ON THE DRAG OF FLUID AND SOLID PARTICLES FREELY MOVING IN A CONTINUOUS MEDIUM

by

Igor V. Haljasmaa

B.S., Ural State University, Russia, 1985

M.S., University of Pittsburgh, 2000

Submitted to the Graduate Faculty of

The School of Engineering in partial fulfillment

of the requirements for the degree of

Doctor of Philosophy

University of Pittsburgh

2006

UNIVERSITY OF PITTSBURGH

SCHOOL OF ENGINEERING

This dissertation was presented

by

Igor V. Haljasmaa

It was defended on

June 19, 2006

and approved by

A.M. Robertson, Associate Professor, Mechanical Engineering Dept.

G.P. Galdi, Professor, Mechanical Engineering Dept.

W. Goldburg, Professor, Physics & Astronomy Dept.

R.P. Warzinski, Research Chemist, Office of Science & Technology, NETL, US DOE

S.K. Cho, Assistant Professor, Mechanical Engineering Dept.

Dissertation Director:

A.M. Robertson, Associate Professor, Mechanical Engineering Dept.

ON THE DRAG OF FLUID AND SOLID PARTICLES FREELY MOVING IN A CONTINUOUS MEDIUM

Igor V. Haljasmaa, PhD

University of Pittsburgh, 2006

Despite the abundance of experimental results on the free motion of solid, liquid, and gaseous particles under various conditions, there is no successful systematization of a drag curve across all three phases. Empirical models offered in the past can be quite useful within the limits of a particular class. However, they lack the capability to explain differences in hydrodynamic behavior across all types from one generalized prospective. The ultimate goal of this study is to provide such a systematic description based on a complete set of non-dimensional parameters, using contemporary knowledge along with our experiments on free particle motion in a quiescent medium.

As a result of experimental studies directed at this objective, instability in particle steady rectilinear motion was identified which was shown to correspond to a bifurcation in the drag curve. Significantly, the onset of this bifurcation did not in general coincide with the onset of vortex shedding around the particle. The particle/ medium density ratio appears to play an important role in the onset point and the characteristics of the non-rectilinear motion, though this parameter was not taken into account in most previous parametric studies. Within the fluid mechanics community, the fluid particle viscosity ratio is generally believed to play a negligible

role in particle motion in contaminated media. However, as a damping factor, particle viscosity can be important for the onset of shape instability and shape oscillations.

Based on our experimental results, along with previous experimental, analytical and numerical works of various authors, a systematic description of the particle drag is suggested.

The fundamental results described above were applied to the specific problem of maintaining CO_2 particles in a fixed viewing region in a countercurrent flow column for long term studies. Countercurrent flow with chosen velocity profiles and tapered column geometry were used to stabilize the buoyant particles in the laboratory frame while minimizing the deviation of the CO_2 particle from the natural free rising (or sinking) motion in the ocean. Design optimization for the experimental unit, limitations of the stabilization process, and parameters affecting particle behavior are discussed.

TABLE OF CONTENTS

LIST OF TABLES

LIST OF FIGURES

LIST OF SYMBOLS AND ABBREVIATIONS

Symbols

$C_D = \frac{4}{3}\frac{\Delta\rho}{\rho}\frac{gD}{U_{term}^2}$	drag coefficient
D	particle diameter ($D = D_{eq}$ for a non-spherical particle)
$D_{eq} = (6V/\pi)^{1/3}$	equivalent diameter
$D_N = \left(\mathrm{Re}^2\, C_D\right)^{1/3}$	non-dimensional diameter
$Eo = \frac{\Delta\rho\, g\, D_{eq}^2}{\gamma}$	Eotvos number
F_d	drag force
F_b	buoyant force
g	acceleration of gravity
$2h$	height of diffuser in the HWT or LWT
K_d	derivative gain of PID
K_i	integral gain of PID
K_p	proportional gain of PID
$Mo = \frac{\Delta\rho\mu^4 g}{\rho^2\gamma^3}$	Morton number
$r(z)$	radius of test section at current vertical particle location z in the HWT
r_o	radius of test section at the set point ($z = 0$)
$R = D/2$	particle radius ($R = R_{eq} = D_{eq}/2$ for a non-spherical particle)

R_f	radius of curvature of a spherical cap
R_{cap}	radius of projected area of a spherical cap
$\mathrm{Re} = \frac{\rho D U}{\mu}$	Reynolds number
$St = \omega D / U$	Strouhal number
$U\ (= U_{term})$	terminal velocity (unless stated otherwise)
$U_N = \left(\mathrm{Re}/ C_D\right)^{1/3}$	non-dimensional velocity
U_{term}	terminal velocity of a particle
V	particle volume
z	vertical position of a particle in the test section of the HWT or LWT
α	angle of diffuser in the HWT or LWT
γ	interfacial tension
$\lambda = \mu_p/\mu$	particle/ medium viscosity ratio
μ	dynamic viscosity of medium
μ_p	dynamic viscosity of a particle
$\nu = \mu / \rho$	kinematic viscosity
ρ	medium (water) density
ρ_p	particle density
$\Delta\rho = \lvert\rho - \rho_p\rvert$	density difference
2ϕ	stagnant cap angle in surfactant cap model
φ_o	angle of a spherical cap
ω	frequency

Abbreviations

HDPE	High-density polyethylene
HWT	High-pressure water tunnel
LBC*	Lower bound curve
LML*	Large Morton limit
LWT	Low pressure water tunnel
NETL	National Energy Technology Laboratory
PID	Proportional-integral-derivative (controller)
PP	Polypropylene
SCL*	Spherical cap limit
SDC*	Standard drag curve
UBC*	Upper bound curve

* Abbreviations, first suggested in this dissertation

PREFACE

First of all, I would like to express my deepest sense of gratitude to two people, without whom this work would be impossible: my adviser, Dr. Anne M. Robertson, for her patient guidance, encouragement, and advice; and my mentor at the National Energy Technology Laboratory (NETL), Robert P. Warzinski, for his continuous support and guidance.

My special thanks and deepest appreciation also extend to Ronald J. Lynn, a Professional Engineer at the NETL, who made possible smooth running of the experimental systems and provided a priceless help with data collection and analysis. I am thankful to Charles Levander, a technician at the NETL, for his help in assembling the experimental unit.

My sincere thanks will also extend to the members of my PhD committee, Dr. G.P. Galdi, Dr. W. Goldburg, and Dr. S.K. Cho for their time, valuable comments and suggestions.

I greatly appreciate the help of Dr. D.D. Joseph and his laboratory in precise interfacial tension measurements, which I needed for data analysis.

The last, but not the least, I would like to thank my wife, Irina Haljasmaa, for her understanding, patience, and support during my PhD years.

1.0 INTRODUCTION

1.1 RESEARCH MOTIVATION

Different branches of science, various technological applications, and just everyday life feature an extremely wide variety of solid, liquid, or gaseous particles, moving in fluid media. An important subclass of this general problem is free (not forced) motion of a positively or negatively buoyant particle in a quiescent fluid. Vast amounts of experimental material devoted to free motion of the particles in continuous media are summarized in [1]. The non-linearity of the problem makes it impossible to obtain an exact analytical solution (even for solid particles) at non-zero Reynolds numbers. Therefore, it is important to find possible universalities in the behavior of such systems using non-dimensional analysis.

The aims of this research originated from a multidisciplinary study conducted at the National Energy Technology Center (NETL) of the U.S. Department of Energy (DOE). This study is devoted to the mitigation of the greenhouse effect by means of large-scale, long-term sequestration of greenhouse gases (mainly, carbon dioxide) from the atmosphere [2]. The largest of available sequestration sites are the oceans, where sequestration already occurs naturally in the surface layers [3]. The novel idea was to skip the surface layer and inject man made CO_2 directly into the deep ocean. The injected CO_2 is expected to have a residence time of several hundred years [2] and provide mankind a recovery period to revise current energy production and consumption strategies.

For a variety of reasons, interest has recently shifted away from oceanic to geologic sequestration; however, the data obtained from this study will be applicable to any liquid CO_2 entering the deep ocean, whether from a leak from a suboceanic geologic CO_2 storage reservoir, such as the Sleipner project in Norway, from a natural seep or vent, or from an engineered release into the deep ocean. The information obtained here contributes toward a better understanding of the fate of the CO_2 oceanic release and the impact of possible CO_2 hydrate formation[1] on the dissolution process.

The physical properties of CO_2 are such, that, with a change in depth, a wide range of densities and aggregate states are covered [4]. For example, at a depth less than 500 m, CO_2 is a gas with density $0.002 < \rho < 0.12\,\mathrm{g/cm^3}$. Deeper in the ocean CO_2 is in a liquid state, and its density increases with depth from 0.85 g/cm^3 to the sea water density (1.03 g/cm^3) at 2,700 m. Deeper than 2,700 m, CO_2 becomes negatively buoyant and sinks. In addition, the formation of a hydrate shell around the CO_2 particle is possible under certain conditions [5]. In this situation, the possibility of shape change is significantly suppressed, and the particle behaves more like a solid. Overall, quite a large range of qualitatively different dynamic regimes is covered by CO_2 particles in the ocean.

A central goal of the NETL work is to better understand the behavior of individual CO_2 particles in the deep ocean including hydrate formation. In order to achieve this goal, it is useful to develop an experimental system where a CO_2 particle can be maintained at a fixed viewing location in a reservoir of water. This can be achieved using a counter-current flow system, requiring at least small velocity gradients in order to maintain the particle in the desired viewing location (see Sections 3.2 & 4.2 for more details). These velocity gradients are an experimental

[1] Ice-like CO_2 clathrate hydrate can form as discrete "flake-like" particles or as a shell on a CO_2 drop, and significantly affects the mechanical and chemical behavior of a drop (e.g., buoyancy, deformability, dissolution rate).

artifact, not found in the real oceanic environment. While studying the behavior of liquid particles in gradient flows, we realized that even the simpler related problem of a free particle in quiescent fluids lacks a well defined universal framework. Since there remain fundamental unanswered questions for even this simple problem, in this thesis, we first focus on liquid particle behavior in a quiescent fluid.

The current level of computational science allows direct numerical simulation of many basic and advanced problems in fluid mechanics. However, there is still a need for better physical insight as well as for a relatively simple tool for engineering applications. Free motion of a buoyant particle in a quiescent fluid is a very basic problem having numerous engineering correlations. Nevertheless, for the case of a fluid particle, this problem lacks a well defined universal approach similar to the Standard Drag Curve (SDC) for solid spheres (see **Figure 1** below). In fact (as it will be discussed later), even the SDC is valid for freely moving spheres for only a limited range of particle/medium parameters.

Numerical simulations themselves can serve as a tool for "revealing universalities" in particle/ medium systems. However, besides being time consuming, they also pose another problem – validation of the physical model used in the numerical analysis. Experimental results are needed as a primary source of information. Thus, an experimental approach is taken in this work.

Briefly, the central goal of this work is:

To provide a systematic description of particle hydrodynamic behavior based on a complete set of non-dimensional parameters, using contemporary knowledge along with our experiments on free particle motion in a quiescent medium. An additional applied goal is to investigate the details of particle behavior in a special class of gradient flows intended

to maintain the particle in a fixed location in the laboratory frame so that long term observation can be made.

The material in this thesis is organized as follows:

The remainder of this introductory chapter provides a brief historical note, describing the main classical works and results for the motion of solid and fluid particles.

Chapter 2.0 consists of an extensive discussion of open questions and unresolved problems existing in the contemporary literature for solid/ liquid/ gaseous particles motion. An attempt is made to look at particles in all physical states (solid, liquid, gas) from the same perspective. The comparative importance of different parameters and dimensionless numbers for different conditions is discussed. Qualitative and quantitative differences between fixed and freely moving particles are emphasized.

The fundamental and applied objectives of the work are provided in Chapter 3.0. The experimental work used to meet these objectives is outlined.

Chapter 4.0 includes a description of the experimental facilities and procedures, as well as their development challenges.

Chapter 5.0 is devoted to experimental findings and discussion on the fundamentals of free particle motion in a quiescent medium. Drag curves for freely moving solid spheres are analyzed. The importance of relative (particle/ medium) density and effects of non-uniform density distribution in a solid particle are discussed. Experiments with fluid particles have revealed some interesting phenomena in the drag curve behavior. Hypotheses are suggested to explain these phenomena. A generalized approach for the description of the drag for solid spheres/ drops/ bubbles is suggested.

Chapter 6.0 deals with the applied problem of long term observations of CO_2 drops in the experimental unit, simulating the deep ocean environment. Optimization aspects of the unit geometry are considered and stabilization of fluid particles in this geometry is investigated. Limitations of the stabilization mechanisms are discussed.

Finally, Chapter 7.0 includes a summary of the most important findings, concluding remarks, and an outline of possible directions for future studies.

1.2 SOLID SPHERICAL PARTICLES

If we consider a rigid homogeneous spherical particle moving at a constant velocity, U, in a linear viscous fluid, then the drag force exerted on the particle will be a function of the following parameters:

$$F_d = F_d(\rho, \mu, U, D), \tag{1}$$

where: ρ, μ – fluid density and viscosity;

D – particle diameter;

U – particle/fluid relative velocity.

Classical non-dimensional analysis (e.g., [6, 7]) with application of Buckingham π-theorem reduces the description of the behavior of such a sphere to the relation of two non-dimensional parameters. The choice of these two non-dimensional parameters is not unique. However, selecting the drag coefficient (C_D) and Reynolds number (Re) as independent parameters has proved to be quite effective (e.g., [8-12]). The plot of C_D vs. Re was first suggested by Rayleigh (see p.605 of [10]). This choice reveals some universality in the behavior of solid spheres in liquid. The so called Standard Drag Curve (SDC) for solid spheres establishes a universal

relationship between the drag coefficient C_D and Reynolds number Re, replacing Eq.(1) with $C_D = C_D(\mathrm{Re})$, where:

$$C_D = \frac{2F_d}{\rho U^2 A}\left[= \frac{\text{Drag force}}{\text{Dynamic force}}\right]; \qquad \mathrm{Re} = \frac{\rho DU}{\mu}\left[= \frac{\text{Inertial forces}}{\text{Viscous forces}}\right], \tag{2}$$

$A = \pi D^2/4$ – cross section of the sphere.

Note that this general definition of the drag coefficient is valid not only for a freely moving sphere, but for any uniform flow around the sphere, either free or fixed. For the case of developed (steady) motion of the solid sphere in a quiescent medium, this definition can be expressed in terms of material and geometric parameters rather than the drag force (see Eq.(4) below).

For certain physical conditions, the particle will go through an initial acceleration period and tend to a steady velocity referred to as the terminal velocity. In this case, the particle buoyancy is balanced by the drag force on the particle:

$$F_d = F_b \qquad \Rightarrow \qquad \frac{\pi}{8} C_D \rho U_{term}^2 D^2 = \frac{\pi}{6} D^3 \Delta\rho g\,, \tag{3}$$

where: U_{term} – particle terminal velocity in quiescent medium;

$\Delta\rho = \rho_p - \rho$ – particle and medium density difference.

From Eq.(3), the expression for the drag coefficient of steady freely moving sphere in a quiescent medium can be derived:

$$C_D = \frac{4}{3}\frac{\Delta\rho}{\rho}\frac{gD}{U_{term}^2} = \left[\frac{\text{Buoyant force}}{\text{Dynamic force}}\right]. \tag{4}$$

It is crucial to remember, that the force balance (3) is valid, strictly speaking, in the absence of acceleration (U_{term} is a constant). If a generalized terminal velocity is introduced for non-

rectilinear particle motion (e.g., spiral or zig-zag motion), it is understood as a vertical component of terminal velocity, averaged over a suitable time of particle motion.

An interest in the problem of free motion of solid spherical particles goes back to I. Newton [13]. He measured the terminal velocity of spheres with different diameters and densities dropped from the dome of St. Paul's Cathedral in London. He obtained the following empirical expression for the terminal velocity of a freely falling particle (as described in [14]):

$$U_{term} = \sqrt{\frac{\pi}{6}\frac{\Delta\rho}{\rho}\frac{gD}{k_n}}, \tag{5}$$

where k_n was found to be approximately a constant of 0.18, which corresponds to a drag coefficient slightly below 0.5. The range of the Reynolds number considered by Newton was $10^3 < \mathrm{Re} < 2 \cdot 10^5$ and it is typically referred to as the Newtonian region.

A special case of the flow past a sphere emerges when Re<<1 (fluid inertia is negligible compared to the viscous forces). Omitting the non-linear inertial term in the Navier-Stokes equation significantly simplifies the problem by reducing it to a linear partial differential equation. This problem was solved exactly in 1851 by G.G. Stokes [15] and it is one of few problems that can be solved analytically. The solution gives a very simple non-dimensional expression for the drag:

$$C_D = 24/\mathrm{Re}. \tag{6}$$

In 1900, H.S. Allen [16] performed a set of experiments with free rising tiny spherical air bubbles, as well as with amber and steel spheres settling in Newtonian liquids of various viscosities. His data were sparse, and covered just some isolated regions of Reynolds numbers (0.2<Re<200 and 2,400<Re<8,000). In addition, the results were not represented in non-

dimensional form. Nevertheless, this work is an important milestone in an attempt to classify the drag on spheres, and these experimental results were extensively referenced by other researchers.

In 1922, Wieselsberger [8] measured air drag around fixed spheres, covering a rather wide range of sphere diameters (from 0.8 to 28cm) and Re numbers (800<Re<770,000). He managed to go beyond the Newtonian range of Re, and was able to catch what is known today as the crisis of the drag (sharp drop of the drag due to the transition to the turbulent boundary layer).

In 1927, H. Liebster [9] obtained more detailed experimental data on steel spheres falling in liquids of high and intermediate viscosity, covering the range of 0.5<Re<3,000.

In 1940 Lapple & Shepherd [10] tabulated the shape of the drag curve for spheres by averaging the experimental results of 17 different research groups (including [8, 9, 16]). This shape is known as a Standard Drag Curve (SDC) and it is used in most of the literature on fluid mechanics.

In 1974, Bailey [17] suggested a slight modification to the SDC. He claimed that the SDC underestimated the drag up to 5% in the Newtonian range and slightly overestimated it in the turbulent boundary layer regime.

A number of authors suggested correlations for the tabulated SDC (e.g., see p.111 of [1] for the list of the most commonly used correlations). The correlation that gives the best fit in the widest range of Reynolds numbers was proposed by Turton and Levenspiel [11]. The authors considered 408 data points from 19 different sources (including [8, 9, 16]) and sought a least squares fit of the following expression:

$$C_D = \frac{24}{\mathrm{Re}}\left(1 + c_1\,\mathrm{Re}^{c_2}\right) + \frac{c_3}{1 + c_4\,\mathrm{Re}^{c_5}} \tag{7a}$$

The resulting values of constants are reproduced below:

$$C_D = \frac{24}{\mathrm{Re}}\left(1 + 0.173\,\mathrm{Re}^{0.657}\right) + \frac{0.413}{1 + 16300\ \mathrm{Re}^{-1.09}} \qquad (7b)$$

In **Figure 1** we compiled experimental data[2] from sources [8, 9, 16] along with a graphical representation of the curve corresponding to Turton and Levenspiel's results given in Eq.(7b).

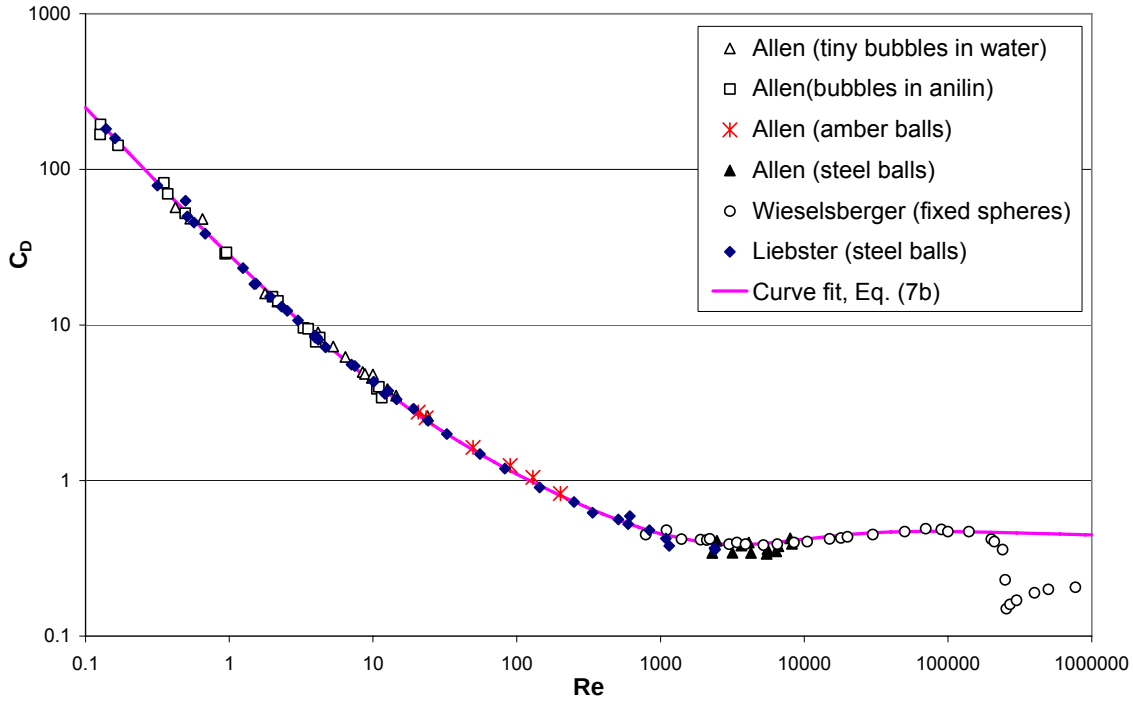

Figure 1. Standard drag curve (SDC) and experimental results for solid spheres

Note that correlation (7b) is valid for Reynolds numbers up to about 100,000. For higher values of Re, the drag coefficient experiences a sudden drop due to the transition to turbulent boundary layer (e.g., [8, 12], and works cited in [8, 12]). This drop is not captured by the above correlation. In addition, a new parameter comes into play for turbulent boundary layer – ε / D, where ε is the surface roughness. After this transition, the behavior of solid spheres can't be described by a

[2] Strictly speaking, air bubbles are not solid spheres and should not be included in Fig.1. However, as discussed in Section 1.3, tiny bubbles have an almost perfectly spherical shape and, due to the presence of surfactants, they behave hydrodynamically like solid bodies.

single drag curve [18]. However, the fluid and solid particles considered in this work don't exceed Re ≈ 100,000, so the usage of Eq.(7b) as a correlation for SDC is justified within the scope of this paper.

In fact, it will be shown later in this work (Section 2.1) that even at Re much lower than 100,000, the drag of freely moving solid spherical particles can not be uniquely defined from known Re. Therefore, at least one more non-dimensional parameter is needed, and the standard drag curve should be replaced by a drag surface to account for the additional dimension in parameter space.

1.3 FLUID PARTICLES

Numerous experimental, numerical, and theoretical studies are available on the free motion of a liquid or gaseous particle in a quiescent fluid. The first attempt to attack this problem theoretically was undertaken at the beginning of the 20th century by Hadamard [19] and independently by Rybczinski [20]. They considered a spherical fluid particle and assumed no shape change during the motion. Under this assumption, the only reason why the motion of such a particle would differ from that of a solid sphere is due to a difference in boundary conditions. For solid spheres, the no slip condition on the surface was assumed. For fluid particles, the continuity of velocity and tangential stress at the surface was used instead (mobile interface). Under the assumption of Stokes viscous flow (Re<<1, no inertia), this boundary condition corresponds to the following solution for terminal velocity of a spherical fluid particle:

$$U_{term} = \frac{1}{12}\frac{D^2 g\Delta\rho}{\mu}\frac{\mu+\mu_p}{\mu+3/2\mu_p} \text{ (Hadamard-Rybczynski solution)} \qquad (8)$$

and the corresponding drag coefficient using Eq.(3) and Eq.(8) is:

$$C_D = \frac{16}{\mathrm{Re}} \frac{\mu + 3/2\mu_p}{\mu + \mu_p} = \frac{8}{\mathrm{Re}} \frac{2 + 3\lambda}{1 + \lambda}, \qquad (9)$$

where $\lambda = \mu_p / \mu$ - droplet/ medium viscosity ratio.

Note that taking the limit $\lambda \to \infty$ leads to the standard solution for a solid sphere in Stokes flow: $C_D = 24/\mathrm{Re}$. At the other extreme, $\lambda \to 0$, Eq.(9) gives a solution for gaseous bubble[3]: $C_D = 16/\mathrm{Re}$. Thus, the drag coefficient increases by 50%, as the particle interface (tangential) mobility decreases, from gaseous bubble to solid particle.

However, this theoretical prediction doesn't match experimental results even in the Stokes regime. Although experiments (e.g., [16] – for small gas bubbles, [21]) confirm that small fluid particles in the viscous regime have a spherical shape, their drag is closer to the Stokes result for rigid particles Eq.(6) than to the Hadamard result Eq.(9). This phenomenon was first noted by W.N. Bond & D.A. Newton [21] and confirmed in other experimental works [16, 22-24] (although with increasing diameter, there is some trend towards Hadamard-Rybczinski values [21, 23]). Such a deviation from theory is generally believed to be due to the effect of surfactants [25-27].

Surfactants are believed to form a viscous layer on the particle-fluid interface, which reduces the surface tangential mobility [25-27]. Due to the particle motion, surfactants are swept to the rear and form a stagnant cap there, leaving the frontal region relatively uncontaminated (**Figure 2**). This "no slip cap" significantly retards the fluid particle terminal velocity. Sadhal & Johnson [28] elaborated on the idea of stagnant cap and suggested a theory for the effect of surfactants on a spherical fluid particle in Stokes flow. They assumed the no slip boundary condition for the

[3] A gaseous bubble is defined as a fluid particle for which $\mu_p << \mu$ and $\rho_p << \rho$

stagnant cap and continuity of shear stress on the rest of the interface. The following exact solution was obtained in [28]:

$$C_D = \frac{16}{\mathrm{Re}}\left\{\frac{\mu}{4\pi\left(\mu+\mu_p\right)}\left[2\phi+\sin\phi-\sin 2\phi-\frac{1}{3}\sin 3\phi\right]+\frac{\mu+3/2\mu_p}{\mu+\mu_p}\right\}, \qquad (10)$$

where ϕ is the angle of a stagnant cap.

If the stagnant cap angle approaches zero, the Hadamard-Rybczinski solution is recovered from Eq.(10). For a "no slip cap" covering the whole particle, the Stokes solution for solid sphere is obtained.

Levich [25][4] introduced an additional retardation coefficient β into Eq.(9) accounting for the presence of surface active materials:

$$C_D = \frac{16}{\mathrm{Re}}\frac{\mu+3/2\mu_p+3/2\beta}{\mu+\mu_p+\beta}, \qquad (11)$$

and considered various mechanisms for the surfactant adsorption/ desorption process. As can be seen from a comparison of Eq.(9) and Eq.(11), this approach is equivalent to the introduction of an additional pseudo viscosity of the fluid particle.

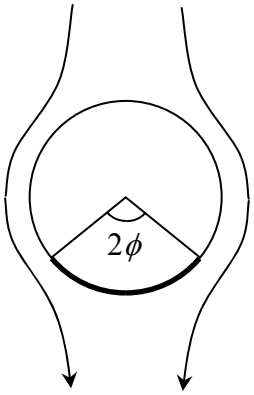

Figure 2. Surfactant cap model (no slip B.C. on the cap; continuity of shear stress on the rest of the interface)

It is interesting that in many practical cases, the fluid particles preserve an almost spherical shape for quite large magnitudes of Re (up to several hundred, e.g., p.125 of [1]). Levich suggested an interesting model for such a particle in the range of "intermediate" Re numbers (50<Re<800, pp.436-448 of [25]). Assuming no surfactants and preserving the spherical shape of a particle, he

[4] An equation similar to (11) was obtained first by Boussinesq in 1913, but he did not consider the distribution of surfactants on the interface, but instead developed a theory of a viscous membrane around the particle.

introduced a thin boundary layer near the particle/medium interface. He further assumed an ideal fluid motion outside this thin layer and tried to find the velocity distribution in the vicinity of the particle surface. Solving this problem using boundary layer approximations (Re>50), he found that even for "intermediate" Re (50<Re<800), separation occurs in a very narrow region (several degrees). Therefore, form drag is negligible and resistance is determined by viscous drag: $F_d = 6\pi DU\mu$, which corresponds to:

$$C_D = 48/\mathrm{Re}. \tag{12a}$$

Harper and Moore [29] extended this solution, accounting for the particle/medium viscosity ratio. They obtained the following asymptotic solution:

$$C_D = \frac{48}{\mathrm{Re}}\left(1+\frac{3}{2}\lambda\right). \tag{12b}$$

As the authors stated in [29], this solution is valid for Re "large enough for boundary-layer theory to hold, but small enough for surface tension to keep the drop nearly spherical." However, Eq.(12b) has only a limited usefulness. It can be used as a rough approximation of the experimental data for $0<\lambda<1$, but it becomes invalid as λ appreciably exceeds 1.

We will return to the case of "intermediate" Re later, in Section 2.3.3.

At the other end of the scale, where viscous forces are negligible compared to inertial effects, a certain universality of the large particle behavior at high Re was observed. It was noticed [30, 31] that, for a completely inertial regime, fluid particles take an approximately spherical cap shape. The angle $2\varphi_0$ of the spherical cap is measured from the center of an imaginary sphere with radius matching the radius of curvature at the top of the spherical cap (see **Figure 3**). Based

on experimental results, $2\varphi_0$ lies within a rather narrow range [95°,115°]. The following approximation for the terminal velocity of a large gas bubble was derived in [30]:

$$U_{term} = \frac{2}{3}\sqrt{gR_f}\ , \tag{13a}$$

Later (see p.474-477 of [31]), this result was generalized for a large liquid particle:

$$U_{term} = \frac{2}{3}\sqrt{gR_f\,\frac{\Delta\rho}{\rho}}\ , \tag{13b}$$

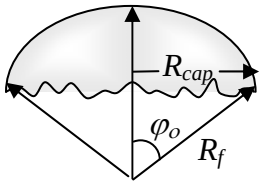

where R is the radius of curvature of the cap, assumed to be constant.

Figure 3 Spherical cap model, with constant radius of curvature R_f.

Note that the only information about the particle shape required in these derivations is the particle sphericity in the neighborhood of the frontal stagnation point. Hence, no knowledge of the cap angle $2\varphi_0$ or the particularities of the particle shape in the rear are required in order to obtain Eq.(13a) or Eq.(13b). Another important assumption used in this derivation is the hypothesis that the purely hydrostatic pressure distribution inside the particle or, in other words, the dynamic force inside the particle is negligible compared to the outside (see Appendix A for more detail).

It is remarkable, that expressions as simple as Eq.(13a,b) have shown a very good agreement with experimental data (e.g., [30, 32, 33]). Some variations of Eq.(13a,b) are discussed in p.205 of [1].

An important note should be made about the particle terminal velocity. For many regimes of particle motion, the path is not rectilinear (e.g., [30, 34, 35]). That is, the terminal velocity of the rising/ falling particle is not a constant, but rather appear to be described by periodic or

stochastic oscillations around some averaged value. When such cases are considered, a generalized terminal velocity is introduced as a time-averaged rise/ fall velocity of the particle.

The drag coefficient, analogous to Eq.(4) for a solid sphere, can be introduced for a large fluid particle. But since a fluid particle, in general, has a non-spherical shape, its diameter is understood to be a diameter of an equivalent sphere, that is, a sphere of the same volume as the considered fluid particle. This approach is widely used for the description of the behavior of fluid particles (see, for example, [1]). The advantage of this approach is that it does not relate particle behavior to any particular shape and, thus, gives more general and systematic results. It also allows comparison to the behavior of solid particles of the same volume and density. Appendix A provides a derivation of the drag coefficient for a spherical cap particle in terms of the equivalent diameter. From Appendix A, it follows that the drag coefficient for a fully developed spherical cap is independent of Re and has a constant value. This conclusion is in agreement with numerous experimental results [24, 30, 32, 36-38] for "equivalent drag coefficient", which give the magnitude of 8/3 for this constant. This is somewhat similar to the behavior of the solid sphere in the Newtonian regime. However, values of the drag coefficient are quite different for a solid sphere and for a spherical cap. While for a solid sphere C_D is approximately 0.45, for spherical cap it is about 8/3, that is, 6 times larger[5].

Although expressions (13a,b) do not depend on the shape at the rear of the particle, the "equivalent drag coefficient" was obtained for the particular shape of the large fluid particle (namely, spherical cap with the "cap angle" of ≈ 52°, see Appendix A). Consequently, if the shape of a particle deviates from spherical cap, the magnitude of C_D may also deviate from 8/3.

[5] The magnitude of the drag coefficient for the spherical cap may seem excessively large to an audience familiar with drags of some standard shapes. This is because the drag was calculated based on the cross section of a sphere of equivalent volume instead of the projected particle area commonly used in engineering hydrodynamics. See Appendix A for details.

For example, if the cap angle is appreciably larger that 52°, we obtain $C_D > 8/3$. Questions regarding the applicability of the spherical cap limit to the motion of liquid drops will be addressed in the later chapters (see, for example, Subsection 2.3.5).

In summary, there are two limiting cases – small Reynolds numbers and relatively large Reynolds numbers. Basically, these are the only cases, where some analytical work can be done:

Small Re: $C_D \approx B/\mathrm{Re}$, $(16 \le B \le 24)$; (14a)

Large Re: $C_D \approx 8/3$; (14b)

where: $\mathrm{Re} = \dfrac{\rho D_{eq} U}{\mu}$; $C_D = \dfrac{4}{3}\dfrac{\Delta\rho}{\rho}\dfrac{gD_{eq}}{U_{term}^2}$;

D_{eq} – is the diameter of a sphere volumetrically equivalent to the fluid particle, as discussed above.

A graphical representation of these two cases is shown in **Figure 4**.

What happens to the drag curve in the intermediate Reynolds number regime? What are the central physical phenomena responsible for the drag curve behavior in this regime? What is the full set of non-dimensional parameters for a complete description of the motion of a liquid particle? When do we need a full set of parameters, and when is it reasonable to neglect some of these parameters? These questions will be addressed in the following chapters.

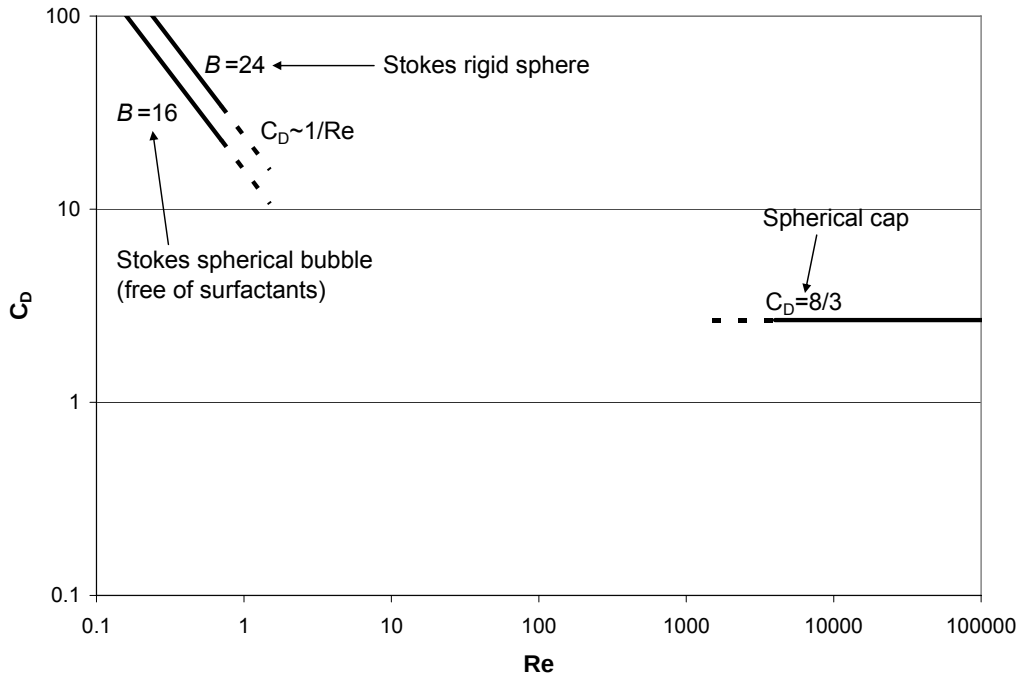

Figure 4. Limiting cases for the drag of a fluid particle

2.0 PROBLEM FORMULATION AND APPROACH

2.1 FREE MOTION OF SOLID SPHERES

2.1.1 Standard drag curve and freely moving solid spheres

A central utility of the SDC is that the correlation (7b) for $C_D(\mathrm{Re})$ can be used to obtain the terminal velocity of the solid spheres as a function of radius and relative sphere density. Indeed, from the quasi-steady balance equation (3), the solid particle diameter and velocity can be expressed in terms of the Reynolds number:

$$\begin{cases} U^3 = \dfrac{4}{3}\dfrac{\mathrm{Re}}{C_D(\mathrm{Re})}\dfrac{\Delta\rho\mu}{\rho^2}g \\ D^3 = (2R)^3 = \dfrac{3}{4}\dfrac{\mu^2 C_D(\mathrm{Re})\,\mathrm{Re}^2}{\rho\Delta\rho g} \end{cases}, \tag{15}$$

where Eq.(7b) can be used for $C_D(\mathrm{Re})$ at Re<100,000.

From system (15), the sphere terminal velocity U can be obtained as a function of its diameter D. Re can't be excluded explicitly from system (15), but one can build a family of parametric curves, using Re as a parameter for solid spheres of different densities. **Figure 5** depicts such a set of curves for spheres with relative densities 0.01, 0.05, 0.1 and 1, falling in water. The relative density is defined as $Rd = \Delta\rho/\rho$ (where ρ is the density of water). The sharp velocity growth at $\mathrm{Re} \approx 200{,}000$ corresponds to the transition to a turbulent boundary layer ([8, 12]). For example, this means that a 20cm smooth nylon ball ($Rd \approx 0.13$,

$\mathrm{Re} \approx 400{,}000$) in water should fall almost 2.5 times faster than a 15cm ball ($Rd \approx 0.13$, $\mathrm{Re} \approx 100{,}000$).

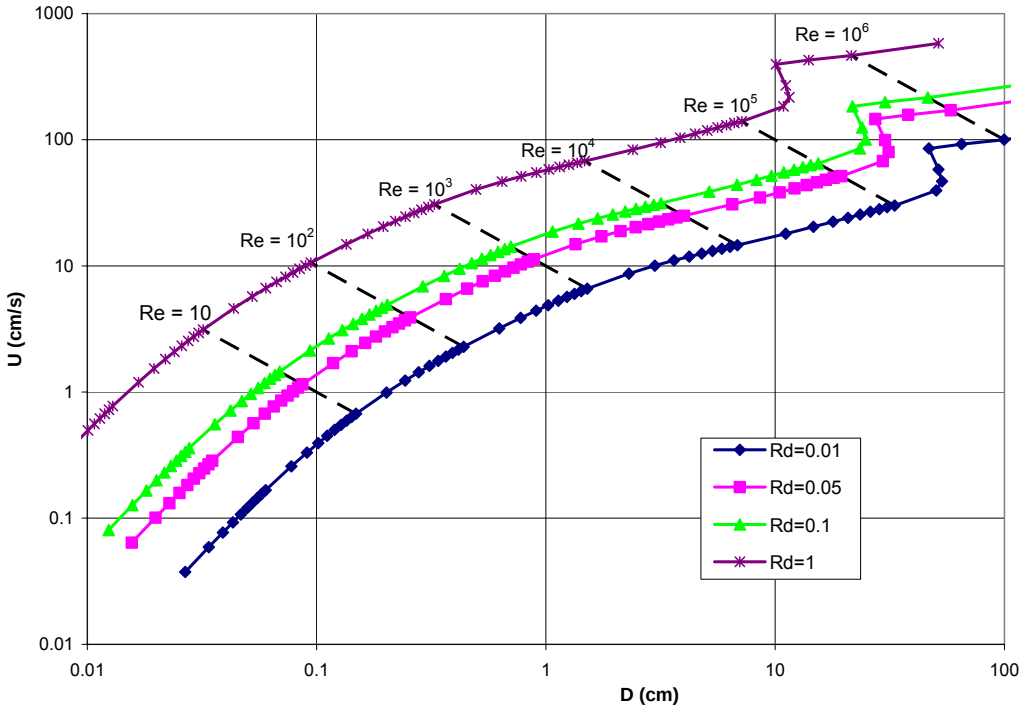

Figure 5. Terminal velocity of solid spheres in water as a function of diameter

Notice the two limiting cases, which follow from correlation (7b). If $\mathrm{Re} < 1$ (creeping flow), then the drag coefficient is with good precision inversely proportional to Re: $C_D \sim 1/\mathrm{Re}$. Using Eq.(15) we can find that for creeping flow $U \sim D^2$. On the other hand, for high Re ($3{,}000 < \mathrm{Re} < 100{,}000$), the drag coefficient is roughly constant: $C_D \approx 0.45$ (Newton's result). Hence, from Eq.(15) we obtain: $U \sim \sqrt{D}$. Both trends can be clearly seen in **Figure 5**.

It follows from Eq.(15) that, for fixed material parameters, particle diameter and terminal velocity are functions of $(\mathrm{Re}^2 C_D)^{1/3}$ and $(\mathrm{Re}/C_D)^{1/3}$, respectively. Hence, we can introduce non-dimensional diameter and velocity:

$$\begin{cases} D_N = \left(\mathrm{Re}^2\, C_D(\mathrm{Re})\right)^{1/3} \\ U_N = \left(\dfrac{\mathrm{Re}}{C_D(\mathrm{Re})}\right)^{1/3} \end{cases}, \qquad (16)$$

and express the SDC in an alternative way, $U_N = U_N(D_N)$ (pp.113-115 of [1]). This dimensionless form (**Figure 6**) is not very commonly used, but it has some advantages compared to a more traditional representation as the drag versus Reynolds number. It provides an explicit dependence of the terminal velocity on the particle size. In contrast, definitions for Reynolds number and the drag coefficient involve both particle size and terminal velocity and, hence, sometimes can be misleading or difficult to interpret. In Chapter 5.0, we'll use the dimensionless variables introduced in Eq.(16) in order to represent and interpret our experimental results for fluid particles.

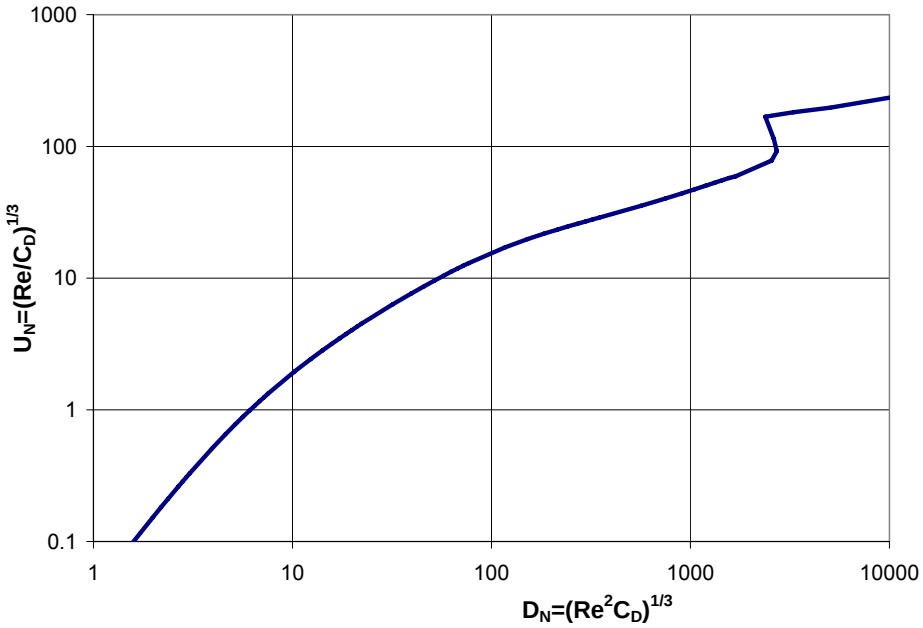

Figure 6. Alternative dimensionless representation of the SDC

All this information is well known in the "fluid mechanics community". The SDC (**Figure 1**) is extensively used in textbooks on fluids and in the scientific literature to determine the terminal

velocity for a rigid spherical particle of given size and density. Its obvious advantage is simplicity and universality – one curve seems to describe any falling or rising solid sphere.

However, when applying the SDC to certain problems, one should remember how this curve was obtained. There are two types of experiments serving as a basis for the SDC:

- In the first type of experiments [9, 13, 16], falling spheres were considered, that is, the particle density was higher than the density of the medium. Drag was then obtained using a quasi-steady force balance (Eq.(3)). The lightest particles used in this type of experiments were amber spheres [16], which were slightly heavier than water (specific gravity of ≈ 1.05-1.1) and had Re<200. Thus, the effect of vortex shedding on the particle motion was not an issue – particles were, in practice, unaffected by the fluid motion.
- In the second type of experiments [8, 12], solid spheres were fixed in space, and a force exerted on them (in the direction of the flow) by a moving liquid was measured. The drag coefficient was then calculated from a known drag force:

$$\frac{\pi}{2} C_D \rho U^2 R^2 = F_d \,, \tag{17}$$

where U is velocity of the parallel flow far away from the particle. No lateral degrees of freedom were allowed for the sphere, which does not represent the actual free motion.

The legitimate questions here are the following:

1. Is the standard drag curve always valid for freely moving solid spheres?
2. If it's not always valid, what is the range of validity?

This is a classical example of a reversed problem. Flow motion with velocity U is substituted by particle motion with terminal velocity $-U$. Next, the balance of drag force and buoyant force is assumed (see Eq.(2)), and an unknown particle velocity is derived from the resulting equation.

However, this force balance implies quasi-steady motion, and it does not take into account dynamics of the system (acceleration). As long as the particle motion remains rectilinear, we expect its terminal velocity to be a constant at every time instant. Absence of particle acceleration justifies the quasi-steady approach, and the drag coefficient for such a motion will successfully fit the standard drag curve.

It was observed experimentally and confirmed by numerical simulations (i.e. [39-43] and works cited therein) that starting from a certain value of Re, the velocity field around the spherical particle loses stability and becomes asymmetric. A regular axisymmetry breaking bifurcation from a steady, axisymmetric vortex ring to a bifid wake with planar symmetry was reported at a Re in the range 150-212 [39-42]. If flow visualization techniques are used [39], this regime can be characterized by the presence of two steady trails ("double thread" or "bifid") in the wake behind the sphere. The plane of these trails is off the flow centerline. Thus, a transition from axial to planar symmetry takes place, where the orientation of the symmetry plane depends on the character of perturbations at the bifurcation point. A Hopf bifurcation (transition to the unsteady vortex shedding) was identified at Re in the range 270-300 for fixed spheres. Periodic fluctuations of the flow may influence the free particle motion, particularly, causing periodic lateral motion of the particle. Under these circumstances of non-zero particle acceleration, a new non-dimensional parameter should come into play (besides Re and C_D), reflecting the unsteadiness of the problem.

Often, the Strouhal number ($St = \omega D / U$), involving a characteristic frequency, ω, of vortex shedding, is introduced to describe oscillating flows. However, this dimensionless parameter is not very suitable for the goals of this work for two reasons.

1. It was postulated in several theoretical, numerical, and experimental works [43-45] that with growth of Re the transition from steady motion to the chaotic regime occurs through a series of Hopf bifurcations. Loosely speaking, every Hopf bifurcation means the appearance of a new characteristic frequency, which is incommensurate with other frequencies already existing in a non-linear system. Various investigators claim that after the appearance of the third frequency the behavior of the system is not much different from chaotic (e.g., [46-48]). In this situation, there is no sense to talk about a single dominant frequency. For example, in [43] the authors investigated numerically the behavior of the flow around a fixed sphere at Re beyond the first Hopf bifurcation. They were able to observe the second Hopf bifurcation with respective frequency, incommensurate with the first one. Accordingly, they introduced two different Strouhal numbers in order to describe the flow. Thus, the use of the Strouhal number as an additional parameter can be justified only in a rather narrow range of Re between the first and the second bifurcations. And after the third Hopf bifurcation the behavior of the system is associated rather with power spectrum than with some particular frequency.
2. Besides that, the Strouhal number involves terminal velocity and oscillation frequency, which are part of the solution themselves. So, it appears that we try to investigate how the solution is affected by the parameter which is itself a part of the solution. It would be preferable to use a combination of material parameters that are fixed for a chosen pair of particle/ medium and does not involve any specifics of geometry or particle motion.

The issue of choosing a suitable parameter is discussed in the next two subsections.

2.1.2 Qualitative theoretical analysis of particle free motion

As will be discussed in detail below, an important factor regulating the influence of the unsteady flow on a freely moving particle is the density ratio. A light particle in a dense liquid is more susceptible to flow fluctuations and readily follows large enough disturbances. While a heavy particle in a "light" liquid has large enough inertia to inhibit significant lateral motion arising from perturbations of the flow even of moderate frequencies. In other words, we would expect the coupling of the particle motion to the fluid motion to be more important for light particles. In fact, several authors [49-53] studied the lateral motion of falling spheres and noticed that particle inertia can have some effect on the drag. In recent works [54, 55] a large deviation from the standard drag curve (more than twice) was obtained in experiments with light spherical particles ($\rho_p < 0.3\,\rho$) in water.

For more rigorous support of the above qualitative comments, we now consider the full equations of free motion for a rigid particle in quiescent liquid [56]:

$$\begin{cases} m\left(\dfrac{d\underline{\xi}}{dt} + \underline{\omega}\times\underline{\xi}\right) = -\displaystyle\int_S \underline{T}(\underline{w}, P)\cdot\underline{n}\, ds + m_e\,\underline{G} \\ \underline{I}\cdot\dfrac{d\underline{\omega}}{dt} + \underline{\omega}\times(\underline{I}\cdot\underline{\omega}) = -\displaystyle\int_S \underline{y}\times\underline{T}(\underline{w}, P)\cdot\underline{n}\, ds \\ \dfrac{d\underline{G}}{dt} = \underline{G}\times\underline{\omega} \end{cases} \tag{18}$$

where

$\underline{\xi}$ - velocity vector of the particle;

$\underline{\omega}$ - angular velocity of the particle;

m – mass of the particle;

m_e – effective mass (difference of particle mass and mass of displaced liquid);

$\underline{I}$ - moment of inertia of the particle;

$\underline{w}$ - fluid velocity generated by moving particle;

$P = p - \underline{y} \cdot \underline{G}$ - modified pressure in the fluid;

$\underline{y}$ - coordinate vector;

$\underline{G}$ - acceleration of gravity;

$\underline{T}(\underline{w}, P) = -P\underline{I} + \mu\left(\text{grad}\underline{w} + (\text{grad}\underline{w})^T\right)$ - Cauchy stress tensor in Newtonian fluid;

$\underline{n}$ - unit vector normal to the particle surface.

The fluid motion generated by the moving particle satisfies the following equations [56]:

$$\begin{cases} \dfrac{\partial \underline{w}}{\partial t} + \left[(\underline{w} - \underline{\xi} - \underline{\omega} \times \underline{y}) \cdot \text{grad}\underline{w} + \underline{\omega} \times \underline{w}\right] = \Delta \underline{w} - \text{grad}P \\ \text{div}\underline{w} = 0 \end{cases} \tag{19}$$

with corresponding boundary conditions, coupling the particle and fluid motion:

$$\lim_{|\underline{y}| \to \infty} w(\underline{y}, t) = 0; \qquad w(\underline{y}, t) = \underline{\xi} + \underline{\omega} \times \underline{y} \text{ - on the particle boundary.}$$

It is important to note, that all vectors and tensors in Eq.(18) & Eq.(19) are written in the coordinate system associated and oriented (but not moving) with the particle. Thus, $\underline{G}$ has a constant magnitude, but changes direction in this coordinate system as the particle changes its orientation. The expression in square brackets in Eq.(19) is a convective acceleration term rewritten in coordinate system associated (reoriented) with a particle.

The integral $\int_S \underline{T}(\underline{w}, P) \cdot \underline{n}\, ds$ in Eq.(18) represents the sum of all surface forces acting on the particle, and it can be considered as a combination of drag & lift forces. The term $m_e \underline{G}$ represents the buoyancy force acting on the particle. Thus, if there is no particle acceleration or rotation, a simple balance of drag and buoyancy forces takes place (Eq.(2)). However, if the particle accelerates or rotates, the left hand sides of Eq.(18) will not vanish.

As mentioned at the end of the previous section, starting from a Re slightly below 300, the velocity field, $\underline{w}$, around a rigid spherical particle experiences periodic oscillations. It causes a periodic variation of the surface force integral and, as a result (from Eq.(18)), periodic changes in particle acceleration and velocity. Furthermore, lateral motion of the particle alters the flow pattern, so it won't be the same as around the fixed particle. That is, the problem of parallel flow (with remote velocity *U)* around a fixed particle is not equivalent to the particle moving with velocity *–U* in quiescent liquid. In this case, it is useful to introduce a time averaged terminal velocity of the particle, and this velocity will be different from the one, obtained using the standard drag curve.

Now, assume two particles of equal size have the same absolute value but opposite signs of buoyancy (m_e and $-m_e$) in a chosen liquid. Obviously, particles will move in opposite directions (one rises, another sinks). But are these motions identical, if they are mirrored to each other? To answer this question, consider the equations of particle motion (18).

For steady motion and small enough Re, the surface force integral is constant and flow around the particle is symmetric. Thus, there is no force, causing acceleration or rotation of the particle. As a result, the left hand sides of system (18) are identically zeros and the form of these equations is equivalent for both rising and sinking particle. As Re increases above the critical value, flow oscillation around particles begins. Although flow oscillations are nearly identical for

both cases, they affect particles in different ways. Sinking particles have a larger mass, so they are less susceptible to the flow fluctuations.

For the case of non-zero acceleration, divide the first equation of (18) by particle density:

$$V_p\left(\frac{d\underline{\xi}}{dt}+\underline{\omega}\times\underline{\xi}\right)=-\frac{\rho}{\rho_p}\nu\int_S\left[\text{grad}\underline{w}+(\text{grad}\underline{w})^T\right]\cdot\underline{n}\,ds+\frac{1}{\rho_p}\int_S P\cdot\underline{n}\,ds+\frac{\Delta\rho}{\rho_p}V_p\underline{G}, \qquad (20)$$

where V_p is the volume of the particle.

Assuming flow periodicity around the particle (both surface integrals on the right-hand side are periodic) we also obtain a periodic particle acceleration. Equation (20) implies the particle density has an effect on the amplitude of the particle acceleration, although the actual form of this dependence is more complicated than just inverse proportionality as one may think from Eq.(20). This is because the motion of the particle and fluid motion around it are coupled (see Eq.(19)), and the velocity of the flow, $\underline{w}$, itself is affected by the periodic particle velocity, $\underline{\xi}$.

To illustrate the effect of the particle mass, consider a one dimensional linear analogy:

$$m\ddot{x}+c\dot{x}=F\sin\omega t\,, \quad x(0)=x_o\,, \qquad \dot{x}(0)=\mathrm{v}_o \qquad (21)$$

In Eq.(21), x is analogous to the lateral position of our spherical particle, and $F\sin\omega t$ is a periodic force, similar to the lateral component of the force caused by the surface integral in Eq.(15). The constant c is a damping coefficient, corresponding to viscous damping in water.

The solution of this equation is:

$$x=x_o+\underbrace{\frac{m}{c}\mathrm{v}_o\left[1-\exp\left(-\frac{ct}{m}\right)\right]}_{\text{Homogeneous solution}}+\underbrace{\frac{F}{\omega c}\left\{1-\frac{m^2\omega^2\exp(-ct/m)+c^2\cos\omega t+m\omega c\sin\omega t}{m^2\omega^2+c^2}\right\}}_{\text{Particular solution}} \qquad (22)$$

As the particle mass increases, the oscillatory motion caused by the periodic driving force $F\sin\omega t$ becomes weaker, and in the limit of $m\to\infty$ oscillations vanish. Of course, the 3-D non-linear case is much more complex. But the main conclusion stays the same – particle inertia

is an important factor for Re>300, and it causes qualitative difference in behavior of sinking and rising particles of the same buoyancy.

This qualitative difference was emphasized in works of D.G. Karamanev with collaborators [54, 55]. They performed a series of experiments with light solid spheres and tried to build a drag curve for them, which turned to be significantly different from the standard drag curve. Although giving extremely useful information, these experiments were not representative enough to build detailed drag curves for solid spheres of various fixed densities. Unfortunately, the work of Karamanev and collaborators did not resonate with the scientific community and have not been cited frequently. Note once again, that terminal velocity of the particle in these works was obtained by time averaging of the instantaneous vertical velocity component.

2.1.3 Density ratio as a missing key parameter

It was shown above (Eq.(20)) that particle density with respect to the density of medium is an important factor, affecting particle motion. Thus, in the most general case the problem of free motion of the spherical solid particle in a quiescent fluid should involve three non-dimensional parameters. Maintaining traditional representation with C_D and Re, and adding ρ_p / ρ, we obtain:

$$C_D = C_D\left(\mathrm{Re}, \rho_p / \rho\right) \tag{23}$$

It's worthwhile to recall that the density ratio in Eq.(23) can be important only after the onset of the periodic regime of flow around a particle (Re > 270-300, see Section 2.1.1), because the vortex shedding is the only feasible reason, which may cause periodic lateral motion of a particle (Section 2.1.2). Hence, for Re < 270-300 we don't expect the drag for freely moving sphere to deviate from the SDC. On the contrary, for freely moving spheres at Re >270-300, a set of

parametric curves should be used instead of the SDC. To obtain these curves for different density ratios, several sets of experiments should be performed using different densities of solid spheres in various liquids.

It is useful to obtain Eq.(23) for a free particle based on non-dimensional analysis similar to one done in Section 1.2 for a fixed particle (Eq.(1)). The average terminal velocity of rise/ fall of a spherical particle will be a function of the following parameters:

$$U_{term} = U_{term}(\rho, \rho_p, \mu, D, g) \tag{24}$$

Classical non-dimensional analysis in the most general case reduces this function to a relation between three non-dimensional parameters. Choosing the following non-dimensional groups:

$$\Pi_1 = \frac{\rho D U_{term}}{\mu},\ \Pi_2 = \frac{gD}{U_{term}^2},\ \Pi_3 = \frac{\Delta\rho}{\rho}, \tag{25}$$

we notice the expression for the drag coefficient (4) obtained from the balance equation (3) is actually a combination of two non-dimensional parameters - Π_2 and Π_3. Although the analysis for rectilinear motion of a particle can be reduced to only two non-dimensional groups (Π_1 and $\Pi_2 * \Pi_3$), the more general case of a free particle requires three groups (Π_1, Π_2, and Π_3). That is, more generally, expression (23) should be used instead of Eq.(7b).

A drag curve is the most common form of non-dimensional representation of the particle motion. However, as emphasized in Subsection 2.1.1, in some cases it is beneficial to see explicitly the non-dimensional terminal velocity as a function of the non-dimensional particle size. Using the dimensionless diameter and velocity, introduced in Eq.(16), we can describe the behavior of a freely moving solid sphere by the following equation:

$$U_N = f\left(D_N, \frac{\rho_p}{\rho}\right). \tag{26}$$

A similar approach is considered in pp.113-115 of [1]. However, the analysis there is limited to two parameters and, basically, is just another representation of the SDC. (see **Figure 6**) As discussed above, such an approach is applicable only for rectilinear motion of a particle. For the more general case of free particle motion, Eq.(26) must be used instead.

Since most of the non-dimensional analyses in the past were done in terms of drag curves, we will keep the same format in this work for comparative purposes. The graphs for dimensionless velocity versus diameter will be added when helpful for interpreting the experimental results. Thus, both functional dependences (23) and (26) will be used in the later discussion (see Chapter 5.0).

Although only a few works have been devoted to studies where the role of ρ_p / ρ is accounted for, they have to be properly credited. In recent numerical work [57], the effect of density ratio on free motion of a sphere after the onset of regular bifurcation was considered. A symmetry breaking bifurcation was found to lead to the appearance of a "bifid wake" (see Section 2.1.1 on discussion about bifurcations), which in turn causes a small, but non-zero lateral force on the particle. The results show a very insignificant effect of density ratio on critical Re of the bifurcation. Basically, differences in particle motion for various density ratios were observed just in a transition from vertical to slightly inclined from vertical rectilinear motion. This is reasonable, because when the sphere is in steady rectilinear (although non-vertical) motion, its acceleration is zero. As discussed in previous sections, a simple force balance can be written for the sphere. A small lateral component of the velocity (compared to the vertical) ensures that vertical motion of a sphere changes insignificantly (about 1%) after transition to the "bifid regime", as was shown in [57].

Based on the experimental results from [49, 50], Clift et al. (p.115 of [1]) suggested the following correction for the standard drag curve, taking into account the relative density of a spherical particle to medium for $\rho_p / \rho > 1;\ 10^3 < \mathrm{Re} < 2 \cdot 10^5$:

$$C_D' = C_D \left[1 + \frac{0.13}{2.8(\rho_p / \rho) - 1} \right], \tag{27}$$

where C_D is the standard drag.

The authors reported that the terminal velocity changed no more than 3.5% due to the particle density variation. However, only falling spheres were considered ($\rho_p / \rho > 1$) and in this case, the retardation of fall was found negligible for Re<1000.

A simplified correction factor such as Eq.(27) will not be able to satisfactorily reflect reality for several reasons. First, multiplication by a constant factor means the standard drag curve will just be shifted up as a whole. It does not correspond to the physical reasoning developed in Section 2.1 and our preliminary data. Namely, that larger Re causes stronger periodic flow fluctuations around the particle and, hence, larger amplitude of particle horizontal motion, which, in turn, further retards the vertical motion.

Another very important point – the particle density used in Eq.(27) and related experiments was always larger than the medium density. As argued earlier, we expect that in this situation, the medium will have only a limited effect on the particle motion. This is consistent with the small velocity change (less than or equal to 3.5%) observed for such regimes. The range of particle density where the retardation is expected to be significant - $\rho_p < \rho$ - was not studied in these works. In [54] the authors showed experimentally that the drag of very light particles in water ($\rho_p / \rho < 0.3$) can increase as much as 2.5 times compared to values predicted by the

standard drag curve (0.95 versus 0.38). This, in turn, would cause a drop in terminal velocity of the rising particle by about 30% compared to the standard drag curve.

Note that the variation in the ratio ρ_p / ρ was considered in [53] in order to determine how it affects the particle path for intermediate Re. Two classes of motion have been distinguished: zig-zag paths and helical paths (see also more recent work [35] on particle paths). A plane zig-zag trajectory is usually reported to develop first as a result of instability (e.g., [35]). As this mode itself becomes unstable, it transforms into helical path. MacCready & Jex [53] came up with the following empirical expression to describe this motion:

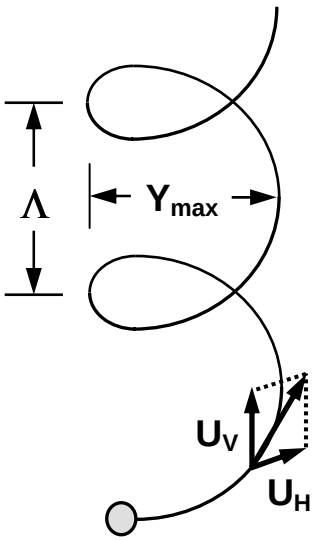

$$\frac{Y_{\max}}{\Lambda/2} = \frac{0.37}{1+2\rho_p/\rho}, \qquad (28)$$

where $Y_{\max}$, Λ - maximum amplitude of horizontal motion and vertical length of a full cycle, respectively (**Figure 7**).

Figure 7. Helical rising path

A generalized helical path can be defined as a trajectory, whose projection on a horizontal plane is an ellipse (e.g., see [35]). In this case, zig-zag motion can be considered as a special helical path for which the horizontal projection is an ellipse with zero minor axis. In this context, $Y_{\max}$ corresponds to the major axis of this ellipse. Such a generalization is convenient, because it covers a wider range of lateral motions of a rising (sinking) particle. In fact, authors in [35] reported such generalized "elliptic-helical" paths for air bubbles in water. They also noticed the slow precession of the projected ellipse, that is, the major axis $Y_{\max}$ changes direction with time.

Karamanev et al. [54] experimentally obtained the following result for light solid spherical particles ($\rho_p / \rho < 0.3$) in water:

$$\frac{Y_{\max}}{\Lambda} \approx 0.18, \tag{29}$$

which is very close to Eq.(28) for $\rho_p / \rho \to 0$.

In general, though, it is unreasonable (or non-physical) to seek an expression of the form (28). Indeed, the geometrical pattern of particle oscillations should depend not only on relative density, but also on the flow regime. For example, for sufficiently small particle diameter, no oscillations occur. So, expression (28) is just an empirical expression which can work rather well only for a limited range of physical parameters.

It is reasonable to assume the ratio $Y_{\max} / \Lambda$ affects the average terminal velocity of the rising particle. How can we quantitatively express this dependence?

Assume for a moment the particle rises in a perfectly helical path and the magnitude of the velocity is the same as for rectilinear motion. What distance would it travel vertically compared to the rectilinearly moving particle? The arc length of one period of a helix is:

$$\Delta S = \sqrt{\pi^2 Y_{\max}^2 + \Lambda^2} \tag{30a}$$

The difference of elevation between these points is just Λ:

$$\Delta L = \Lambda \tag{30b}$$

Hence, in rectilinear motion, the particle will travel a greater vertical distance during the same time period:

$$L_{rect} = L_{hel} \sqrt{\frac{\pi^2 Y_{\max}^2}{\Lambda^2} + 1} \tag{31}$$

For very light particles in water, using Eq.(29) and Eq.(31), we obtain:

$$L_{rect} \approx L_{hel}\sqrt{\pi^2(0.18)^2+1} \approx 1.15\,L_{hel}\,, \tag{32}$$

which means the standard drag curve overestimates the particle velocity by about 15%.

Experiments of Karamanev et al. [54] as well as our experiments with ping-pong balls (see Section 5.1) show, that this overestimation is actually higher – about 25-30%. But we should remember that to obtain Eq.(32), we assumed the magnitude of the particle velocity coincided with that of a rectilinearly moving particle. There is no obvious reason why this should be true. In fact, we may expect that since the particle helical path per unit height is longer than rectilinear, more energy is lost due to viscous dissipation in covering the same vertical distance. Thus, although the potential energy arising from the driving body force (buoyancy) is the same for both regimes, we expect that dissipation losses are larger for the helical path and, hence, kinetic energy per unit height is lower for the helical path. In addition, the particle path can be non-helical for certain ranges of Re, and, in fact, it is not strictly proven that what we visually identify as helical is indeed helical.

2.2 SOLID PARTICLES VERSUS DROPS AND BUBBLES

The analytical description of a fluid particle behavior in the flow field is extremely challenging. Unlike the case of a solid particle, this is a free boundary problem, where the shape of the particle itself is a part of the solution. The problem for liquid particles is therefore fundamentally different than that for solid particles. The geometrical shape of a particle is predefined by a dynamic balance, and hence the set of possible shapes is rather narrow. In some ways, this makes the study of fluid particles more attractive.

Most theoretical and numerical studies of solid particles are confined to relatively simple geometric shapes: spheres, spheroids, spherical caps, toroids, long cylinders [23, 58-62]. In general, solid particles can have any imaginable geometrical shape, including features such as sharp corners, holes, and cracks. This shape is predetermined and is not dictated by fluid-particle interaction. The particle shape must be specified for every particular application, and the solution in the near-particle field will also differ for every such case. Thus, the shape of the particle is an extra restriction, imposed on the system. Even if they have a regular shape, most solid particles are, in practice, non-uniform. As a result, their center of mass typically doesn't coincide with the geometric center. As it will be discussed in Chapter 5.0, this shift of the center of mass can appreciably change the drag of a particle in certain range of relative densities and Reynolds numbers.

On the other hand, a fluid particle is not expected to have sharp corners or odd shapes. As it follows from vast experimental material of the twentieth century (nicely summarized in [1]), fluid particle shapes can be reduced to a rather narrow set. These shapes (i.e. sphere, oblate spheroid, spherical cap) naturally emerge as a result of particle-flow interaction, and don't represent an extra restriction on the system. Any numerical results will have much more fundamental nature, than one for a solid particle, which is applicable only for a particular solid shape. In fact, the shapes of solid particles, chosen for detailed study by various researchers, often reflect possible shapes of fluid particles realized under certain physical conditions [23, 58, 59, 62].

The density is well modeled as uniform in a fluid particle (assuming no stratification). As will be discussed later (Section 5.1), the non-uniformity can have a strong effect on the particle behavior. While the non-uniformity can be excluded from the full list of parameters describing

the fluid particle, for a solid particle a mass distribution should be also taken into account for some other regimes.

The idea of this work has developed from attempts to describe the behavior of liquid CO_2 particles in the deep ocean. One may ask: if liquid drops are of interest, why is so much attention devoted to the behavior of solid spherical particles in this study? To answer this question, recall that a falling/rising solid sphere represents the limiting case of a fluid particle. Specifics of fluid particles compared to solid spheres will be discussed in detail in the following sections. For example, the liquid/liquid interface mobility changes the boundary conditions on the particle surface compared to that for a solid sphere; and the high ratio of inertia to surface tension causes significant deviations from a spherical shape for the drop. As all the features of the solid sphere behavior are inherently present as a limiting case for fluid particles, the behavior of freely moving spheres should be understood first in detail. Then, the specifics of drops and bubbles can be added.

2.3 FREE MOTION OF FLUID PARTICLES

2.3.1 Non-dimensional description for drops and bubbles. Parameters affecting drag.

In the case of a fluid particle, two additional parameters must be considered – particle material viscosity μ_p and interfacial tension γ.[6] Hence, in order to completely describe free motion of a fluid particle, two additional dimensionless numbers are required compared to the analysis of free motion of a solid sphere. Since the new parameters, μ_p and γ, represent the material

[6] In fact, a solid sphere can be considered as a limiting case of infinitely high particle viscosity and interfacial tension. This limit is equivalent to the assumption of no internal motion and no shape changes.

properties of the investigated system, it is logical to define the required dimensionless numbers as certain combinations of material parameters. Although the choice of dimensionless numbers is not unique, we will use the following pair of parameters in this work:

$$\lambda = \mu_p / \mu, \qquad Mo = \frac{\Delta\rho \mu^4 g}{\rho^2 \gamma^3}, \tag{33}$$

$\Delta\rho = \left|\rho - \rho_p\right|$ - difference of medium and particle density;

μ_p, μ - particle and medium dynamic viscosity, respectively;

γ - interfacial tension.

The former is just the particle/ medium viscosity ratio, the latter is the so called Morton number, introduced in [63] and [24] and commonly used for the description of free motion of fluid particles. The *Mo* displays a very strong dependence on the medium viscosity. Therefore, the full span of the physically achievable Morton numbers extends from 10^{-12} (rain drops) up to 10^4-10^6 (bubbles in glycerine or in sugar solutions). However, the most common physical systems – drops in the air, bubbles and drops in water – have a comparatively narrow range of *Mo*: 10^{-12}-10^{-9}.

The choice of parameters (33) is dictated by the following rational arguments. Experimental data of various researchers show that free particle motion (at least, in the non-periodic regime) is independent of the particle viscosity, unless the system is thoroughly purified or the Morton number is very large, *Mo* >100 (p.28 and p.173 of [1]). The logic behind this behavior is fairly clear: if one factor (contamination) completely suppresses interface tangential mobility, then another factor (particle viscosity) becomes irrelevant with respect to this type of interface

mobility[7]. Since most of the practical applications deal with contaminated media, it provides a motivation to eliminate (under certain conditions) the particle viscosity from consideration. For this reason, the particle viscosity appears only in one non-dimensional parameter, the viscosity ratio.

Other attempts to systematically describe free motion of fluid particles were associated with three independent dimensionless parameters (see Subsection 2.3.4 for more details). That is, the following type of functional dependence was considered:

$$C_D = C_D\left(\mathrm{Re}, Mo_{fixed}\right), \tag{34}$$

resulting in a set of dimensionless curves for various magnitudes of material parameter *Mo*. Actually, in most works devoted to this matter, another choice of dimensionless numbers was made for the functional dependence of type (34), see Subsection 2.3.4. But the philosophy is the same: create a universal graph (similar to the Moody diagram for circular pipes [64]) with Morton number as a parameter.

Unfortunately, as was shown at the beginning of this section, this approach is incomplete, and, in general, should be amended by two additional parameters. Therefore, in the most general case, the following expression should be used instead of Eq.(34):

$$C_D = C_D(\mathrm{Re}, Mo, \rho_p / \rho, \lambda) \tag{35}$$

Lastly, a note should be made on the importance of non-sphericity. Although the fluid particle shape may significantly influence the drag, it is not an independent parameter. Based on the above discussion, the shape should be uniquely defined by the complete set of dimensionless parameters:

[7] There can also be interface motion in the normal direction, caused, for example, by shape oscillations. This type of motion will not be completely suppressed by surfactants, although surfactants may alter it through the change in interfacial tension. Shape oscillations and their effect on particle motion will be discussed in more detail in Section 5.2.5.

$$C_D = C_D\left(\mathrm{Re}, Mo,\ \rho_p / \rho,\ \lambda, shape(\mathrm{Re}, Mo,\ \rho_p / \rho,\ \lambda)\right) = C_D\left(\mathrm{Re}, Mo,\ \rho_p / \rho,\ \lambda\right) \qquad (36a)$$

In contrast, for an arbitrary solid particle:

$$C_D = C_D\left(\mathrm{Re}, \rho_p / \rho,\ shape\right) \qquad (36b)$$

Of course, to attain a better understanding of the physics, it's extremely useful to have more information about the function $shape(\mathrm{Re}, Mo,\ \rho_p / \rho,\ \lambda)$ for a fluid particle, but this information is not necessary to build drag curves.

In this regard, it is advantageous to use an equivalent diameter introduced in Eq.(14) for fluid particles. Then, the solution is independent of the particular shape of the particle, which itself must be a part of the solution. The only known quantitative information about the particle is the amount of material in it.

Summarizing the above considerations, we can conclude that in the most general case the drag curve of type (34) is not complete without the addition of extra parameters. Particle/ medium viscosity and density ratios represent these additional dimensions for the drag curve.

In a surfactant-free environment, the viscosity ratio affects the particles drag (and therefore, the terminal velocity) through the interface mobility, as already mentioned in Section 1.3. This factor is closely related to the internal particle circulation. The kinetic energy of the flow past the particle is transmitted to the interior of the particle through the interface. This causes internal circulation of a certain intensity inside the liquid/gaseous particle. The mobile interface decreases both form drag and friction drag compared to the corresponding solid sphere (see discussion and references in subsection 5.III of [1]):

a) Reduction of the form drag is most probably caused by the shift of flow separation line towards the rear of the particle. The moving interface delays the separation of the

boundary layer. Thus, the recirculation zone at the rear of the sphere is smaller than for a corresponding rigid particle.

b) Skin friction is also reduced, because the gradient of the tangential velocity on the mobile boundary is lower than for the corresponding solid particle.

As discussed in Section 2.1, particle/ medium density ratio (or relative particle inertia) becomes important only for unsteady motion and it affects the ability of the particle to follow periodic flow fluctuations. Additional lateral motion of a rising/ sinking particle in a periodic regime reduces the averaged terminal velocity of rise/ fall and, hence, increases the average drag.

The following three subsections offer a detailed discussion of the interfacial mobility, viscosity ratio, and relative inertia.

2.3.2 Effect of Surface Active Impurities

If not subjected to a special purification process, any real fluid system contains traces of surface active materials called surfactants. Surfactants tend to accumulate on the interface separating two media and affect interface mobility [25, 26]. Circulation inside the particle implies a toroidal type of motion, causing the surfactant molecules to be entrained inside the particle. Due to the dual hydrophilic/hydrophobic nature of these molecules, they resist departure from the interface and, consequently, this entrainment. As a result, they accumulate at the rear of the particle and retard the circulatory motion [28]. As stated in [27], both the terminal and the interfacial velocity of a droplet are reduced, compared to motion in a pure liquid (the interfacial velocity particularly near the rear of the droplet). High flow velocity around the particle may wash the surfactants from the interface, causing some restoration of the interface mobility.

Figure 8 illustrates the effect of interface mobility on particle drag. It compares drag curves for air bubbles in ordinary tap water versus air bubbles in thoroughly purified water [24, 38].

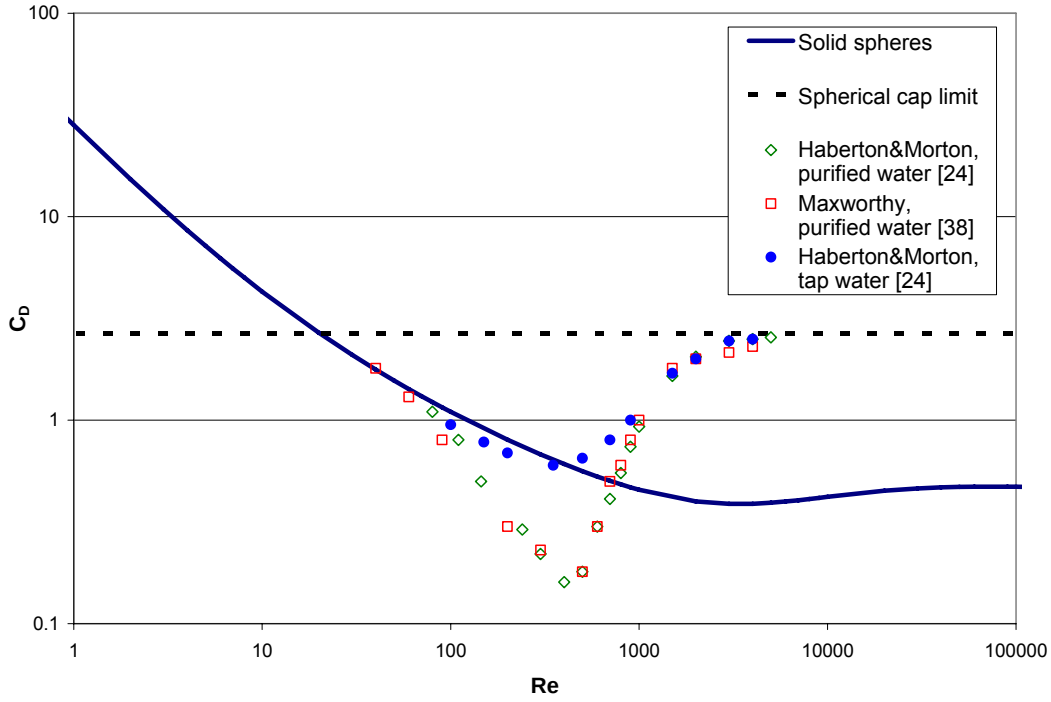

Figure 8. Drag coefficient for air bubbles in water

Indeed, the bubble drag in the purified water is significantly lower – it even falls below the standard drag curve. It is interesting that drag curves from works [24] and [38] (40 years apart!), for bubbles in thoroughly purified water, fit each other quite well. Air viscosity is very small compared to that of water, which causes intense tangential motion of the interface. High interface mobility is not suppressed by surfactants, because of the high level of purification. Therefore, the drag curve for bubbles in purified water falls below the standard drag curve for solid spheres in the range of intermediate Re numbers. Eventually, for higher Re, as the particle deformation and periodic motion come into play, the C_D starts to grow and exceeds the drag for solid spheres. On the other hand, the drag curve for bubbles in contaminated water practically never drops below

the standard curve. At certain point the drag curve starts to exceed the standard curve, which corresponds to a noticeable deviation from a spherical shape and/or change of the rising regime.

As discussed in 2.3.1, it is a widely accepted point of view that particle/ medium viscosity ratio can be neglected unless we deal with thoroughly purified system or if Mo >100. This statement remains to be verified for the full range of Reynolds numbers. For example, we may argue that surfactants reduce, but do not completely eliminate internal circulation. Especially for moderate Reynolds numbers, the energy of the external flow may be enough to drive the internal particle material even in the presence of surfactants (or may wash out the surfactants). In this scenario, internal circulation may increase with the growth of Re, and have a large effect for lower particle viscosities. Thus, particle viscosity may come into play. Also, tangential motion of the interface is not the only process affected by the particle viscosity. For instance, an unsteady flow around the particle can potentially trigger shape oscillations. If present, these oscillations may alter the particle periodic motion and, hence, the drag. The higher particle viscosity would tend to attenuate or completely suppress shape oscillations.

Although omitting the parameter λ (even for sufficiently contaminated media) may require more rigorous analysis, we accept this approach here as a starting point. We'll return to the effect of particle viscosity, in Sections 2.3.3 and 5.2.5.

It's useful to mention that drag in the spherical cap regime should not vary noticeably with circulation intensity. Indeed, at this high level of inertia, skin friction is just a negligible fraction of the overall drag, so it won't change the drag significantly. The separation point for a spherical cap also won't change – it will always be at the edge of the cap. Therefore, it's reasonable to expect that drag curves may vary as we vary the level of contamination, but they merge together in the spherical cap regime. It is necessary to emphasize that the above arguments are valid only

if we admit a universal shape of the cap for the inertial regime (cap angle about 52°). Note that available experimental results (at least for the air bubbles) seem to support this hypothesis (i.e., see **Figure 8**).[8]

2.3.3 Effect of Viscosity Ratio on Motion of Fluid Particles

The effect of the particle/medium viscosity ratio $\lambda = \mu_p / \mu$ on particle drag was briefly discussed in Section 1.3. Assuming continuity of the tangential stress over the boundary of the particle, we have:

$$\mu_p \frac{\partial u_{in}}{dy} = \mu \frac{\partial u_{out}}{dy}, \tag{37}$$

where the *y*-axis is normal to the interface, u_{in} and u_{out} are tangential velocities inside and outside of the particle, respectively. Then, if the particle viscosity is much larger than that of the surrounding fluid, the internal circulation may be negligible.

An interesting numerical study was performed by Feng & Michaelides [65] on spherical liquid particles. These authors assumed that particles don't deviate from a spherical shape and the interface between the particle and carrying fluid is "perfectly clean" (no surfactants). The effect of the viscosity ratio ($\lambda = \mu_p / \mu$) on the particle drag coefficient was then examined for intermediate Reynolds numbers. The numerical domain was divided into a thin boundary layer (dimensionless thickness $\approx (\mathrm{Re})^{-1/2}$) and the rest of the domain filled with an ideal fluid. Basically, this numerical study is an extension of analytical Hadamard-Rybczinski solution towards higher Reynolds numbers and further development of Levich's approach (see Section

[8] Applicability of the universal spherical cap limit for particles with non-negligible inertia (ρ_p *not* $<< \rho$) is somewhat discussed in Section 2.3.4 and.2.3.5.

1.3 or pp.436-448 of [25]). Based on their numerical results, the authors suggested the following engineering correlation for the drag coefficient of spherical, "perfectly clean" fluid particles in a continuous medium:

$$\begin{cases} C_D(\mathrm{Re},\lambda) = \dfrac{2-\lambda}{2} C_D(\mathrm{Re},0) + \dfrac{4\lambda}{6+\lambda} C_D(\mathrm{Re},2), \quad \text{for } 0 \le \lambda \le 2, \quad \mathrm{Re} < 1000 \\ C_D(\mathrm{Re},\lambda) = \dfrac{4}{\lambda+2} C_D(\mathrm{Re},2) + \dfrac{\lambda-2}{\lambda+2} C_D(\mathrm{Re},\infty), \quad \text{for } 2 \le \lambda \le \infty, \quad \mathrm{Re} < 1000 \end{cases} \tag{38a}$$

where:

$$\begin{cases} C_D(\mathrm{Re},0) = \dfrac{48}{\mathrm{Re}}\left(1 + \dfrac{2.21}{\sqrt{\mathrm{Re}}} - \dfrac{2.14}{\mathrm{Re}}\right) \\ C_D(\mathrm{Re},2) = 17.0\,\mathrm{Re}^{-2/3} \\ C_D(\mathrm{Re},\infty) = \dfrac{24}{\mathrm{Re}}\left(1 + \dfrac{1}{6}\mathrm{Re}^{2/3}\right) \end{cases} \tag{38b}$$

Note that in the first approximation Eq.(38b) for $\lambda = 0$ coincides with Levich's theory (see Eq.(12a)).

Drag curves based on this correlation for different magnitudes of the viscosity ratio λ are shown in **Figure 9**:

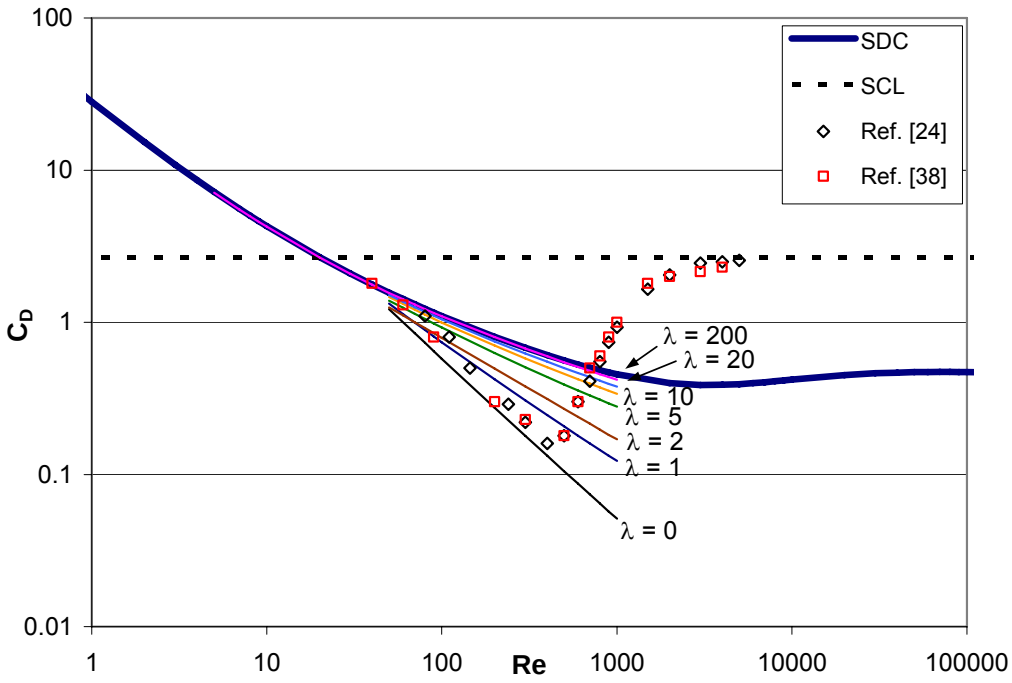

Figure 9. Drag for spherical fluid particles in purified medium. Solid lines represent correlation (38) for various magnitudes of viscosity ratio, λ. For comparison, the experimental results of Maxworthy [38] and Haberton & Morton [24] for air bubbles are shown. (SDC – standard drag curve, SCL – spherical cap limit)

As we discussed earlier, the drag coefficient in the rectilinear regime may be affected by three factors: viscosity ratio, presence of surfactants, and particle shape change (through material parameters, see Eq.(36a)). These authors deliberately eliminated the last two factors to reveal the effect of the viscosity ratio on the particle drag. Although real systems in most situations can't be reduced to this simplified model, it serves as a very important limiting case. As the relative particle viscosity λ decreases, the interface mobility increases, causing a drop in the drag coefficient, **Figure 9**.

It's interesting to compare the correlation curve for $\lambda = 0$ and experimental drag curves for air bubbles in purified water (**Figure 8**). In the regions, where the air bubbles are nearly spherical, these curves match each other rather well. Slightly higher values of drag for the real air

bubbles system can be explained by traces of surfactants, which can't be completely eliminated from water. On the other hand, for higher values of λ, the drag curve (38) approaches the classical curve for solid spheres (**Figure 9**).

Based on Eq.(38), we conclude that for $\lambda > 20$ the drag curve is nearly independent of the viscosity ratio. Or, in other words, interface mobility is negligible. This observation can be used for experimental modeling of another limiting case. Namely, if we use very viscous fluids for the particle ($\lambda > 20$), then the interface is practically immobile, and the only parameter affecting the drag curve is the particle shape. This separation of effects is very important. Such a case is considered in Section 5.3 based on experiments with oil droplets ($\lambda > 40$).

As a final comment, the correlation (38a,b) should be considered with some precaution, because it was obtained assuming axial symmetry of the solution. For solid spheres, instability of axisymmetric solution occurs at Re=212. We were not able to find any numerical work devoted to the onset of asymmetric solutions for fluid spheres. Due to interface mobility, we would expect that the instability occurs at higher values of Re than for the solid sphere, although probably still lower than Re=1000.

2.3.4 Drops versus Bubbles – Significance of Particle Inertia

To avoid complications related to the interface mobility, it can be very useful to build a set of universal drag curves for "sufficiently contaminated" carrying fluid or "very viscous" particles.

As discussed in earlier sections, out of three factors (interface mobility, non-sphericity, non-rectilinearity) responsible for the drag deviation from the SDC, only one – interface mobility – has been shown experimentally to cause drag reduction. Thus, if the interface mobility is not an

issue, it's reasonable to expect the drag curve for such a particle is never below the SDC and asymptotically approaches the spherical cap limit of 8/3 for large Re[9].

Various authors have attempted to create a universal set of drag curves $C_D = C_D(\mathrm{Re}, Mo)$ for contaminated systems or even $C_D = C_D(\mathrm{Re}, Mo, \lambda)$ for purified media. However, these curves do not give satisfactory results even for cases with immobile interface. Why? The most advanced attempts were undertaken in [66-68] (see Appendix B for details). **Figure 10** (reproduced from p.27 of [1]) shows a popular diagram based on correlations developed in [66-68]. The most striking feature of these correlations is a three-parametric approach. The choice of the non-dimensional numbers is not unique, and the authors found it more convenient to use the Eotvos number, *Eo*, instead of the drag coefficient C_D. Thus, the fluid particle behavior was described by:

$$\mathrm{Re} = \mathrm{Re}(Eo, Mo), \tag{39}$$

where:
$$Eo = \frac{\Delta\rho\, g\, D_{eq}^2}{\gamma}\left[= \frac{\text{Buoyancy}}{\text{Surface tension}}\right] \tag{40}$$

The functional dependence used in Eq.(39) can be easily converted to the form $C_D = C_D(\mathrm{Re}, Mo)$, using the relation between dimensionless numbers:

$$Mo = \frac{16}{9}\frac{Eo^3}{C_D^2\,\mathrm{Re}^4} \tag{41}$$

[9] Again, the limit of 8/3 is applicable if we admit as a working hypothesis the universal shape (≈ 52° spherical cap) of a large fluid particle in the limit of purely inertial regime. Unfortunately, there has been very little experimental work on large liquid drops, so we cannot confidently affirm the same shape in the inertial regime. Such lack of experiments is partially caused by limitations of structural integrity of large drops. They break apart readily for much lower Re than gas bubbles. In fact, slight overshooting of the C_D=8/3 limit was observed in some experiments with liquid drops, including our experiments.

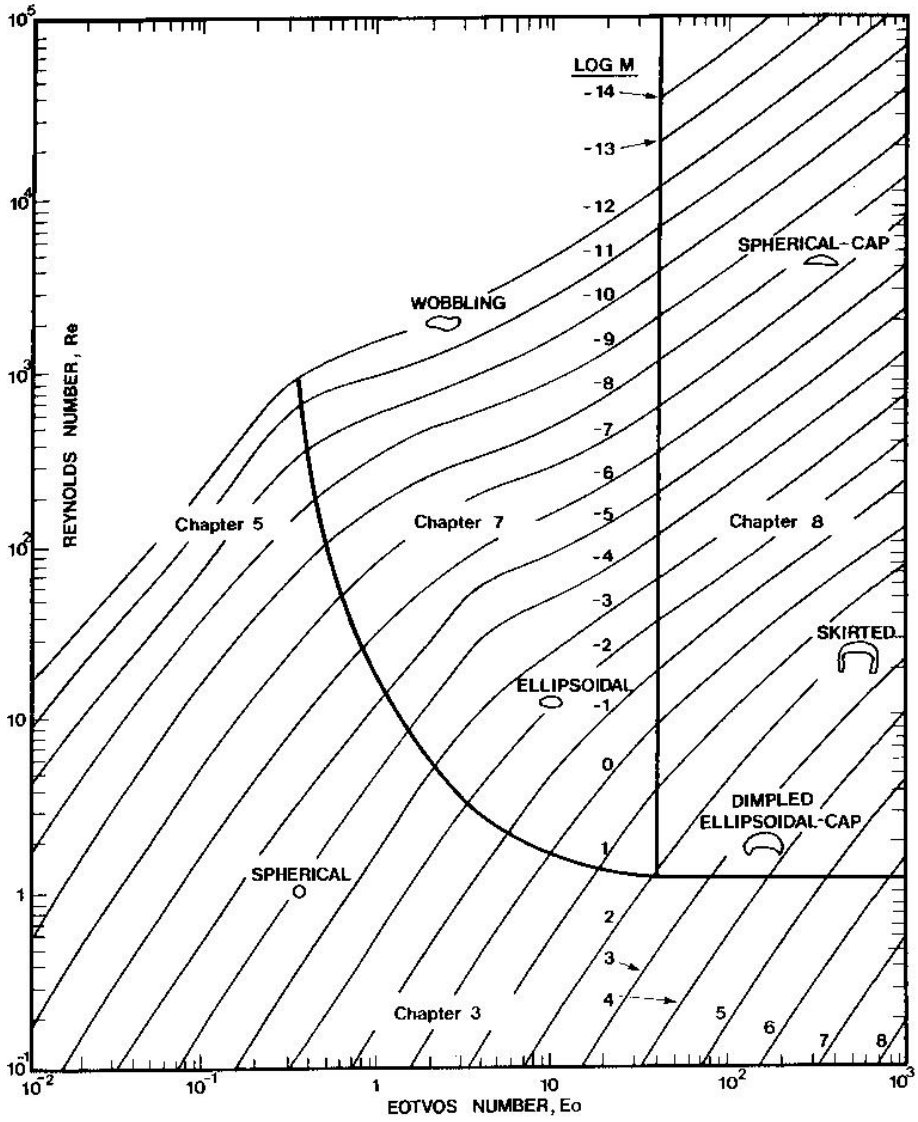

Figure 10. Shape regimes for bubbles and drops (reproduced from p.27 of [1])

Basically, **Figure 10** is a "three-parameter" attempt to unify all the drops and bubbles "under one roof". For example, based on this figure, gaseous and liquid particles fit the same drag curve if they have the same Morton number. The problem in this formulation is similar to the problem of reversing buoyancy for a solid sphere, considered in Section 2.1. Indeed, would rising and falling fluid particles with the same magnitude of *Mo* behave identically?

We already anticipate a negative answer to this question from the previous discussion, but we now consider relevant experiments. Consider the existing experimental results for drops and bubbles moving in quiescent liquids. Below, several typical drag curves are reproduced from experimental works [24, 69-72] of the second half of the twentieth century (**Figure 11**).

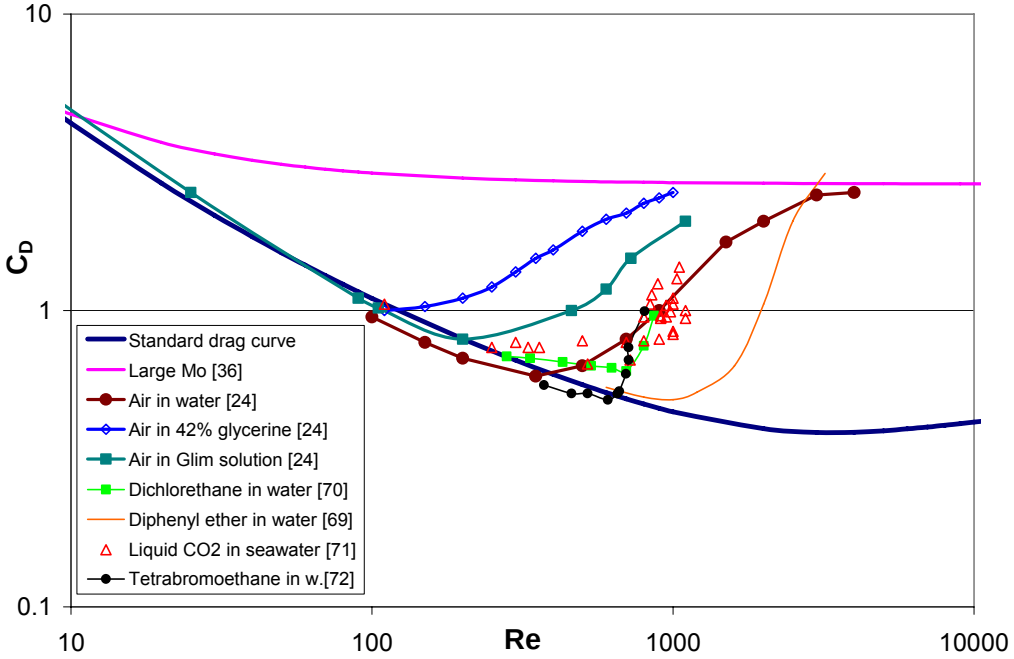

Figure 11. Qualitative difference of drag curves for bubbles and drops (contaminated systems)

Even without knowledge of the Morton number for every particular curve, one can easily see that the liquid drops appear to behave qualitatively differently from bubbles. Due to the large difference in behavior, it is common to separately study bubbles in liquids [36, 38], drops in air [73, 74], or drops in liquids [66, 67, 72] and often to develop distinct correlations for each case. Investigators sometimes suggest that different mechanisms might determine the particle motion and stability for each case. For example, in the recent work [75], the author states that ”the large difference in the critical Reynolds number for drops … and bubbles … is a strong indication that different mechanisms might determine the path instability.”

However, from a fundamental point of view, there is no difference between the above mentioned cases (as long as the effects of compressibility are insignificant). All these cases represent motion of fluid particles in a continuous media. If the dimensionless material parameter (Morton number) is the same and the internal particle viscosity can be neglected, then the only difference between these three cases will be density ratio, ρ_p / ρ : <<1 for bubbles in liquids; ≈1 for drops in liquids; >>1 for drops in gases. Hence, in the rectilinear regime of motion, we would expect all three cases to fit the same drag curve. It will be shown in later chapters, that the transition from the rectilinear to the periodic motion occurs differently even for particles with the same Morton number. The onset of instability of the rectilinear motion and quantitative characteristics of periodic behavior depend on particle inertia with respect to the medium (that is, their density ratio). This observation is similar to that for solid spheres: particle inertia becomes important, when the Re exceeds a critical value.

Applying these results to the problem of CO_2 particles in the ocean (discussed briefly in Section 1.0), we see the drag laws for CO_2 particles in liquid and gaseous phase will be qualitatively different. **Figure 11** has only particles with densities either greater than 0.9 g/cm^3 or less than 0.1 g/cm^3. From a fundamental point of view, it would be quite useful to have drag curves in the intermediate density range ($0.1 < \rho < 0.9$ g/cm^3). Although we may hypothesize how the shape of the curve changes in the intermediate range, experiments are needed to confirm these expectations. Since it is quite difficult to find a common liquid with such density, there are practically no experimental works in this range. In the process of carbon dioxide sequestration, this intermediate range of particle density can be achieved, if we consider the possibility of thermal vents in the vicinity of the CO_2 release. In this case, CO_2 particles at the depth of about 1,000 m can have a density around 0.5-0.6 g/cm^3.

As seen in Appendix B and **Figure 10**, the models developed in [66-68] don't adequately reflect the behavior of fluid particles in the most challenging transitional region (marked and denoted by wobbling and ellipsoidal particles in **Figure 10**). These transitional curves are shown as lines that smoothly connect the regions of spherical and spherical cap regimes and provide representative mean values for bubbles and drops with fixed *Mo*. In fact, the authors realize the limitations of this chart by noting, for example, that it is not applicable for liquid drops falling in gases.

Thus, the problem of free motion of liquid/gaseous particles in quiescent liquids under conditions of an immobile interface must involve at least[10] four non-dimensional parameters: C_D, Re, *Mo*, and ρ_p / ρ:

$$C_D = C_D\left(\mathrm{Re}, Mo, \rho_p / \rho\right) \tag{42}$$

To obtain these parametric curves, several sets of experiments should be performed for different density ratios and different Morton numbers.

A more detailed discussion about the physics of fluid particles for different ranges of parameters (e.g., deviation from the standard drag, shape change, unsteady rising regime) is left until Chapter 5.0, where our experimental results are provided.

2.3.5 "Large *Mo*" limit (LML)

Lastly in this chapter we would like to discuss in more detail the existence of an upper bound for the drag of fluid particles. In the 70s through early 80s various researchers in McGill University, Montreal, P.Q., Canada (including Grace [68], Wairegi [37], Bhaga & Weber [36]) studied free motion of fluid particles in various media for large values of Morton number. Several interesting

[10] Possibly, as many as five parameters, because neglecting the viscosity ratio in the most general case remains unjustified (see 2.3.2 and 5.2.5).

results were found during these studies. Experiments with air bubbles in viscous liquids by Bhaga et al. [36] have revealed that for any *Mo* larger than approximately $4 \cdot 10^{-3}$ the drag curves coincide and are functions only of the Reynolds number. The curve fit of these results is shown in **Figure 11** and is represented by the following formula:

$$C_D = \left[(2.67)^{0.9} + \left(\frac{16}{\mathrm{Re}} \right)^{0.9} \right]^{1/0.9} \tag{43}$$

However, this study was limited to air bubbles. According to our earlier discussion (Section 2.3.4), we would expect any fluid particle to tend to the same limit for large enough *Mo*. A very extensive experimental study was described in the PhD dissertation of Wairegi [37]. Various freely rising and sinking liquid droplets were considered in different media for a very wide range of Morton number $5 \cdot 10^{-12} < Mo < 2350$. The author did not provide a systematic representation of these results in terms of drag curves. Therefore, we had to use the tables of experimental data provided in [37] to create the $C_D(Re)$ curve for their data. **Figure 12** depicts the experimental data from [37] in the range $10^{-4} < Mo < 2350$ along with the experimental fit (43) for air bubbles. Although the dispersion of the data is quite large, it seems to follow the same trend as the previously introduced curve for air bubbles at large *Mo*.

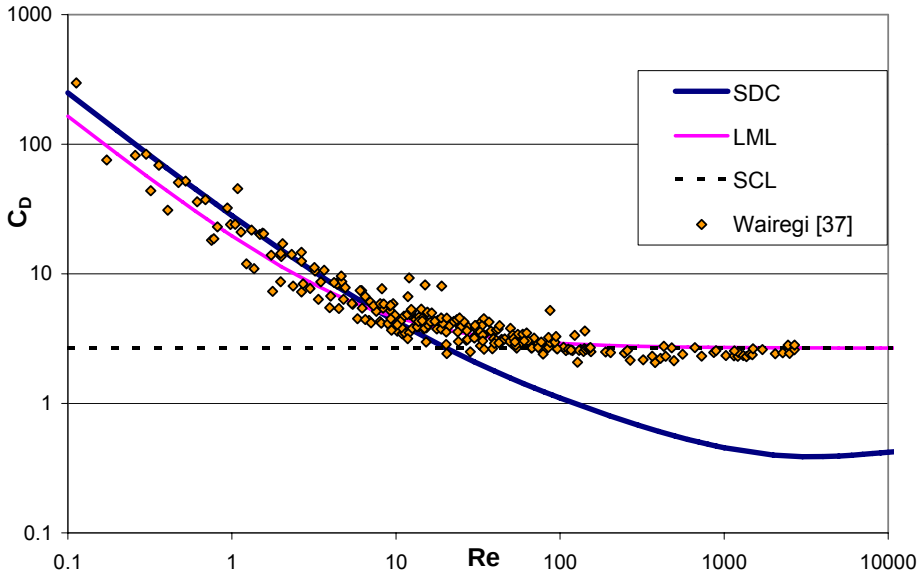

Figure 12. Behavior of fluid particles at large Mo: Eq.(43) for air bubbles (LML) and experiments [37] for liquid drops: $10^{-4} < Mo < 2350$ (SDC – standard drag curve; LML – large Morton limit; SCL – spherical cap limit)

Why is the large *Mo* chosen as a possible limiting case for the free motion of fluid particles in continuous media? Based on physical grounds, a large *Mo* implies a highly deformable particle even with low flow around it. Indeed, large magnitudes of *Mo* mean that viscous forces in the medium significantly overcome the interfacial tension. This causes a strong distortion of a fluid particle even in the regime of a relatively low Re. Thus, LML means, loosely speaking, the "maximum possible deformability" permitted by physical laws. Quotes are used, because "maximum possible deformability" is not a clearly defined term so far. Besides *Mo*, another factor causing strong particle deformation is the high Re. As discussed in Section 1.3, in this limit the drag is independent of Re and the "maximum possible deformability" is just a horizontal line $C_D=8/3$ (Spherical Cap Limit or SCL). As expected, the experimental fit for large *Mo* (43) converges to the SCL when Re increases.

As for the theoretical (analytical) treatment of this problem, the most recent advance was made by D.D. Joseph [76]. He extended the gas bubble analysis of Davis & Taylor which was

based on inviscid potential flow to viscous potential flow and derived a more general formula that includes a kinematic viscosity of the medium, $\nu = \mu / \rho$:

$$U_{term} = -\frac{4}{3}\frac{\nu}{R_f} + \sqrt{\frac{4}{9}gR + \frac{16}{9}\frac{\nu^2}{R_f^2}}\,, \tag{44}$$

where R_f is radius of curvature of the front end of bubble (either spherical, ellipsoidal or spherical cap). Note that this analysis was performed for a gas bubble, that is, $\Delta\rho = \rho - \rho_p \approx \rho$.

When inertial effects dominate over the viscous ones, Eq.(44) reduces to the Davis & Taylor solution (13a). In the other extreme, if viscosity effects are much larger than gravitational effects, a well known solution for the viscous regime obtained by Moore [77] is matched:

$$U_{term} = \frac{1}{6}\frac{gR_f^2}{\nu}\,. \tag{45}$$

Equation (44) rewritten in terms of drag takes the form:

$$C_D^f = 6 + 32/\mathrm{Re}_f\,. \tag{46}$$

However, both the drag coefficient and Reynolds number are expressed in terms of the radius, R_f, of the bubble front. In order to rewrite them in terms of equivalent radius, R_{eq}, we need to know the relation: $K=R_{eq}/R_f$. Various experiments with fluid particles in highly viscous media (pp.24-25 & pp.203-204 of [1]) show the shape of a fluid particle can, with reasonable precision, be approximated by a segment of a sphere (see **Figure 47**). Then, the coefficient K can be found as following (see Appendix A):

$$K = \frac{R_{eq}}{R_f} = \left(\frac{1}{16}\right)^{1/3}\left(8 + \cos 3\varphi_o - 9\cos\varphi_o\right)^{1/3} \tag{47}$$

Substitution of $C_D^{eq} = K \cdot C_D^f$ and $\mathrm{Re}_{eq} = K \cdot \mathrm{Re}_f$ into Eq.(46) gives:

$$C_D^{eq} = 6K + 32K^2/\mathrm{Re}_{eq}\,. \tag{48}$$

As discussed in Section 1.3 and Appendix A, in the inertial regime of high Re the particle has a universal shape, which is characterized by the angle $\varphi_o \approx 50^o$ (see **Figure 47**). Hence, $K \approx 0.45$. As a result, from Eq.(48) we obtain approximately the same prediction of constant drag in the inertial regime as in Appendix A:

$$C_D \approx 2.7 + 6.5/\mathrm{Re}, \quad \mathrm{Re} > 200, \tag{49}$$

where super- and subscripts "*eq*" are omitted for brevity. In the following text $C_D = C_D^{eq}$ and $\mathrm{Re} = \mathrm{Re}_{eq}$ are implied for non-spherical fluid particle, unless stated otherwise.

The important difference from Appendix A is that the drag involves a hyperbolic term, so the drag monotonically increases from 2.7 as Re decreases. However, there is another complication: numerous researches have shown that, for Re<150, the angle φ_o is not a constant. In fact, it increases for smaller Re. The approximate fit $\varphi_o(\mathrm{Re})$ was obtained by averaging numerous experimental results (p.204 of [1]):

$$\varphi_o = 50 + 190 \cdot \exp\left(-0.62 \cdot \mathrm{Re}^{0.4}\right), \quad \mathrm{Re} > 1.2 \tag{50}$$

Loosely speaking, as the Re decreases from 150, the shape of a bubble gradually changes from spherical cap with $\varphi_o \approx 50^o$ towards a spherical particle with $\varphi_o \approx 180^o$ and K gradually increases from 0.45 to 1.

For sufficiently small Re, when the particle is spherical, we have K=1 and Eq.(48) approaches the following limit:

$$C_D = 6 + 32/\mathrm{Re} \tag{51}$$

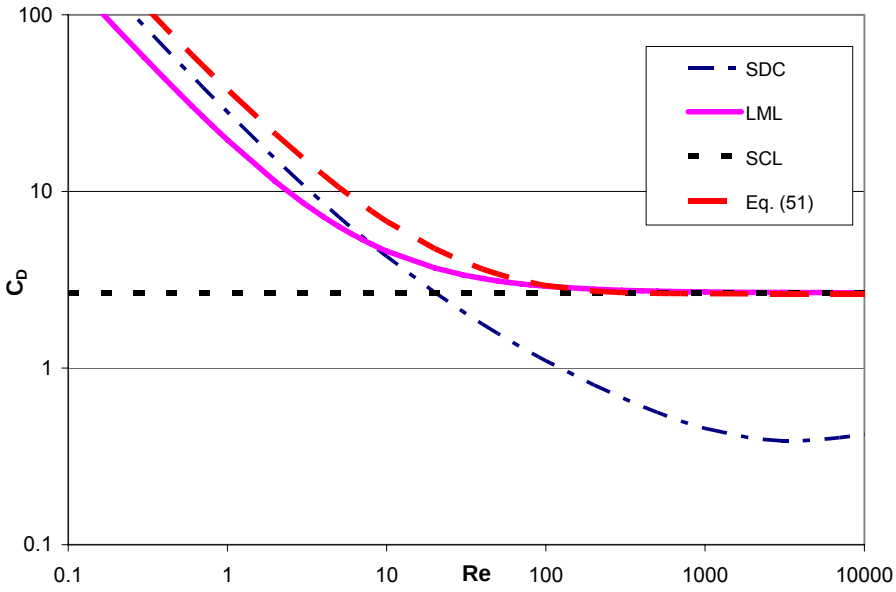

Figure 13. Comparison of experimental curve for large *Mo* (43), LML, and Eq.(51) (SDC – standard drag curve; LML – large Morton limit; SCL – spherical cap limit)

This limit does not coincide with the experimental data where C_D tends to approach 16/Re for small Re (**Figure 13**). But we have to recall that the viscous potential approach is not expected to provide good results for creeping flows. Instead, the Hadamard-Rybczynski solution should be applied. Although, in the presence of the contaminants, limit 16/Re is not usually realized due to interface immobility (Sections 1.3 and 2.3.2), we can argue that in the case of a very viscous medium this effect is overwhelmed by high viscous stresses on the boundary.

Based on the above discussion, the curve (43) can be suggested as a universal limit for freely moving liquid/ gaseous particles. Although these results seem likely, there is no strict proof that all the liquid and gaseous particles approach this limit for high enough Re. For example, to the best of our knowledge, no one has observed a "reversed spherical cap", that is, a spherical cap regime for the falling drop. This may be due to the fact that heavy drops break up at rather low Re. Even if this limit is indeed universal, it is important to reveal the character of convergence to this limit for different drop/bubble drag curves. In particular, is this limit an upper bound curve,

or can particular drag curves overshoot it at certain values of Re? In fact, some experimental results (i.e. [69] or our experiments reported in Section 5.2) show that under certain conditions drag curves for liquid particles can overshoot the limiting curve (43).

3.0 OBJECTIVES

3.1 EXPLORATION OF FUNDAMENTAL PHYSICS OF PARTICLE MOTION

Based on the above discussion, the following strategic goals were formulated for the present work:

I. Systematically investigate and quantify the effect of density ratio on the drag of solid spheres. Build a set of drag curves for solid spherical particles with density ratio as a parameter. Determine whether curves with the same density ratio are nearly coincident. Pay special attention to the peculiarities of particle behavior in the transitional region from rectilinear to periodic motion. Investigate the possibility of existence of the upper drag limit for large Re similar to spherical cap limit for fluid particles.

II. Consider fluid particle drag as a generalization of drag for solid spheres (the possibility of shape change is included). Quantitatively investigate the drag dependence on the Morton number[11] and density ratio. Try to reduce the number of independent parameters by eliminating or minimizing the effect of interface mobility (this effect can be investigated later in a separate study). Pay special attention to the peculiarities of particle behavior in the transitional region (between spherical and spherical cap regimes).

[11] Covering a full range of physically achievable Morton numbers can be an overwhelming task for this work. Therefore, a goal was set to consider just several magnitudes of Mo in the "most common" range. In future studies, this range can be extended.

In terms of the experimental work, the following experiments were planned in order to achieve the goals outlined above:

1. Series of experiments with freely moving solid spheres:
    a) For fixed particle density, obtain the terminal velocities for particles of different sizes and build a drag curve for this particular density ratio over as large a range of Re as possible;
    b) Repeat the above set of experiments for other values of particle density (ρ_p / ρ = 0.8-0.99; 0.4-0.5; <0.1);
    c) Perform pairs of experiments which differ only by the sign of $\Delta\rho / \rho$; compare pairs of curves with the same magnitude but opposite signs of $\Delta\rho / \rho$ (rising versus falling);
    d) Consider the limiting case $\rho_p / \rho \to 0$ for a fixed medium. Attempt to develop an experimental model of a spherical void in a weightless rigid shell;
2. Experiments with various materials of fluid particles for the maximum possible range of Reynolds numbers:
    a) For the fixed material parameters, run experiments with various particle sizes to build a drag curve $C_D = C_D\left(\mathrm{Re}, Mo_{fixed}, \left(\rho_p / \rho\right)_{fixed}\right)$;
    b) Repeat the above set of experiments for other values of ρ_p / ρ keeping *Mo* the same;
    c) Compare the behavior of drag curves for systems having the same *Mo* but different density ratios. Analyze whether they follow the same trends as the curves for solid spheres.

For all the experiments, the regime of motion (e.g., rectilinear, zig-zag, helical) and particle shape change (if applicable) was tracked in order to relate these changes to the qualitative characteristics of the drag curve.

As a result of this experimental investigation, the following open questions were expected to be answered:

1. Will addition of the density ratio to the 3-parametric approach give a unique description of fluid particle motion? In other words, will all systems with identical *Mo* and ρ_p / ρ obey the same drag curve for the full range of Re?[12]
2. What are the characteristics of the drag curve in the intermediate regime (between SDC and LML)[13]? What qualitative changes does increased particle inertia cause on the shape of the drag curve? Why?
3. If there are any other factors affecting the behavior of the drag curve in some sub-range of Re, what are their mechanisms and the criteria for their importance?
4. Is the LML a universal asymptote for all fluid particles, where all the drag curves converge for large enough Re? If yes, then what's the character of this convergence?
5. What are the drag curves for solid spheres in the limit of $\rho_p << \rho$? How strongly are they functions of ρ, and how much do they deviate from the standard drag curve?

[12] For example, particle viscosity can become important for some range of Re (Section 5.2.5); even small non-uniformity in density plays a big role in some cases and purity of particles may be important (Section 5.1); finally, the variation of the level of perturbations in the system may cause instability of the drag curve at different values of Re (Section 5.2.4).

[13] For fluid particles, only contaminated systems are considered, so the drag is assumed to stay always above the SDC.

3.2 APPLICATION TO CO_2 SEQUESTRATION RESEARCH

The other major set of goals for the present paper was directly related to CO_2 particle motion in the deep ocean environment. To study the behavior of such particles, a High Pressure Water Tunnel (HWT) was designed and constructed at the NETL (details of the HWT will be given in Section 4.2). The ultimate goal was to maintain a buoyant CO_2 particle in the test section of the HWT for long-term observations (up to several hours). To achieve this, a countercurrent flow must be generated in order to balance the buoyant force on the particle. For the particle to remain within a viewing window, a certain level of particle stability in both the lateral and axial direction is required. In addition, it was desirable to keep the relative particle motion as similar to that expected in the ocean as possible. The second goal is the most challenging, as it requires design and optimization of techniques for stabilization in both axial and lateral directions. Also, there is no guarantee that the optimal design for certain particle size and system conditions will work well for other sizes and conditions.

To investigate the stability problem and to explore various configurations of flow conditioners (used to create a velocity field conducive to the above design criterion), it was helpful to perform a set of preliminary experiments with corn oil in a Low Pressure Water Tunnel (LWT, see Section 4.2 for details). LWT features (geometry, etc.) resemble the HWT, but the absence of high pressure makes it possible to construct the walls of the tunnel with transparent plastic and to use modular components for easy observations and design changes. Properties of corn and castor oils in water responsible for hydrodynamic behavior[14] are surprisingly close to those of CO_2 at depths of 1,000 and 1,500 m [4], so it seemed to be a proper material for simulations.

[14] Based on the ideas of Section 2.3, we are talking first of all about the similarity of the Morton numbers and the density ratios.

Approximation of solid sphere seems feasible when we consider a small almost spherical CO_2 particle in non-purified medium. The presence of hydrate shells on CO_2 particles acts to restrict shape change, so that such particles are expected to be hydrodynamically more similar to solid spheres. Thus, experiments with solid spheres in the LWT may shed some light on the stability issues in above mentioned regimes.

Summary:

To resolve the stability issues, to design a suitable profile for various particles, and to understand the physics of drop behavior in specific velocity profiles, the following work should be done:

1. Using the LWT, investigate several configurations of the test section and choose one, which seems to work best with the widest range of particle sizes and densities. Specifically, address the following issues:
    a) vertical (axial) stabilization and ways to improve it (passive and active stabilization);
    b) horizontal (lateral) stabilization – choice of flow conditioner.
2. Perform a set of experiments in the LWT for solid spheres of several sizes and densities with the chosen flow conditioner. Report the peculiarities of particle behavior.
3. Assess the stability of fluid particles (oil drops) in the above mentioned configuration in the LWT
4. Perform a set of experiments in the HWT for CO_2 droplets of various sizes under different conditions (pressure, temperature) and classify this data (e.g., effect of the particle size/ shape and velocity profile on the stabilization issues).

4.0 EXPERIMENTAL FACILITY AND PROCEDURES

Two experimental facilities located at the National Energy Technology Laboratory (NETL), Pittsburgh, PA of the US DOE are described below – an 8' tall water tank and a High Pressure Water Tunnel (HWT). The former is a facility, operated under atmospheric pressure and is intended mostly for the fundamental research on particle motion in a quiescent medium. The latter is a one of a kind facility created for the long term residence simulation of CO_2 drops (and possibly other fluid particles) in the deep ocean (down to 3,500 meters). The applied goal of this work, related to a successful operation of the HWT, is to investigate the buoyant fluid particle behavior in countercurrent gradient flows.

4.1 WATER TANK

An experimental unit for studying the motion of solid/liquid/gaseous particles in a quiescent medium was designed and built at the NETL of the US DOE. The experimental vessel is a transparent plexiglass tank of 28cm x 28cm square cross section and 245 cm height with open top (**Figure 14**). Experiments in the tank were performed at room temperature. Typical variance of temperature during each set of experiments did not exceed 0.5°C. Buoyant fluid particles or solid balls are released at the bottom of the tank. Heavy particles are dropped through the open top of the tank or released from nozzles. The motion of the particle is recorded by two video cameras, located at selected heights and distances from the tank wall in mutually perpendicular

directions (see Section 4.1.2 for details). The key parameters to be obtained from the experiments are particle volume and terminal velocity. As the particle motion is video recorded, information about the particle trajectory and shape can also be obtained.

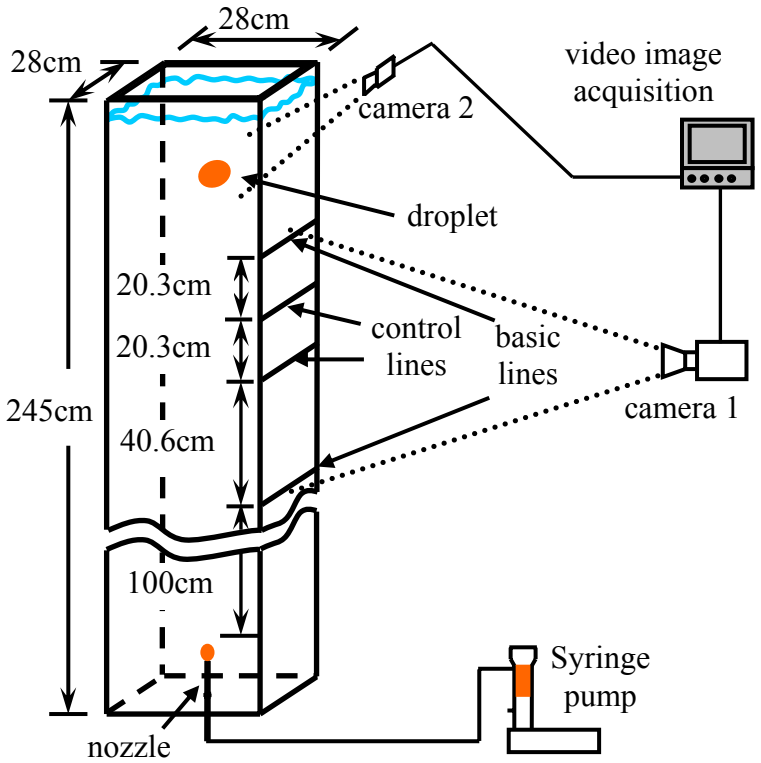

Figure 14. Sketch of the water tank

4.1.1 Particle Release Systems

Two different release systems were tested for liquid/gaseous particles, depending on what material and size of particle is required.

1. Set of replaceable nozzles of different diameters

   The liquid, which forms a particle, is delivered to the nozzle through the tubing by a high precision syringe pump (model 260D, ISCO, Inc., ± 0.005 mL) at a constant rate.

Knowing the pump rate and the time between consecutive particle releases, the volume of the particle can be calculated.

2. Invertible cap

   A high precision syringe pump is used to inject the predefined volumes of liquid particle material under the cap. After making sure the injected material has coalesced into one particle, the cap is inverted and the particle released. This injection mechanism is particularly useful for generating large particles, when the "nozzle mechanism" does not work.

There is a potential problem in using the invertible cap mechanism. In general, a portion of the injected liquid was found to stay in the cap as a coating after the cap was inverted. Following G.S. Beavers and D.D. Joseph [78], to resolve this problem, a thin coat of Scotchgard was applied to the cap internal area. Scotchgard is a trademark of 3M and it effectively repels oil and other liquids from the protected surface. However, it was later found that the drag coefficient in some cases was substantially affected by both the amount of Scotchgard applied and the particle residence time in the cap. It should be taken into account that Scotchgard contains surfactants (e.g., sodium lauryl sulfate). The presence of surfactants, in general, may affect the behavior of the system by changing its interfacial tension. Besides that, pouring the liquid drop (especially of large volume) from the cap introduces a large scale asymmetric perturbation into the system. It may require longer transitional time or even trigger an undesirable instability mode. As the bottom line, the usage of the cap release mechanism repeatedly gave higher magnitudes of drag than direct release from the nozzles, and therefore, was eliminated.

The release mechanism for solid particles is similar to the submarine or spaceship gate system. Two valves are connected by a flexible hose. One of these valves has an outlet to the

environment, another one is attached to the bottom of the tank. A particle is introduced into the hose through the first valve. Then it is released under the invertible cap in the tank through the second valve. Before inverting the cap and starting the measurements, the particle is kept in the cap for several minutes to ensure negligible motion in the medium.

4.1.2 Video Recording and Data Analysis

After the release of a particle, the video recording system is used to find the precise particle location at every instant of time (Camera 1 in **Figure 14**, Sony DXC-325). The time of each recorded frame can be determined using a video timer. This video equipment can provide 30 frames per second, hence, the precision of measurements is approximately 0.033 of a second.

The terminal velocity is found by timing the particle passage between the two basic lines 32" apart as shown in **Figure 14**. An experiment is repeated several times for each particle size to obtain a more representative data set and to estimate data scattering for a given particle size.

Before the actual calculation of the particle terminal velocity using the video data, some preprocessing should be done. Namely, it's necessary to verify that the particle has reached terminal velocity at the lower basic line. To check this, additional control lines were added between the lower and upper basic lines (**Figure 14**). If the velocity change between equidistant control lines does not exceed its experimental scattering, then the particle is assumed to have reached terminal velocity.

It is important to estimate an error in velocity measurements by the method described above. If the precision of measurements is $\Delta t = 0.033\,\text{sec}$, and maximum expected velocity of the particle is $V_{\max} \approx 30\,\text{cm/s}$, then "spatial resolution" of the system is: $\Delta S = V_{\max}\Delta t \approx 1\,\text{cm}$

Thus, precision of the position measurement is roughly $\pm 0.5\,\text{cm}$. If we make the distance between control marks 80cm, we will have reasonable accuracy of $\pm 0.65\%$. Based on these estimations, the overall test section length of 32" seems appropriate.

Having a precise measurement of volume and velocity of the particle along with knowledge of its material properties, we can calculate the drag coefficient of the particle and its Reynolds number (see Eq.(1)).The primary goal of these experiments is to build a set of curves $C_D(\text{Re})$ for chosen pairs of "particle material / liquid medium". Alternatively, representation of the results in the form $U_N = U_N(D_N)$ (see Eq.(16)) will be used whenever it is helpful to describe the experimental results as a function of particle size.

4.1.3 Measurements of particle and medium properties[15]

Particle properties

- Density

Density of a solid particle is calculated as particle mass over the volume. Solid particles are weighted on a precise scale ($\pm 0.0005\,\text{g}$). The volume of large particles (D > 1.2 cm) is calculated based on diameter measurements, using a micrometer (1.2 < D < 2.54 cm) or a caliper (D >2.54cm). For smaller particles, where the precision of the volume measurement must be higher for precise density results, a pycnometer (Accupyc 1330) was used. To obtain the density of the liquid particle material, a large amount of liquid (i.e., 250 mL) is weighed. The density for the bulk is considered as the density of the liquid particle material. Note, that some liquids (i.e., oils) may undergo gradual stratification if left quiescent. Hence, if the oil resides in the syringe pump for few days, the density of the oil

[15] Here we discuss measurement techniques. Values are given in Chapter 5.0.

pumped from the top of syringe pump to form a particle can be slightly lower than density obtained by averaged measurements. Although stratification should not have a significant effect on the results of experiments (our tests have shown density change within 1%), it is rather easy to avoid this problem.

- Interfacial tension

Precise measurement of the particle/medium interfacial tension is quite important, since the Morton number used in the analysis incorporates the third power of the interfacial tension. Ideally, interfacial tension of the particle medium should be measured before every set of experiments. For example, corn or castor oils, if exposed to the open air, undergo oxidation, which is expected to gradually change their interfacial tension. Unfortunately, it was not possible to measure interfacial tension in the NETL facility. Dr. D.D. Joseph from the University of Minnesota kindly provided interfacial tension measurements for several pairs of materials (corn oil, castor oil, isooctane and air in tap water), using the unique spinning drop tensiometer in his laboratory [79].

Medium properties

Density and viscosity of water are quite well tabulated. As for the viscosities of fluid particles, high precision is not critical for the purposes of this research. Therefore, data provided by manufactures (in MSDS or other supporting documents) gives sufficiently good information on the viscosity.

4.1.4 Particle Shape and Rising Regime

Information about the particle shape and rising regime is also of great importance. Although, as was mentioned in Section 2.3, the shape of a particle is not an independent parameter, it is extremely useful for physical insight. It helps to relate the behavior of the drag curve to the shape and regime changes and may help to understand better the dynamics of the motion. Camera 2 (**Figure 14**, Sony XC-ST50) is used to obtain a closer look at the particle motion and, thus, provides a more detailed information on the variation of particle shape. The video record can be used to import particle images to the computer (up to 33 frames per second) and perform digital image analysis. Particularly, a "pseudo-stroboscopic" picture of particle motion can be created. This will provide the chronology of both the path and the shape change of the particle in one still picture. Camera 1 (**Figure 14**) is too distant to show the details of the particle shape, but due to wider field of view, it allows an observation of the particle path over the fluid domain between basic lines.

Note, that Cameras 1 and 2 are located in mutually perpendicular directions with respect to the water tank, in order to permit evaluation of the three dimensional nature of particle motion.

4.2 HIGH PRESSURE WATER TUNNEL (HWT)

4.2.1 Motivation and Development Challenges of the HWT

All the prior studies on CO_2 drops in water at the NETL (Pgh, PA) were performed in the High Pressure Viewcell - an approximately 40 cm^3 pressure vessel [80]. Although the viewcell provides useful data on dissolution rates of CO_2 drops, formation, dissolution, and relative

density of the hydrate shell around the drop, it does not adequately simulate the real oceanic environment:

- It can't be used to model flow past the particle (which takes place when a particle rises in the ocean);
- Particle contact with foreign (glass, stainless steel) materials in the vessel cannot be avoided;
- The small volume of the viewcell causes a gradual increase in CO_2 concentration in water during the experiment (as the particle dissolves).

These drawbacks provide unnatural mass transfer characteristics and create artificial nucleation sites, altering the process of hydrate formation or dissolution.

To overcome these limitations, the High Pressure Water Tunnel (HWT) was designed and constructed at the NETL to simulate the CO_2 particle motion in the deep ocean environment [81, 82]. To help determine the optimal geometries needed in the test section of the HWT, a Low Pressure Water Tunnel (LWT) was used. The low pressure system posed much fewer safety concerns and technical challenges, so it was better suited to analyzing design modifications (see Subsection 4.2.2 for details of the HWT and LWT).

To prevent the particle from rising due to the buoyant force, F_b, an equal force is needed in the opposite direction. This drag force, F_d, can be created by a countercurrent flow in the direction of gravity. The term 'countercurrent' is used because the fluid moves in the direction opposite to the rising particle. The same considerations are valid for a sinking particle, except the directions of all the velocities and forces change to opposite.

A very important consideration for this system is the stability of the particle in both vertical and horizontal directions. Special features of the water tunnels provide mechanisms for such stabilization. A conditioning element above the test section (see **Figure 16**) provides a special

velocity profile for passive horizontal particle stabilization. A representative velocity profile (with a local minimum in the pipe center) is shown in **Figure 15** ([81]).

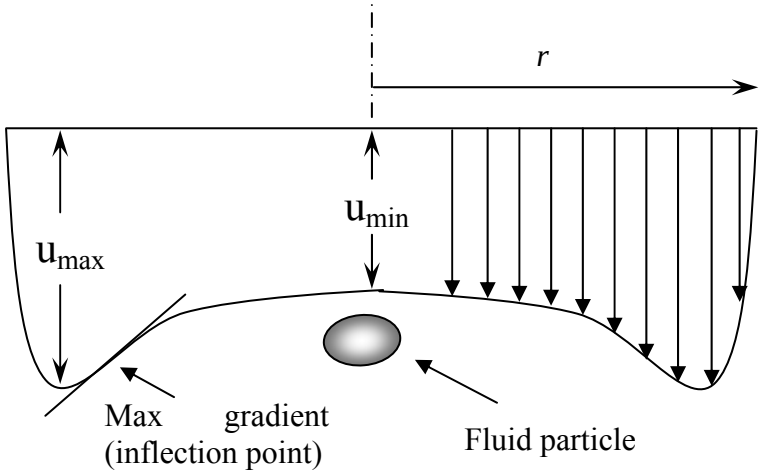

Figure 15. Representative velocity profile in the HWT

In addition, an expansion of the test section downstream works as a passive stabilizing factor in the vertical direction. For example, if the particle deviates downstream from the viewing position, the pipe expansion causes a decrease in drag force and, as a result, force imbalance. A similar but opposite effect would occur if the particle deviates upstream. The resultant force tends to return the particle to the desired position.

Besides passive stabilization by the geometry of the test section, an additional active stabilization in the vertical direction was implemented. A feedback control system with PID controller using particle vertical position as an input signal and the pump speed as an output (single input – single output, or SISO system) was used [82]

More detailed information on the stabilization issues is provided in Section 6.0.

4.2.2 Brief Description of the HWT and LWT

The schematic drawing of the HWT is depicted in **Figure 16**. It consisted of a vertical test section integrated into a closed flow loop with a centrifugal variable-speed pump ($^3/_4$ HP MagnePump from Autoclave Engineers) and control valves for precise water circulation control, a syringe pump to generate and control high pressure in the system, another syringe pump to inject liquid CO_2 or other particle material, and a chiller for cooling the system to deep-ocean temperatures. Measurements of the flow rate in the system were performed by an ultrasonic flow device (Controlotron system 1010N with flow tube 992DFTN) from Controlotron Corporation, of Hauppauge, NY. The HWT could operate at pressures up to 35 MPa and temperatures down to 274K. Pressurized components were located in a securely isolated and structurally reinforced room. Observations and control of all the system components were performed from two control room computers by means of programs developed using LabVIEW version 6 software from National Instruments, of Austin, TX.

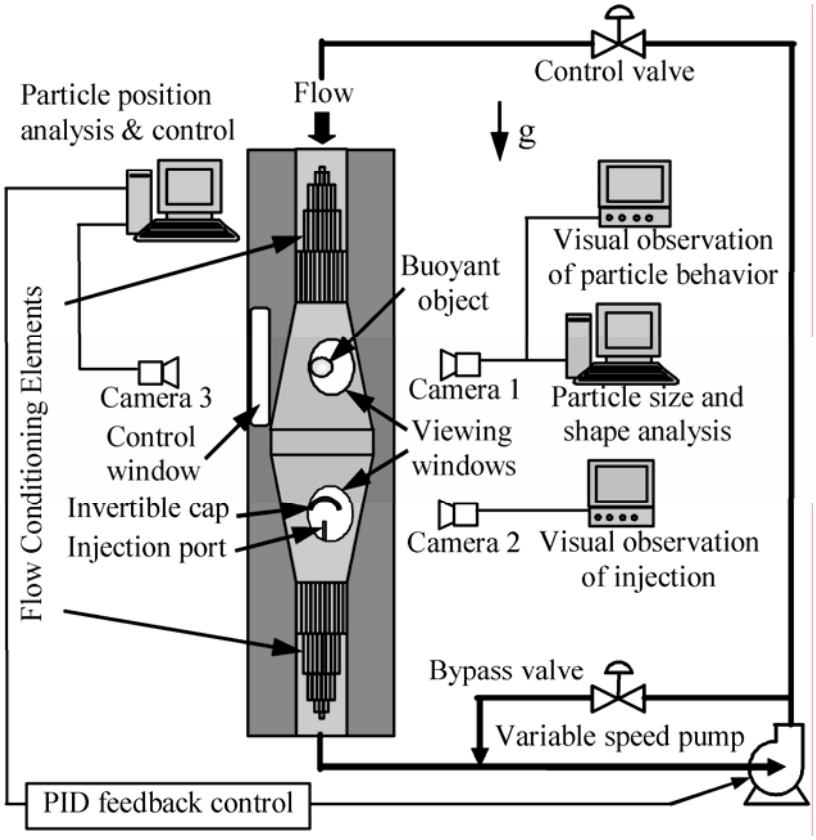

Figure 16. Schematic drawing of the High-pressure Water Tank (HWT)

The two identical conical test sections (38 cm length, 5.1 cm inlet diameter, 7.3 cm outlet diameter) were used for either a rising or sinking fluid particle (**Figure 16**). Several ports on different levels of the test section served for fluid/gas injection into the system and for connecting devices to monitor the temperature and pressure. There were two sets of orthogonal viewing windows that were monitored by charge-coupled device (CCD) cameras. For each pair, the back window was used to provide a diffuse light source and the front window was used for observation. The circular windows (3.8 cm viewing diameter) were monitored with a 640x480 pixel Sony CCD camera which has a sampling rate of 15 Hz and was used for direct observation and recording of the fluid particle behavior. Subsequent automated analysis permitted the sphericity, volume and position of the particle to be tracked through time. To perform this

analysis, a machine vision application was developed at the NETL using IMAQ Vision, the National Instruments add-on library of LabVIEW. Some features of this application included particle identification, edge detection, image analysis and enhancement, least square fit of the particle shape to ellipse, determination of its geometric center and volume. All this operations were performed in real time fashion with a user defined rate. The oblong windows (1.3 cm x 15.2 cm viewing dimensions) were monitored with a 1000x1000 pixel Kodak Megaplus digital camera model ES 1.0 sampled at 9 Hz that permits particle detection and control of its vertical position using a feedback control system. There can be short 'blind' periods, when the particle moves horizontally out of the viewing range of the narrow oblong window and cannot be detected. When this occurred, a simple linear interpolation algorithm was developed to predict the vertical position of the particle and adjust the feedback correspondingly until the particle reappears. Wider oblong windows would have prevented this problem, but they would not have withstood the pressures required to simulate the deep ocean. A representative snapshot of a CO_2 drop in a circular viewing window is depicted in **Figure 17**.

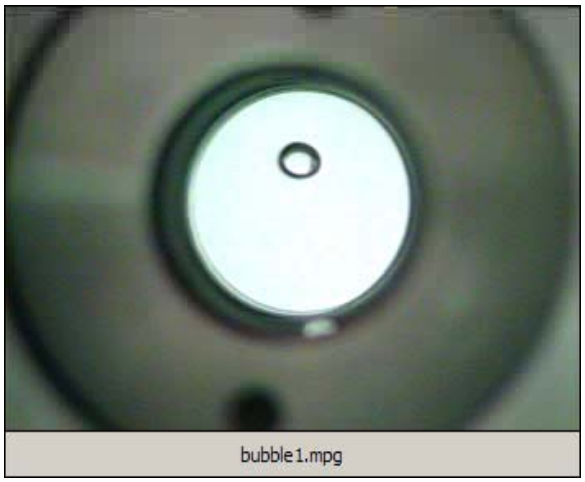

Figure 17. CO_2 drop in a circular viewing window of the HWT

A Low-Pressure Water Tunnel (LWT) was designed and built at the NETL for systematic investigation of possible particle regimes, conditioner and test section designs. The LWT consists of a conical test section which is constructed of transparent plexiglass pipe (inner diameters: x_1 = 5.08 cm; x_2 = 6.35 cm; length 30.5 cm), a loop of PVC plastic pipe, and a

variable-speed centrifugal pump for water circulation. A conditioning element can be easily inserted and removed from the system. An ultrasonic flow sensing system is used to measure the total flow rate in the loop. **Figure 18** shows an air bubble stabilized in the test section of LWT.

Advantages of this facility are:

1. Ease of operation;
2. Considerable flexibility, which is important for frequent design changes;
3. Possibility for obtaining measurements of flow characteristics;
4. Easy visualization due to the transparent test section.

Figure 18. Air bubble stabilized in the test section of the LWT

5.0 FUNDAMENTALS OF FREE PARTICLE MOTION: RESULTS AND DISCUSSION

5.1 EXPERIMENTS WITH FREE FALLING/ RISING SOLID BALLS

Figure 19 shows experimental results for spheres of several density ranges, falling or rising in water:

Table 1. Properties of solid spheres used in the experiments*

	Range of ρ (g/cm^3)	Range of d (mm)
Nylon balls	1.1-1.14	6.35-63.5
High density Polyethylene (HDPE) balls	0.9-0.92	4.75-19
Polypropylene (PP) balls	0.83-0.86	4.75-76.2
Hollow PP balls 1	0.4-0.5	9.5, 19
Hollow PP balls 2	0.31	25.4
Ping-pong balls	0.081-0.089	40

*All the plastic balls were purchased from Precision Plastic Ball Company, of Franklin Park, IL, except the ping-pong balls, which were purchased off the shelf at Dick's Sporting Goods.

Based on the discussion of Section 2.1, we expect that as we consider less dense particles, their drag curves would deviate from the SDC for lower magnitudes of Re. **Figure 19** demonstrates trends in this direction. Loosely speaking, it shows the effect of change in sign of buoyancy while preserving its absolute magnitude. Indeed, HDPE & PP balls (0.83-0.92g/cm^3) and nylon balls (1.1-1.14g/cm^3) in water have about the same magnitude, but opposite signs of buoyancy. Thus, we can see the isolated effect of particle density on the onset of periodic motion. Lighter

particles, PP & HDPE, experience instability and transition from the rectilinear motion at Re = 1,300-1,400, while heavier nylon particles demonstrate this transition only at Re = 3,500.

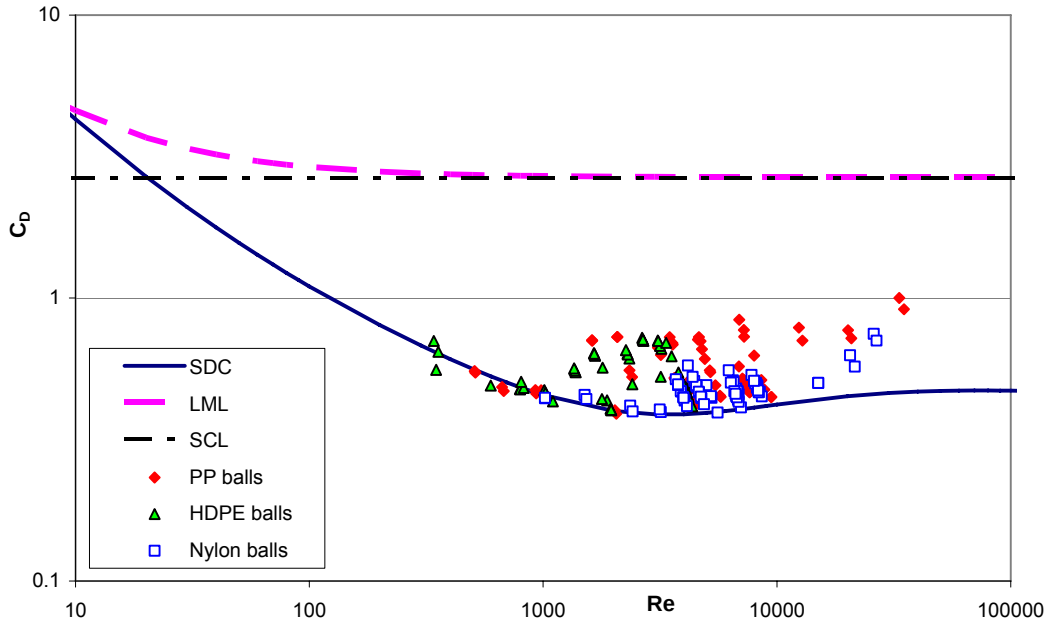

Figure 19. Freely moving solid spheres versus the Standard Drag Curve
(SDC – standard drag curve; LML – large Morton limit; SCL – spherical cap limit; PP – polypropylene; HDPE – high-density polyethylene, see Table 1 for properties)

However, there is strong scattering of the experimental results for seemingly almost identical balls. Earlier work devoted to free motion of solid spheres [52, 53] encountered similar problem, which prevented the development of a generalized relation between the sphere drag and relative density. Several observations were made during our experiments with solid spheres. Data scattering for experiments with the same particle were much smaller than scattering from experiments with different particles of nearly identical size and mass. This led us to the conclusion that there is something different in these spheres, although their diameters and masses are very close. Because of the nature of the manufacturing process (injection molding), the particles used in our experiments inherently have numerous voids. In other words, they are non-uniform – their center of mass, in general, does not coincide with their geometric center.

The next question is how much the small shift in the center of mass can affect the motion of a spherical particle. Some earlier works (for example, a simple model developed in [51] and compared with experiments) suggest that this effect can be rather significant even for a very small shift. To check this hypothesis, the following experiment was performed. A small bore hole was drilled in a 1" polypropylene ball all the way to its center. A small metal wire was then inserted into the hole. The mass of the resulting ball was changed by about 2%, which is the order of mass scattering among the polypropylene balls of this size in the batch. However, this shift of the center of mass resulted in drag increase by about 75% (from 0.45 to 0.8, **Figure 20**)!

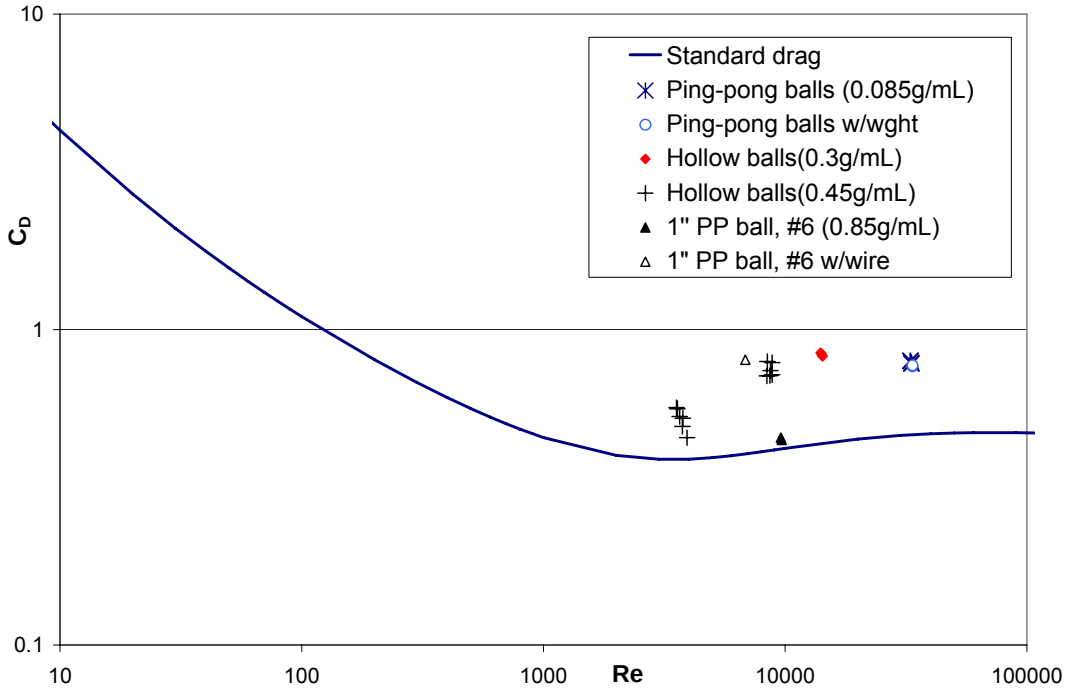

Figure 20. Effect of non-uniform density distribution on the motion of solid spheres

This result implies that if we try to build a drag curve for fixed density ratio, highly uniform spheres should be used for every chosen material, at least for non-rectilinear regimes of motion. The injection molding manufacturing process does not provide the required level of uniformity, therefore, spheres manufactured by a more precise method should be considered. A good

candidate is precision grinding – this procedure is used to manufacture billiard and golf balls of high uniformity and sphericity. Unfortunately, precision grinding is a rather expensive industrial process, and companies offering this service prefer to have a large order (hundreds or thousands of balls). Thus, experiments with highly uniform balls were postponed at this time.

Why would we need to know the drag curves for highly uniform spheres, if most real spherical particles are more or less non-uniform and their drag may significantly deviate from the uniform case? To study the effect of shifted center of mass on particle behavior, a reference case is needed. As was discussed earlier (Section 2.1), the vertical terminal velocity and drag of the freely moving sphere, in general, differs from the standard drag curve. Therefore, the standard drag curve can't serve as a reference case for freely moving spheres. Uniform spheres, on the other hand, provide a good reference case, as particles of given diameter and weight with simplest possible mass distribution. Additionally, such spheres can serve as a reference case for fluid particles of the same volume and mass, where material is usually uniformly distributed; thus, deviation of fluid particles from this reference case is caused solely by the particle shape change.

Another interesting phenomenon was observed during the experiments with ping-pong balls rising in water. Six different balls were tested, and they did not give noticeable difference in drag coefficient. Even more, addition of weight (1.5-5% of the ball's mass) on one side of these balls also did not result in detectable changes in drag (**Figure 20**). These findings indicate that for particles with small inertia (or density) non-uniformity does not play as large a role as for heavier particles. On the other hand, when particles are sufficiently heavy (heavier than the medium) the lateral motion is much weaker, and the effect of the non-uniformity is weaker too. Hence, an

optimum particle/medium density ratio may exist for which the span of drag variations as a function of non-uniformity is maximal.

In fact, the greatest scattering in our data was observed for sphere-to-fluid density ratios between 0.85 and 1.13, while the data for very light spheres in water (SG<0.1) showed little scattering. Viets and Lee [51] developed a theory to explain the oscillatory motion of a sphere based on coupling between its rocking and lift. The rocking in their model was due to a small displacement of the center of mass of a sphere. The authors emphasized the sensitivity of the periodic motion of a sphere even to a minor shift of its center of mass. Significantly, their phenomenological model predicts that this effect is the strongest for sphere-to fluid density ratios between 0.8 and 1.2, which is in line with our findings. Fortunately, fluid particles are typically free of this complication (assuming no stratification). Hence, we would expect much less data scattering, for example, for liquid drops. Indeed, our experiments with drops revealed much less data scattering than analogous experiments for solid spheres (see Section 5.2).

It's quite interesting to find the upper limiting curve of the drag coefficient for oscillatory motion of the particle from both theoretical and applied points of view. Obviously, for a chosen continuous medium, this limit will correspond to the case when the particle has no inertia (spherical void in liquid). In general, it's not expected that this limit will be the same for any continuous medium. As already mentioned in Section 2.1.3, in works [54, 55] the limit for $\rho_p / \rho < 0.3$ in water was found to be about 0.95. Our measurements with selected light balls ($\rho_p = 0.08 - 0.3\,\mathrm{g/mL}$) in water gave slightly lower results: $C_D = 0.76 - 0.85$ (**Figure 20**).

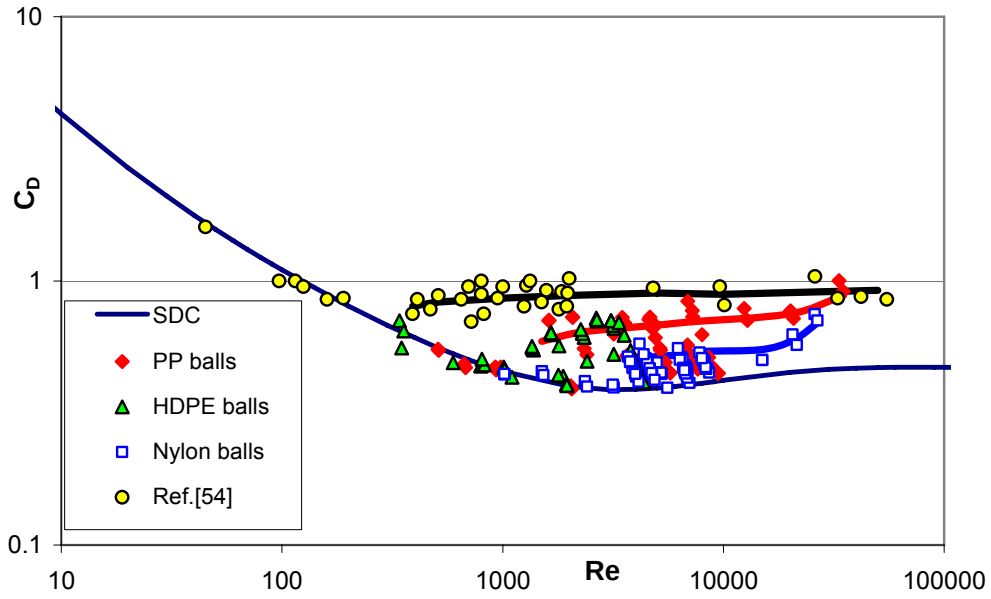

Figure 21. Experimental drag data for light spheres ([54], $\rho_p / \rho < 0.3$), HDPE & PP balls ($0.83 < \rho_p / \rho < 0.92$), and nylon balls ($1.1 < \rho_p / \rho < 1.14$). Solid lines demonstrate trends after transition from rectilinear path: Re ≈ 300; Re ≈ 1,300-1,400; and Re ≈ 3,500; respectively.

Figure 21 shows the results reported in [54, 55] for light spheres ($\rho_p / \rho < 0.3$) along with our results for heavier balls. Although the authors obtained quite interesting experimental results, their interpretation of these results is not always reasonable. For example, they make quite a strong statement about the existence of the universal drag – $C_D \approx 0.95$ – for light spheres ($\rho_p / \rho < 0.3$) at Re > 130. At the same time, they claim that the drag curve for heavier spheres should coincide with the SDC. Existence of two qualitatively different drag laws separated by some threshold particle density seems to be an oversimplified interpretation of the results. As shown in our experiments and some earlier works (e.g., [52, 53]), the drag of freely moving spheres with $\rho_p / \rho > 0.3$ can significantly overshoot the SDC.

The conclusions made by authors in [54, 55] are partially explained by the limited range of Re, at which the experiments were run. For example, experiments for heavier spheres were

mostly reported at Re < 1000-1500. As seen from **Figure 21**, the drag curves for PP & HDPE spheres at these magnitudes of Re indeed coincides with the SDC. Another suspicious statement is that the drag for light particles deviates from the SDC at Re = 130. As discussed earlier (see Section 2.1.1), a bifurcation to the periodic flow around a sphere occurs approximately at Re = 270-300. Hence, there is no mechanism for deviation from the SDC for Re < 270-300! If we look carefully at the results of [54, 55] for light spheres (shown in **Figure 21**), we can see a gap (no data point between Re = 130 and Re = 300). The authors assumed a linear interpolation for Re=0.95 in this gap, although it's much more reasonable to expect a bifurcation in drag at Re > 300. Note also that the data for light spheres indeed demonstrates less scattering than the data for PP & HDPE balls in conformance with our earlier statements.

5.2 FLUID PARTICLES IN WATER

5.2.1 Properties of experimental fluids

One of the ways to ensure interface immobility of a drop (at least in a rectilinear regime of motion) is to conduct a set of experiments with various oils as liquid particle materials. Viscosity of oils is more than an order of magnitude larger, than the viscosity of water. For such a large difference in viscosities, mobility is not an issue (see Section 2.3.3). Therefore, the oil drops are expected to fit the SDC in the spherical regime and gradually deviate from the SDC in the direction of higher drag with increasing non-sphericity (Sections 2.2 & 2.3.3). Using oil drops we can successfully achieve separation of the factors discussed in Section 2.3.4 independent of the level of system purification. Namely, the effect of non-sphericity can be examined

independently and thereby, the unique rectilinear portion of the drag curve can be built for the fixed value of the Morton number and negligible tangential interface mobility.

Once the drag curve for the oils is built, other particle materials (having similar Morton numbers in water) can be tested. Comparison of their drag with the drag of oil drops (at similar *Mo*) can serve as an additional check for the insignificance of tangential interface mobility. If the rectilinear portion of the drag curve for less viscous particles coincides with the one for the oil and does not drop below the SDC, then the tangential interface mobility is suppressed by contamination and can be excluded from consideration.

Below are material properties of the liquids that were used for the experiments in water.

Table 2. Material properties of fluids used in the experiments*

	Viscosity μ_p, g/cm/s	Density ρ_p, g/cm^3	Interf. tension γ, g/s^2	μ_p/μ	ρ_p/ρ	*Mo*
Corn Oil	0.45	0.917	20.1**	45.9	0.919	9E-11
Castor Oil	9	0.957	16.8**	918	0.958	7E-11
Isooctane	0.0047	0.69	35.5**	0.48	0.691	6E-11
Ethyl Phthalate	0.12	1.118	14.4	12.3	1.120	3.9E-10
Bromobenzene	0.011	1.49	38	1.12	1.493	8.8E-11
Air	1.80E-5	1.2E-3	59.3**	1.86E-3	1.2E-3	4.2E-11

* Mazola brand corn oil – off the shelf at Giant Eagle;
Castor oil – from Aldrich Chemical Co., of Milwaukee, WI;
Isooctane – from Mallinckrodt, Inc., of Paris, KY;
99%+ Ethyl Phthalate – from Alfa Aesar, of Pelham, NH;
99% Bromobenzene – from Alfa Aesar, of Ward Hill, MA;

** Interfacial tension measurements for these materials in tap water were kindly provided by Dr. D.Joseph's group (Aerospace Eng. and Mechanics, Univ. of Minnesota).

Water density and viscosity for the experimental temperature range of 20-24°C were taken from [83]. Material properties for air bubbles in non-purified water are also provided, since we desire a generalized approach for any fluid particle (see Subsection 2.3.4).

As follows from **Table 2**, all the fluid particles except ethyl phthalate have Morton number in a rather narrow range, $Mo = (4\text{-}9)\cdot 10^{-11}$. Compared to the full span of physically achievable Morton numbers (more than 10 orders of magnitude), this dispersion is small; therefore, *Mo* is assumed to be approximately the same for these materials. The value for the interfacial tension of ethyl phthalate in tap water was taken from [69], and the reliability of this value should be checked. For example, if we use 22-23 g/s^2 instead of 14.4 g/s^2 for interfacial tension, then *Mo* for ethyl phthalate nicely falls into the above mentioned range.

5.2.2 Representation of the experimental data and "three-parametric" models

After the choice of materials for the experiments, we need to choose an optimal way to represent the experimental results (without loss of generality and taking into account all important phenomena). As discussed earlier, one of the important objectives of the present experimental study with fluid particles is to show the insufficiency of the "three-parametric" approach for the complete description of particle behavior even for the case of tangentially immobile interface.

If we overlook the imperfections of correlations (B2) (see Appendix B), the ideal 3-parametric model sought by the authors could be schematically represented by **Figure 22**.

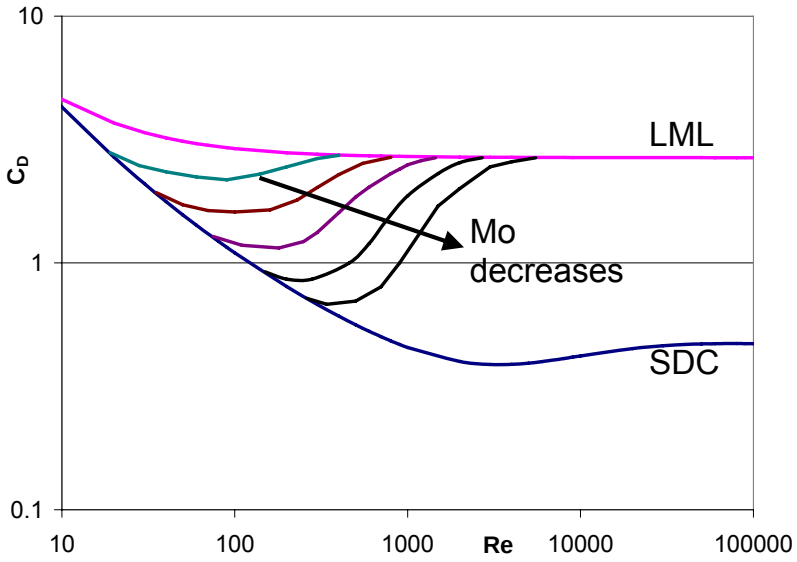

Figure 22. Idealized representation of the "three parametric" model in terms of drag curves for tangentially immobile interface (SDC – standard drag curve, LML – large Morton limit). Helps to visualize the concept of *Mo* as a measure of particle deformability

Loosely speaking, this is just **Figure 10** expressed in terms of drag curves. As mentioned in Section 2.3.4, formal transformation from **Figure 10** to **Figure 22** can be done using relation (41) between non-dimensional parameters. Although formally both representations are equivalent, we'll try to provide here some arguments in favor of using the format of drag curves (or format of non-dimensional velocity, U_N, versus non-dimensional diameter, D_N, see Eq.(16) for definition):

1. The using of drag curves gives us an opportunity to extend and generalize the case of solid spheres to the fluid particles (impossible in Re(*Eo*) format, because dimensionless parameter *Eo* is irrelevant for a solid particle);
2. Material parameter γ (which is a part of dimensionless number *Eo*) is the largest source of error. In addition, it can even vary during the experiment. Therefore, it's difficult to build precise curves for Re(*Eo*). On the other hand, C_D(Re) or $U_N(D_N)$ don't involve γ. Interfacial tension is present only in the material parameter *Mo*.

Thus, in the remaining portion of this paper, our experimental results for fluid particles will be represented in the form C_D(Re) or $U_N(D_N)$.

The appeal of representing the data in the form shown in **Figure 22** is related to the concept of the *Mo*, as a measure of particle deformability (see discussion on Morton number in Section 2.3.5). As Re (inertia) grows, the drag curves deviate from SDC (zero deformability limit) and approach the LML (highest deformability limit). Obviously, "more deformable particles" (having higher *Mo*) deviate from the SDC and merge to the LML curve at lower values of Re. Thus, we would expect to generate a set of parametric curves between SDC and LML. Unfortunately, this scenario can't be realized due to the loss of stability of particle rectilinear motion. The emerging instability denies the completeness of drag curves for fixed *Mo* and requires consideration of at least one more dimensionless parameter. As for **Figure 22**, it basically replaces the variety of drag curves with bifurcations by some averaged curve (for every fixed *Mo*), which smoothly connects SDC and LML. Therefore, although giving some physical sense to fluid particle behavior, this type of figure lacks the details of behavior in the most interesting transitional region.

5.2.3 Rising Fluid Particles

Experimental information was initially collected in the form of particle terminal velocities as a function of particle equivalent diameter. This format is more intuitively clear, because it gives an idea of how the particle behavior changes as its volume increases. Therefore, initially, we provide our experimental data in the form $U_N(D_N)$. **Figure 23** depicts the results for the rising (positively buoyant) particles, with material properties given in **Table 2**. Every data point is an

average of several (usually from 8 to 12) experiments repeated for every particle size and the error bars correspond to the dispersion of these repeated experiments.

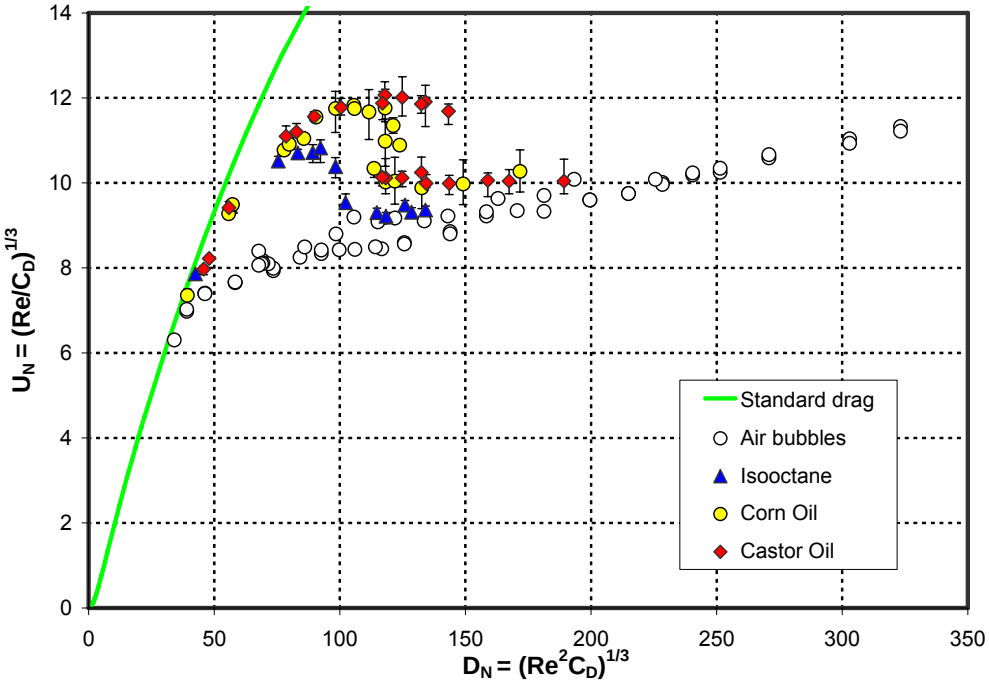

Figure 23. Experimental results for non-dimensional velocity U_N as a function of non-dimensional diameter D_N for rising drops and bubbles

We'll leave the discussion of the peculiarities of the curves for various experimental fluids until the more traditional representation (in the form of drag curves). Here, we just note that freely moving liquid drops with sufficient quantities of surfactants and approximately the same Morton number fit the same curve in a regime of steady (rectilinear) motion ($D_N < 75$), as predicted by the non-dimensional analysis.

Figure 24 provides a more traditional representation of the same results – in the form of drag curves. The averaged experimental values are shown without error bars to avoid overcrowding the figure.

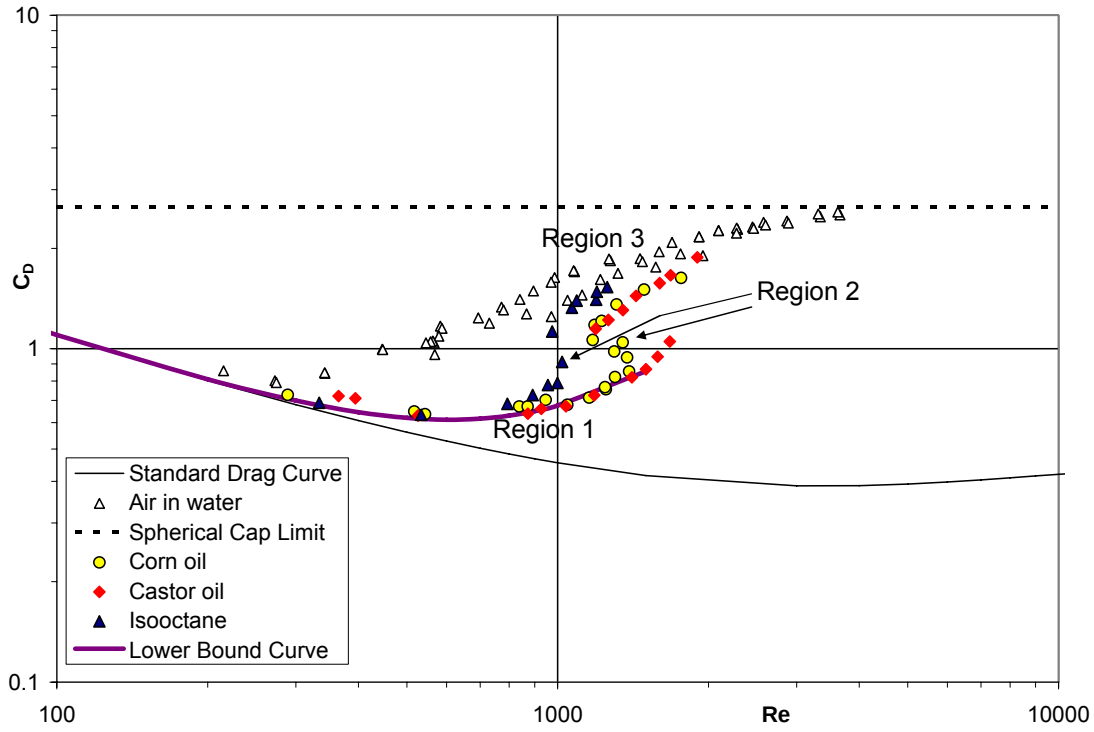

Figure 24. Drag curves for rising liquid drops and air bubbles in non-purified water

All the curves can be characterized by three distinct regions:

Region 1. The drag curve deviates from the SDC. The gradual character of this deviation along with visual observations of gradually increasing non-sphericity, confirm that non-sphericity increases drag compared to the corresponding spherical particle. Note that in this region the drag curves for all the tested liquid drops fit each other rather closely. According to the earlier discussion, this means the interface mobility, as a competing factor for reducing drag, is negligible (either due to high viscosity ratio, as for oils – see 2.3.3, and/ or due to the contamination, as for the other particles – see 2.3.2). Thus, the non-sphericity is the only factor responsible for deviation from the SDC in this region, and the Morton number uniquely defines the portion of the curve corresponding to the rectilinear motion.

Region 2. The drag curve experiences a rather sharp growth in a narrow range of Re (in some cases even a reversed trend in Re is observed). An observation of drop trajectories in the water column reveals this is the region of changes in rising regime. The particle path is not rectilinear any more, but demonstrates a transition to the periodic pattern(s) governed by certain unstable perturbation mode(s). The detailed analysis of this transition will be performed in the later section(s).

Region 3. With further increase in particle size, the particle enters the third region of the drag curve. In this region the slope of the C_D(Re) curve gradually diminishes and the curve appears to approach the SCL. Unfortunately, experiments with larger liquid particles are problematic or impossible. Above a critical size, we could not form drops using the nozzle system. Even if formed using some other mechanism (e.g., rotating cap), they were structurally unstable and tended to break up after release. Therefore, it is still not clear, if liquid particles in the limit of large Re admit the spherical cap shape. Thus far, there are no indications of this shape at the highest achievable Re.

We now turn to the discussion of peculiarities in the drag curve behavior for each type of particle material. From **Table 2**, the Morton numbers and density ratios for both oils are similar and their viscosity ratios are both higher than 20. Hence, following the arguments of Subsections 2.3.1 and 2.3.3 we don't expect much difference in the drag curve behavior for both oils. Indeed, both curves coincide in the majority of the experimental range of Re and demonstrate transition to the periodic regime at similar values of Re. An important feature of these curves is the presence of a region of dual solutions. Namely, two particles of the same size can have qualitatively different motion (rectilinear or periodic). A possible explanation for this phenomenon is conditional stability. That is, the rectilinear motion is still stable with respect to infinitely small

perturbations, but it becomes unstable with respect to finite perturbations of certain critical amplitude. This range of conditional stability is wider for castor oil.

The density ratio and viscosity ratio for isooctane in water are appreciably lower than for the oils. Following our arguments from Section 2.3.4, since isooctane has a lower inertia than oil drops of the same size, we expect an earlier transition to periodic motion. Indeed, the maximum extent of rectilinear motion for isooctane drops is about Re ≈ 1,000 (versus 1,400 for oils).

The experimental data for the air bubbles requires special discussion. At a first glance, it is significantly off the general trend for liquid drops, suggesting the need to consider it as a special case. However, having almost zero density, the air bubbles would be expected to experience a bifurcation from the rectilinear path at a much lower magnitudes of Re than the liquid drops. In this regard, the behavior of air bubbles suggests a reasonable physical explanation. The bifurcation to the non-rectilinear regime for air bubbles occurs at approximately Re = 300-400. As was mentioned in Section 2.1.1, this is the magnitude of Re, where the flow around a spherical particle becomes periodic. Since the bubbles are virtually weightless particles ($\rho_p / \rho \to 0$), they readily respond to the periodic fluctuations of the flow. By coincidence, the appreciable non-sphericity for the fluid particles also starts at Re ≈ 300-400. Therefore, for air bubbles, we are not able to observe the deviation from sphericity (from SDC) and the bifurcation from the rectilinear regime of motion as the two distinct transitions. To the best of our knowledge, it is theoretically possible for the onset of non-rectilinear motion to occur at a lower Re than deviation from sphericity. In this case, the behavior would be analogous to the free motion of solid sphere.

Hence, the curve for air bubbles also supports the need for using density ratio as an additional parameter. Furthermore, the results in **Figure 24** suggest the drag curves for various

fluids with $Mo \approx 6.5 \cdot 10^{-11}$ merge to the drag curve for air bubbles in the non-rectilinear regime of motion for sufficiently high Re. So, the drag for air bubbles can possibly serve as a limiting curve (or upper bound curve, UBC) for particles in water with fixed Morton number ($Mo \approx 6.5 \cdot 10^{-11}$ for our experiments). However, experiments at higher Re to confirm this conjecture were not possible owing to limitations in particle size using our nozzle release system.

The Lower Bound Curve (LBC) is also shown in **Figure 24**. As expected, it serves as a lower bound for data from all fluid particles (including air bubbles) with $Mo \approx 6.5 \cdot 10^{-11}$ in the rectilinear regime (before bifurcation), which is consistent with the conjecture based on non-dimensional analysis (e.g., Section 2.3.4).

It is also apparent that this experimental data for fluid particles has less scattering than the data for solid particles (**Figure 19** vs. **Figure 24**). This fact supports our hypothesis (see Section 5.1) about the effect of non-uniformity on particle drag.

5.2.4 Bifurcation in the Drag Curve

Region 2 of the drag curves discussed in the previous subsection deserves closer attention as a narrow range of Re, where abrupt quantitative and qualitative changes are observed. To extract more physical insight from this region, consider separately the drag data for castor oil (**Figure 25**). This set of data displays the most pronounced peculiarity.

For a certain range of castor oil drop sizes (1.25 mL - 2 mL) we observed two different rising regimes - rectilinear and zig-zag. This was the case for different drops in this range of sizes and even sometimes for the same drop - it moved in a slight zig-zag path in the first half of test section but moved rectilinearly in the second half.

The castor oil drag curve clearly consists of two branches (**Figure 25**), and these two branches overlap for drops with volumes in the range 1.25 mL - 2 mL. The following hypothesis is suggested to explain this phenomenon.

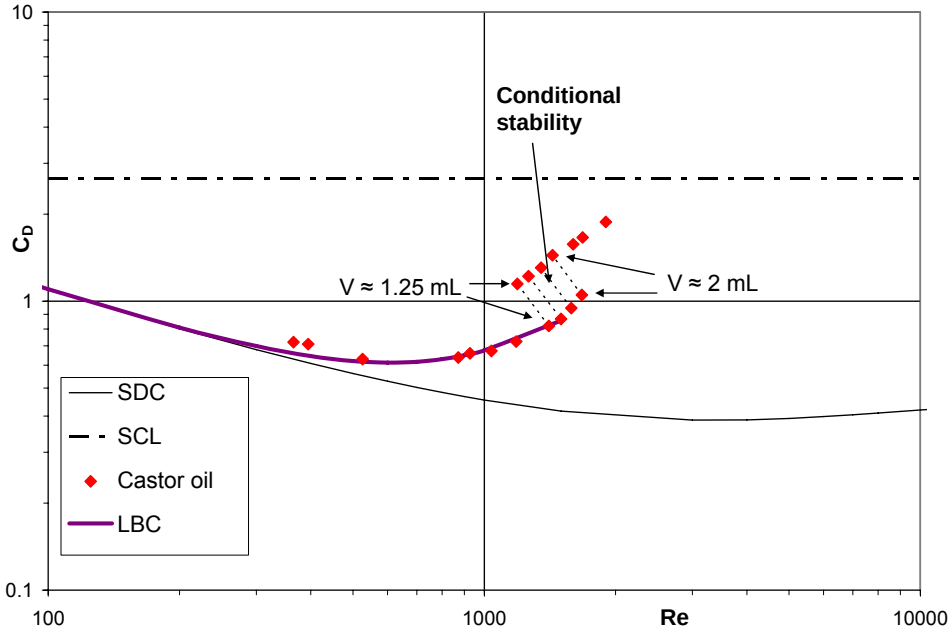

Figure 25. Experimental and numerical data points for drops of castor oil (SDC – standard drag curve; SCL – spherical cap limit; LBC – lower bound curve)

Rectilinear motion is unconditionally stable for $V < V_{crit}$ (< 1.25 mL). However, as the particle exceeds this size, the particle may face conditional stability. That is, rectilinear motion is still stable with respect to infinitely small perturbations, but it becomes unstable with respect to finite perturbations of certain critical amplitude. Such a critical perturbation may be introduced during release from the nozzle. The amplitude of perturbations depends on the conditions at the instant of the release (especially for large diameter nozzles), and medium conditions in the vicinity of the release. Even if rectilinear motion is stable with respect to the amplitude of the release perturbations, the zig-zag motion may converge to rectilinear motion very slowly. So, at the beginning of the test section some rocking still can be observed. For castor oil particles larger

than 2 mL, we have unconditional instability, and thus, we can observe only non-rectilinear motion.

The basic idea of the hypothesis is that the drag curve (averaged over the period for periodic regime) is not continuous – a bifurcation point exists (slightly below 1.25 mL for castor drops). The magnitude of Re, at which the lower curve becomes unstable, depends on initial conditions and amplitude and type of perturbations in the system. A new frequency of particle oscillations is introduced into the system at this point, so this point can be considered as a Hopf bifurcation.

As was mentioned earlier (see Section 2.1.1), a Hopf bifurcation of the flow around the fixed solid sphere occurs for Re slightly below 300. The fact that free motion of oil drops appears to be rectilinear for 300<Re<1400 is probably a tribute to the particle inertia. That is, the energy of periodic fluctuations for Re<1400 is not sufficient to appreciably move the drop in the lateral direction. It is important that the transition to periodic motion occurs rather abruptly, in a "bifurcation-like" manner. Periodic particle oscillations don't increase gradually from zero (as one may think) with the gradual growth of energy of periodic flow fluctuations.

For further development of this hypothesis, return to **Figure 9** for nearly spherical air bubbles. The axisymmetric numerical solution for spherical air bubbles in purified water (line for $\lambda = 0$ in **Figure 9**) extends beyond Re=400. At the same time, experimental results show a very sharp deviation from this curve for Re>400. It is hard to believe that just a change of the bubble shape causes such an abrupt deviation. It seems more reasonable to consider this value of Re as a bifurcation point. This point of view seems to find confirmation in experimental works [24, 84]. Although the visualization technique in 1950s was not as advanced as it is today, visual inspection of recorded frames from [24] suggests that lateral motion of air bubbles in water starts at least from Re=465. This is approximately the minimum of the drag curve for air bubbles in

purified water. Lindt [84], based on Rosenberg's observations [63], summarized the shapes and regimes of bubble motion in purified water for different Re numbers. He reported that periodic motion of the bubble starts approximately at Re=500.

Next, recall that we deal with air, whose density is negligible compared to the density of water (no inertia). Hence, we assume the onset of periodic motion of air bubbles coincides with the onset of periodic motion of the flow around the bubble. Recent numerical results of several authors confirm that flow around a solid sphere becomes periodic at Re slightly below 300 [41-43]. To the best of our knowledge, there are no similar works published for spherical fluid particles. However, spherical bubbles in purified water have a mobile interface, which can possibly shift the onset of periodic flow up to $\mathrm{Re} \approx 400\text{-}500$ (less drag, smoother flow).

Concluding this subsection, we may try to apply the concept of chain of bifurcations (as the way of transition to chaos) to the motion of fluid particles. Earlier in this thesis (Subsection 2.1.1) we already discussed the scenario of the transition to chaos through consecutive Hopf bifurcations with incommensurable wave numbers. Up to this point, we were able to observe only the first Hopf bifurcation from the rectilinear regime of motion and the appearance of the first Hopf frequency. On the other hand, the behavior of a spherical cap particle suggests that we deal with the chaotic regime, where the motion is on average rectilinear and the spectrum of fluctuations has no clearly pronounced dominant frequencies. If we admit the truncated scenario of the transition to chaos [46], we miss two successive bifurcations on the way to the spherical cap regime. In the future, it may be beneficial to study in more detail this range of fluid particle behavior in an attempt to reveal these missing bifurcations.

5.2.5 Sinking Fluid Particles and Shape Oscillations

Based on the experimental results for buoyant fluid particles (including air bubbles) we initially suggested the following hypothesis for particle behavior at fixed *Mo* in non-purified medium:
The SDC for fixed solid spheres can be considered as a curve corresponding to zero deformability. At low Re, corresponding to low energy of flow, the drag of fluid particles will follow the SDC. As Re increases, the growing energy of the flow deforms the particles and increases the drag above that predicted by the SDC. This curve, the LBC, is unique for a fixed magnitude of *Mo* as long as the motion of a fluid particle stays rectilinear. As the Re increases further, a bifurcation occurs from the rectilinear motion curve to another branch of the drag curve, that represents the periodic regime of motion for a given density ratio. Uniqueness of the behavior for fixed *Mo* does not hold any more; the bifurcation from the LBC occurs at higher Re for more inertial particles. The particle retardation due to this bifurcation can be so pronounced that it can cause a reverse trend in Re (e.g., **Figure 24**).

This hypothesis was supported by data for the rising fluid particles used in our experiments, including air bubbles. Indeed, the transition to the periodic motion occurs at Re around 300-400 for air bubbles, about 1,000 for isooctane, and approximately 1,400 for oils.

Additional experiments with heavy (sinking) fluid particles were initially planned in order to confirm the same trend. That is, heavy particles were expected to fit the same rectilinear regime as rising particles (providing they have the same *Mo*) and to give an extension of the LBC towards higher Reynolds numbers (later bifurcation). This scenario would nicely fit our hypothesis regarding the delay in bifurcation until higher magnitudes of Re for more inertial particles. However, the results obtained for the sinking particles were somewhat unexpected. **Figure 26** summarizes the experimental results for all the materials, provided in **Table 2**. Indeed,

the drag curves for ethyl phthalate and bromobenzene rather nicely fit the LBC in the rectilinear regime of motion, but the bifurcation from rectilinear motion occurs not as predicted by the "inertia hypothesis" (see previous paragraph). In fact, sinking droplets demonstrate transition from the rectilinear regime at even smaller magnitudes of Re than rather light isooctane.

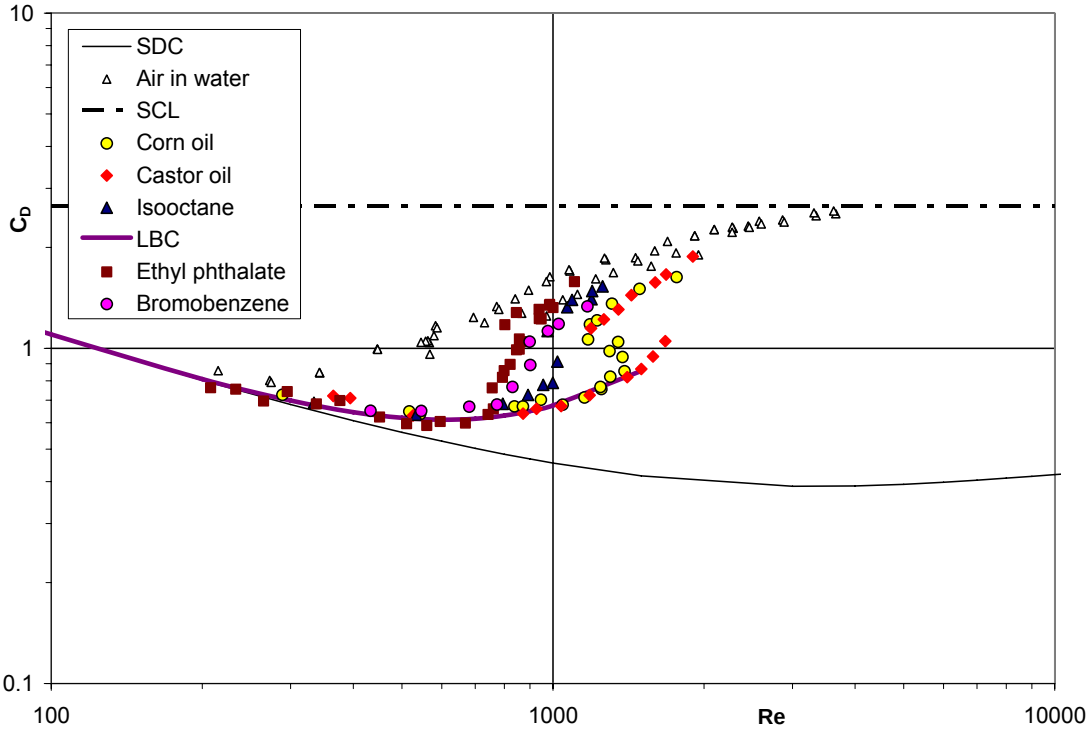

Figure 26. Drag curves for liquid drops and air bubbles in non-purified water (SDC – standard drag curve; SCL – spherical cap limit; LBC – lower bound curve)

Since the initial hypothesis fails to explain the behavior of sinking particles, we may suspect the existence of another mechanism, which triggers the instability in particle motion. Observations of the drops in periodic regimes in the Water Tank reveal some peculiar differences in their behavior. In particular, oil drops experience a rather strong rocking motion and no detectable shape oscillations. On the other hand, the drops of bromobenzene and ethyl phthalate (and, to some degree, isooctane) demonstrate shape oscillations along with rocking motion. Oscillations of shape (especially pronounced at the rear of the particle) typically have several times higher

frequency than rocking. For sinking particles, often "intermittency" is observed in the transitional regime: shape oscillations are transformed into the rocking; rocking damps out, leading to shape oscillations again; etc. On the border between rectilinear and transitional regimes the following phenomenon was observed for bromobenzene drops: after release, the drop experiences shape oscillations (due to perturbation at the release), which eventually die out; no rocking was noticed.

The above observations imply that "shape instability" for sinking drops occurs at lower Re than path instability. Thus, we may deal with an additional mechanism, which triggers instability in the system. What is the origin of this mechanism? In our previous considerations (see Subsections 2.3.2 and 2.3.3) we neglected one of the material parameters – particle viscosity. However, the particle viscosity (damping factor) could be important for the particle shape oscillations.

Qualitative analysis of the behavior of such a system in the vicinity of the critical (transitional) state can be performed using a simple spring-mass-damper one-dimensional analogy (see e.g. [85]):

$$m\,\ddot{x}(t) + c\,\dot{x}(t) + \gamma\,x(t) = f(t)\,, \tag{52}$$

where m represents inertia, c is the viscous friction, γ is the interfacial tension or restoring force, and $f(t)$ represents an input forcing function for the system.

It is well known from the linear control theory that a simple mass-spring-damper system (52) allows oscillations if the damping factor is less than unity:

$$\ddot{x}(t) + \frac{c}{m}\dot{x}(t) + \frac{\gamma}{m}x(t) = \ddot{x}(t) + 2\varsigma\,\omega_n\dot{x}(t) + \omega_n^2\,x(t) = \frac{f(t)}{m}; \qquad \varsigma = \frac{c}{2\sqrt{\gamma m}} < 1; \tag{53}$$

where ς is damping factor, ω_n is natural frequency of the system.

From this simple qualitative analysis we can make the following important conclusion: higher inertia particles with higher interfacial tension are better candidates for the existence of shape oscillations, while high viscosity tends to suppress these oscillations.

It should be emphasized that these simple one-dimensional considerations are not appropriate for a quantitative analysis of the actual particle three-dimensional behavior. Other parameters (for example, particle size and shape) should be taken into account for such analysis. In addition, even the basic parameters of the mass-spring-damper system (52) (m, c, γ) are not clearly defined. Nevertheless, the above considerations enable us to formulate a reasonable explanation for the fluid particle behavior and can serve as a motivation for further investigations.

There is a very important fundamental difference between the two types of instabilities described above. The path instability has no restoring force. Hence, we would expect the "rocking" frequency to coincide with the frequency of vortex shedding in the flow around the particle. On the other hand, the shape oscillations possess their own natural frequency, $\omega_n = (\gamma / m)^{1/2}$, since the interfacial tension provides a restoring force. For the sinking particles in our experiments this frequency is several times higher than the shedding frequency, so we can approximately treat every shed vortex as forcing impulse, $f(t)$, and look for the impulse response of Eqn.(52).

5.3 COMPARATIVE ANALYSIS OF FLUID AND SOLID PARTICLES

Recall that one of the main goals of this work is to maximally generalize the description of free motion of a particle in a quiescent medium. In this light, it is useful to bring together the experimental results we have so far for bubbles, drops, and solid spheres for comparative

analysis. **Figure 27** demonstrates such a graph obtained by combining **Figure 21** and **Figure 26** for solid and fluid particles in non-purified water. Drag curves for bromobenzene, ethyl phthalate, and isooctane drops are not included to avoid overcrowding. Since solid spheres demonstrate quite large scattering of data (see Section 5.1 for details), solid lines are sketched for them in order to help to visualize the trends.

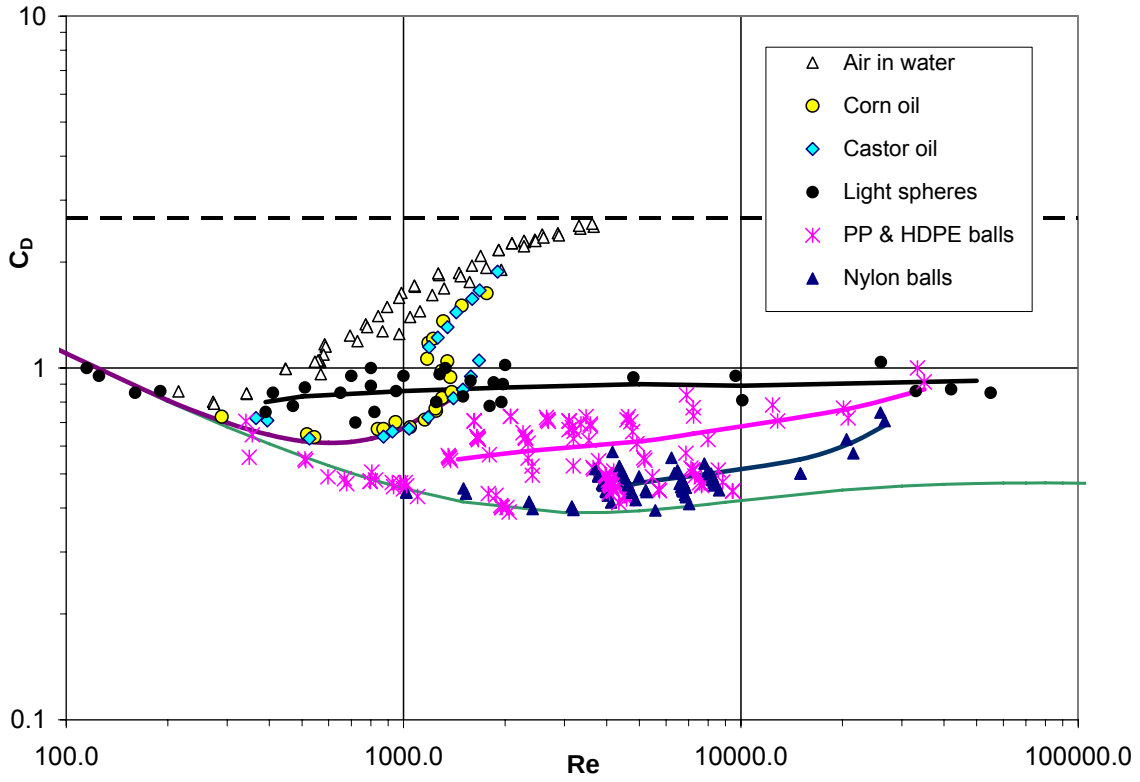

Figure 27. Comparison of drag curves for solid, liquid, and gaseous particles. Solid lines demonstrate trends in drag of solid spheres after the bifurcation from the rectilinear path (PP – polypropylene; HDPE – high-density polyethylene; see Table 1 for material properties)

The most important observation which can be made from **Figure 27** regards the onset of a bifurcation for essentially different fluid and solid particles. In **Figure 27** we can group liquid and solid particles into pairs with respect to their inertia (through the density ratio): light solid spheres ($\rho_p < 0.3\,\mathrm{g/cm^3}$) and air bubbles will make the first pair; PP & HDPE balls (0.83-0.92

g/cm^3) are good candidates to be paired with oils (0.91-0.96 g/cm^3). In every of these pairs, as Re grows, a loss of sphericity causes significant deviation of the fluid particle drag from its solid counterpart. However, one important event occurs approximately at the same Re for "inertially similar particles." Indeed, detailed inspection of the data for oils and PP & HDPE balls shows the instability of the rectilinear motion and transition to the periodic regime occurs at similar magnitudes of Re (between 1,300 and 1,400). Comparison of another pair, light solid spheres and air bubbles, reveals the same trend. As discussed earlier (Section 5.2.3), the bifurcation from the rectilinear regime for air bubbles occurs with no significant non-sphericity observed. Therefore, both drags are rather close even at the transition to periodic regime. Significant deviation of two curves caused by non-sphericity occurs after the bifurcation. Since both are much lighter than water, the bifurcation occurs shortly after the onset of instability in the flow around the particle, that is, after Re = 300. Since both particles have a (nearly) spherical shape at the bifurcation, the bifurcation occurs directly from the SDC (see **Figure 27**).

Unfortunately, this appealing correspondence between solid and fluid particles of similar inertia does not extend to all particle materials. As we already discussed in Section 5.1, the onset of the bifurcation for more inertial spheres occurs at higher magnitudes of Re. From **Figure 27**, this bifurcation is at Re = 300 for light spheres, at Re = 1300-1400 for PP & HDPE balls, and at Re = 3,500 for nylon balls. Hence, following the logic of previous paragraphs, one would expect that ethyl phthalate drops, being "inertially similar" to nylon balls (close densities), should have similar bifurcation point (Re = 3,500). However, another type of instability – shape oscillations – is possible for fluid particles with certain combination of particle parameters (particle inertia, viscosity, interfacial tension – see Section 5.2.5). This phenomenon is more significant than the "inertial similarity" and causes an earlier transition to the non-rectilinear path for fluid particles.

We now reconsider why air bubbles and oil drops were chosen for comparison with solid spheres. Both lack significant shape oscillations (at least in the vicinity of the bifurcation from the rectilinear regime) and, hence, the "inertial similarity" is sufficient for them to behave similarly Absence of oscillations for these particles can be reasonably explained using qualitative analysis of Section 5.2.5. Indeed, according to Eq.(53), no shape oscillations are expected, if:

$$c > 2\sqrt{\gamma m}\,, \tag{54}$$

where c, m, and γ are viscous, inertial and surface tension terms, respectively.

In the case of oil drops, particle viscosity is very high, so the inequality (54) is satisfied. For air bubbles, the viscosity is rather low, but the air density is three orders of magnitude less than the density of water. Therefore, the expression on the right hand side of Eq.(54) is also rather small, so the inequality (54) will likely still be satisfied.

6.0 PARTICLE STABILIZATION IN LWT & HWT: RESULTS AND DISCUSSION

As described in Section 3.2, an important objective for the CO_2 sequestration research was to find an optimal configuration for maintaining fluid particles of various sizes within the observation window for up to several hours. At the same time, we should reduce as much as possible any deviation from the natural particle dynamics, typical for free particle motion in a water column.

As briefly discussed in Section 4.2, special features were implemented in the LWT and later in the HWT to achieve these goals:

- flow conditioning elements – for lateral stabilization and
- tapered test section & PID (proportional-integral-derivative) controller – for vertical stabilization.

In this chapter, we will elaborate on particle stabilization and discuss more generally particle behavior in specific gradient flows created in the test sections of LWT and HWT.

6.1 PRELIMINARY CONSIDERATIONS

Flow conditioning elements were used to provide a desired velocity profile for lateral stabilization of a fluid particle in the test section. They were composed of a bundle of small (from 3.5 to 5.5 mm OD) straws of different lengths with hexagonal ("honeycomb-like")

arrangement located in the straight pipe upstream from the test section. The central part of the conditioner had longer straws, causing a local velocity minimum in the center of the pipe (**Figure 28**) for a finite region downstream of the conditioning element. The usage of such "honeycomb-like" structures as the flow conditioning elements gives a great deal of flexibility. Indeed, a much greater variety of flow profiles can be obtained in the test section using "honeycomb"-conditioners, compared to the other methods (for example, a cylindrical rod on the axis of a pipe [86]).

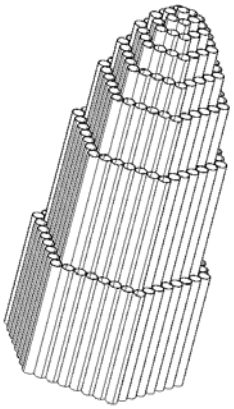

Although conditioners of similar kind were used to reduce velocity on the axis of the pipe in earlier studies [87], to the best of our knowledge no systematic investigation on optimal geometry of the system was previously performed.

Figure 28. Sketch of representative conditioning element

An important issue to be considered in the design of the test section is the optimal distance from the conditioner to the object of observation. If the particle is located too close to the conditioning element, the jets from individual straws will essentially alter the hydrodynamics and mass transfer around the particle and may even break it up. If the conditioning elements are too far from the particle, the velocity profile will be altered too much by viscous effects to be useful for particle stabilization.

Figure 29 displays velocity profiles in the test section of the LWT, experimentally obtained using an automated traversing Pitot tube system[16]. Local maxima from individual jets are clearly seen 8 cm downstream from the flow conditioner at a flow rate of 12 L/min. As the profile

[16] For more detail on Pitot tube design and usage in both LWT and HWT, see Appendix C.

develops downstream, the maxima from the individual jets diminish and by 17 cm from the conditioner, the profile is smooth. Note that this flow rate (12 L/min) is close to the critical value of transition to the turbulent flow for this particular geometry of the test unit (see also Section 6.3 on this matter). Hence, it provides the largest development length; that is, for other flow rates the effect of the individual jets from the straws will be less pronounced.

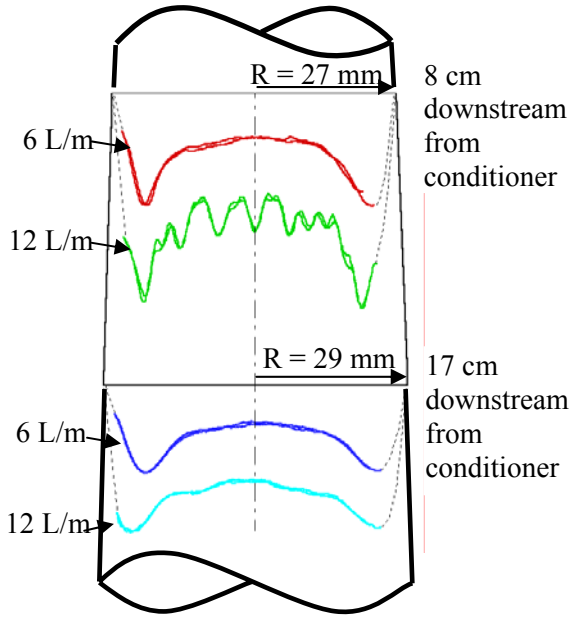

Figure 29. Velocity profiles in the test section of LWT

On the other hand, the local minimum on the axis of the test section deteriorates downstream, as we move further from the conditioner and the profile tends towards the fully developed form (see **Figure 29** at 17 cm). Thus, a long enough conditioner is needed in order to preserve a sufficient velocity well (velocity gradient) throughout the test section.

In the process of this research, the shape of the optimal velocity profile underwent significant evolution (**Figure 30**). Early flow conditioners were designed to stabilize an air bubble. It was found experimentally that the properties of air (negligible density compared to water) required a design with a deep, narrow well in the velocity profile at the center of the pipe. Though these conditioners were successfully used to keep large bubbles relatively stable near the pipe axis, it was decided that the velocity field was too different from that expected in the oceanic environment. Indeed, our fundamental investigations show that lateral and shape oscillations of a particle may play an important role in its free motion at a certain range of Re (see Chapter 5.0).

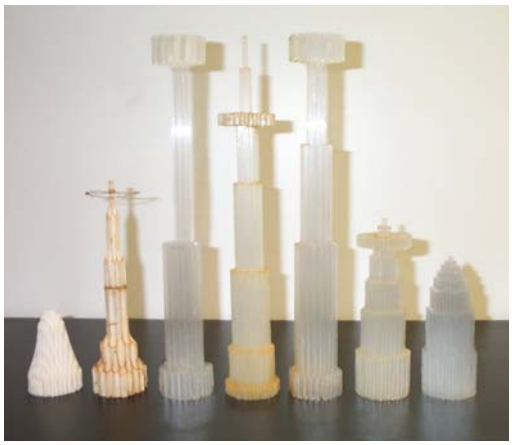

The narrow velocity well along with the high velocity gradients restricts the natural lateral motion of a particle, and alters the particle shape and flow patterns around it. These altered flow patterns can cause unrealistic mass transfer and material losses from the particle. They may also affect hydrate formation and dissolution kinetics.

Figure 30. Some conditioners tested in the LWT

The goal for more recent flow conditioners was to provide a wide velocity well with relatively low-velocity gradients near the center (as in Figure 15). Such a profile would keep a particle away from the wall and at the same time allow some freedom of lateral motion. It was also designed to keep the maximum velocity gradient in the profile as small as possible to minimize deviation from natural mass transfer conditions.

6.2 VERTICAL STABILIZATION

In order to estimate the effectiveness of both the passive and active mechanisms of vertical stabilization (see Section 4.2.2) and to optimize the geometry of the test section, a simple linearized one-dimensional model of vertical stabilization was developed and assessed experimentally.

6.2.1 One-dimensional model for vertical stabilization

Figure 31 depicts a test section of the HWT where the particle is stabilized and observed. The test section diverges in the direction of gravity, g, where the divergence angle is given by α. To prevent the particle from rising due to the buoyant force, F_b, an equal force is needed in the opposite direction. This drag force, F_d, can be created by a countercurrent flow in the direction of gravity (see Section 4.2).

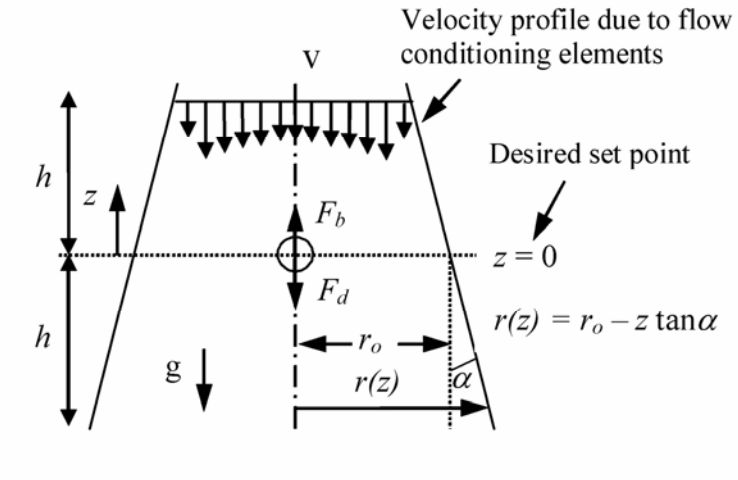

Figure 31. Diagram of a particle in the test section

If we take into account only drag and buoyant forces, then the vertical component of the equation of particle motion can be written as:

$$m_p \frac{d\,\mathrm{v}_p}{dt} = \frac{4\pi}{3}\rho_p R^3 \frac{d\,\mathrm{v}_p}{dt} = \frac{\pi}{2} C_D \rho\, \mathrm{v}_r^2\, R^2 + \frac{4}{3}\pi R^3(\rho - \rho_p)g = F_d + F_b, \qquad (55)$$

where $\mathrm{v}_r = \mathrm{v} - \mathrm{v}_p$ is the relative axial component of velocity of the flow with respect to the particle, v(z,t) is the centerline velocity and $v_p(z,t)$ is the axial velocity of the particle. To apply linear control theory, the drag force needs to be linearized about the velocity of interest (denote it by $\bar{\mathrm{v}}_r$). That is, an expression of the following type is sought:

$$F_d \approx \eta + \sigma \mathrm{v}_r \qquad \text{for } \left|\mathrm{v}_r - \bar{\mathrm{v}}_r\right| << \mathrm{v}_r, \tag{56}$$

where linearization coefficients η and γ should be found for a particular setpoint velocity $\bar{\mathrm{v}}_r$.

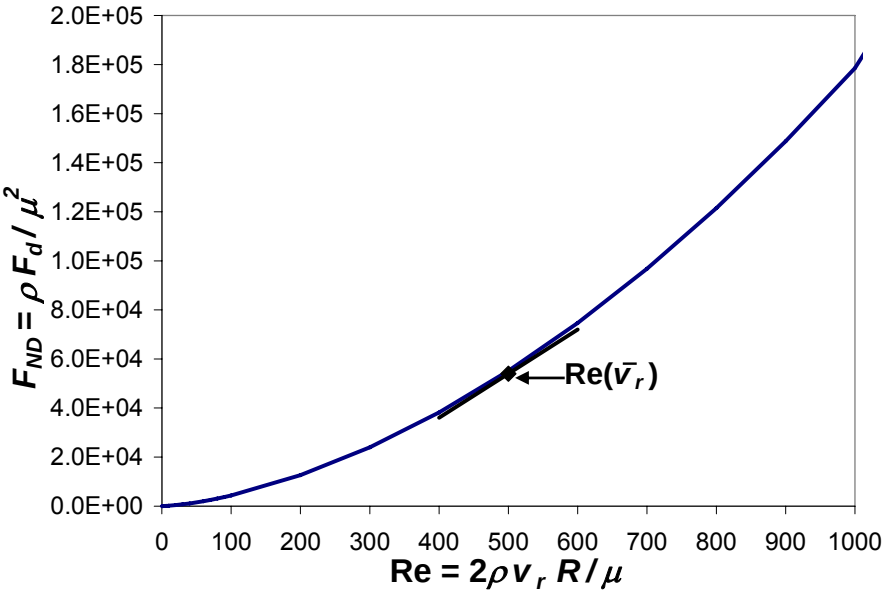

Figure 32. Linearization of non-dimensional drag force around the setpoint velocity $\bar{\mathrm{v}}_r$

Figure 32 represents a non-dimensional drag force for a spherical particle, F_{ND}, as a function of *Re* and shows the procedure of linearization around the setpoint velocity $\bar{\mathrm{v}}_r$. More details on the drag force linearization in given in Appendix D. Using a linearized drag force from Eq.(56), Eq.(55) can be written as:

$$m_p \frac{d\,\mathrm{v}_p}{dt} = \frac{4\pi}{3}\rho_p R^3 \frac{d\,\mathrm{v}_p}{dt} = \eta + \sigma(\mathrm{v} - \mathrm{v}_p) + \frac{4}{3}\pi R^3(\rho - \rho_p)g = F_d + F_b. \tag{57}$$

Next, the evolution of the axial velocity along the centerline of the diverging section is derived, based on the assumption that the centerline axial velocity is inversely proportional to the cross-sectional area:

$$\mathrm{v}(z) = \frac{\beta}{\pi r^2(z)}, \tag{58}$$

where β is a constant for a given flow rate, z is the vertical coordinate, and $r(z)$ is the test section radius at the vertical location z (see **Figure 31**).

Strictly speaking, Eq.(58) is not true for any velocity profile other than fully developed flow in a constant radius vessel. Particularly for profiles with a local minimum on the axis (see **Figure 15**), at very low flow rates and small divergent angles the velocity on the axis may even grow downstream. This is an unfavorable scenario causing loss of vertical stability of the particle. However, for moderate velocities (5-16 cm/s), when the desired vertical particle displacement (and even test-section length) is much smaller than the pipe development length, use of the approximation of Eq.(58) appears reasonable.

Then, simple geometric considerations and linearization with respect to z lead to the following expression for the axial flow velocity:

$$\mathrm{v}(z) = \frac{\beta}{\pi r^2} = \frac{\beta}{\pi}\left(r_o - z\tan\alpha\right)^{-2} \approx \frac{\beta}{\pi r_o^2}\left(1 + \frac{2\tan\alpha}{r_o}z\right) = \bar{\mathrm{v}}\left(1 + \frac{2\tan\alpha}{r_o}z\right), \qquad (59)$$

where $\bar{\mathrm{v}}$ is a steady state velocity[17] at the set point $z = 0$.

Assuming steady flow, the particle is steadily maintained at the setpoint, we have:

$$0 = \eta + \sigma\bar{\mathrm{v}} + \frac{4}{3}\pi R^3(\rho - \rho_p)g \qquad \Rightarrow \qquad \bar{\mathrm{v}} = -\frac{\eta}{\sigma} - \frac{4\pi}{3\sigma}R^3(\rho - \rho_p)g\,. \qquad (60)$$

Substituting Eq.(59) and Eq.(60) into Eq.(55), and rewriting Eq.(55) in terms of the particle location $z(t)$ ($\dot{z} = \mathrm{v}_p$, $\ddot{z} = d\,\mathrm{v}_p/dt$) gives:

[17] For the purposes of this section under steady state velocity we understand vertical flow velocity, which (through the drag law) exactly balances the buoyant force at z=0. This is typical terminology in the linear control theory for denoting a basic state. Then, perturbations to this basic state are applied and the response of the system is studied. Respectively, the steady state is understood as an ideal balance, when the particle is steadily maintained at z=0 (unrealistic situation, but useful as a reference case).

$$\overbrace{\frac{4\pi}{3}\rho_p R^3}^{m}\ddot{z}+\sigma\dot{z}+\overbrace{\left(\eta+\frac{4\pi}{3}(\rho-\rho_p)R^3 g\right)\frac{2\tan\alpha}{r_o}}^{b}z=0 \tag{61}$$

The system response to the spontaneous fluctuations of flow velocity v(*z*,*t*) will now be investigated. To achieve this, a perturbation component $\Delta_v(t)$ is added to the flow velocity:

$$\mathrm{v}=\bar{\mathrm{v}}\left(1+\frac{2\tan\alpha}{r_o}z\right)+\Delta_v(t), \tag{62}$$

where $\Delta_v(t)$ represents an input to the otherwise stationary system. Then, the final form of the linear control system equation for a particle in the divergent test section will be:

$$m\ddot{z}+\sigma\dot{z}+bz=\sigma\Delta_v(t) \tag{63}$$

6.2.2 Analysis of the dynamic model

The simple dynamic model (63) strikingly resembles a spring-mass-damper system, where the stiffness of the restoring element, *b*, is proportional to the tangent of the divergence angle α, and the factor σ is obtained by linearization of the drag law around the steady state velocity at *z* = 0. As is well known from linear stability theory, for certain combination of parameters, system (63) gives vertical oscillations of the particle in response to the flow perturbation. Obviously, these oscillations don't correspond to the natural motion of the particle in the column of water and, therefore, they are highly undesirable. Thus, the first goal was to determine the range of the divergence angles α, for which system (63) is overdamped (no vertical oscillations).

From classical control theory it follows that for critical damping:

$$\sigma^2=4bm. \tag{64}$$

Critical damping provides the quickest return of the system to equilibrium without overshoot. Thus, $b < \sigma^2/(4m)$ ensures that there are no oscillations in the system.

In order to estimate the range of divergence angles, α, that satisfies the above inequality, a numerical example was considered with the values of parameters typical for the HWT (see Appendix D). As a result, for the combination of geometrical and material parameters, considered in Appendix C, the following condition for no vertical oscillation was obtained: $\alpha <\approx 12°$. This is quite a large angle for a conical diffuser and, based on our one-dimensional model, it could provide a very good response time. However, such a large divergence angle causes flow separation and reverse flow near the wall of the diffuser. Moreover, even angles half this size (4°-5°) cause too rapid deterioration of the local velocity minimum downstream the diffuser and, hence, loss of the desirable velocity profile (see **Figure 15**). Therefore, an angle between 1° and 2° was recommended for the geometry of the test section in order to guarantee an acceptable profile throughout the entire test section. Employing such a "weak spring" requires that the diffuser be sufficiently long to ensure that the particle does not escape from it due to the perturbations typical for the system. Assuming the maximum size of a CO_2 particle to be about 2 cm, the following parameters of the diffuser were suggested: $r_o \approx 3$cm; $h \approx 15$cm (see **Figure 31**).

The next step was to assess performance of the chosen system. The linearized equation of motion (C13) obtained in the numerical example (Appendix D) for $\alpha = 1.4°$ gives a rather high damping coefficient: $\varsigma \approx 2.97$. This means the system is significantly overdamped and rather sluggish. Indeed, the impulse response performed in Appendix C has shown the settling time for the particle perturbed from the steady state to be about 20 s, which is unacceptably large (**Figure 33**). In addition, a zero steady-state error should be maintained in response to various drifts in the

system (temperature variations, particle size change due to dissolution, etc.).Therefore, a control system is required to reduce settling time (at least, to several seconds), eliminate steady-state error and provide better rejection of disturbances.

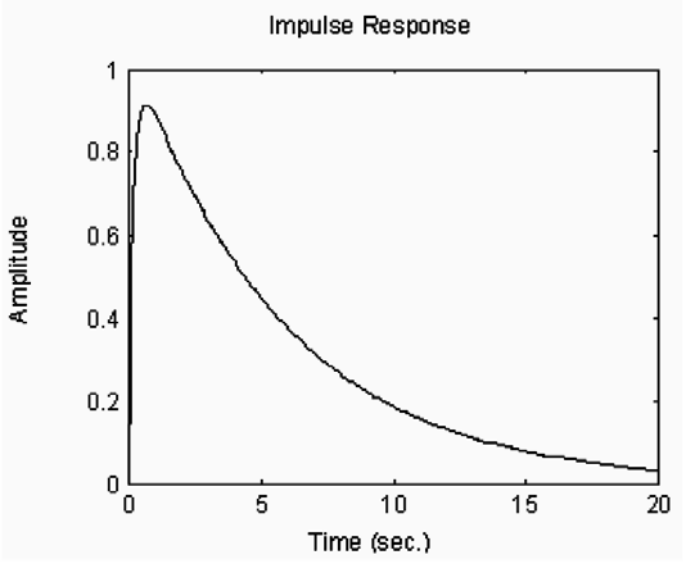

Figure 33. Open-loop impulse response for Eq.(C13)

6.3 DESCRIPTION OF FLOW PATTERNS IN THE TEST SECTION

Before discussing the control design for the optimized system, it is important to describe qualitatively the flow patterns inside the test section. **Figure 34**a depicts the flow conditioning element, chosen as an acceptable conditioner with respect to the considerations described above. It is composed of 4 mm OD plastic straws and has 7 annular layers of straws (see also the sketch in **Figure 28**) with the length of every layer increasing from periphery towards the center: 40 mm, 80 mm, 107 mm, 129 mm, 148 mm, 156 mm, and 163 mm. This conditioner creates a wide velocity well with reasonably low gradients and maintains the profile with a central local velocity minimum throughout the test section for a wide range of flow rates. **Figure 34**b shows

these profiles at various flow rates, measured using an automated traversing Pitot tube system (see Appendix C) through the cross section $z = 0$ (see **Figure 31**). Measurements were conducted in the test section with dimensions $r_o \approx 3$cm; $h \approx 19$cm (**Figure 31**). The conditioner was located at a distance ≈18 cm from the inlet of the diffuser. This configuration has been used extensively in the HWT for experimental studies of CO_2 droplets (see Section 6.5). Similarly, velocity profiles for various flow rates were measured through the ports located at $z = 5.7$cm and $z = -5.7$cm. They are provided in Appendix E.

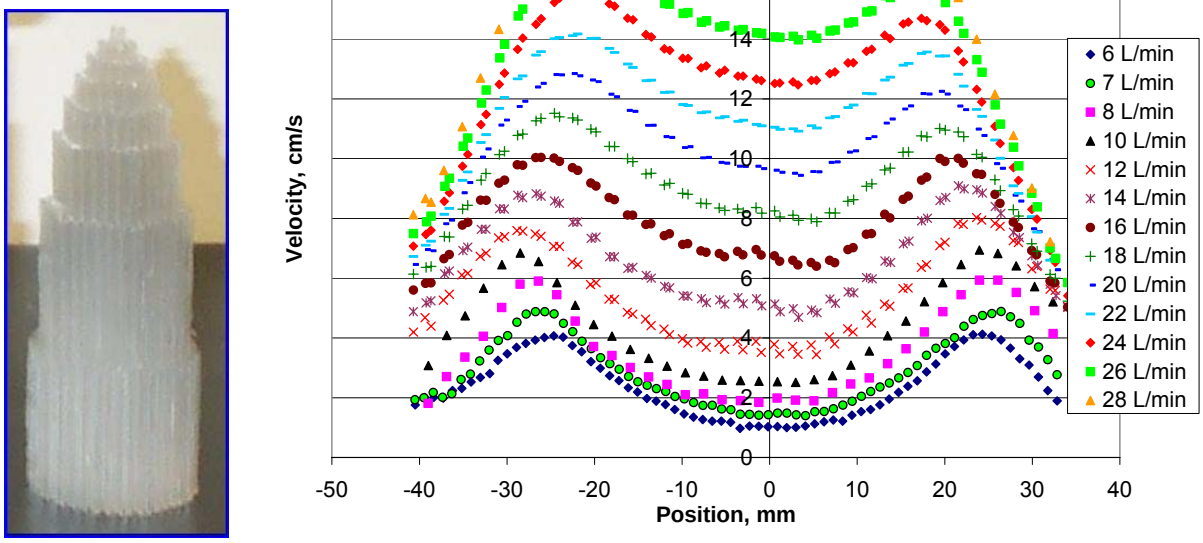

(a) (b)

Figure 34. (a) Flow conditioning element used in HWT and (b) velocity profiles measured at z=0 for different flow rates

Assuming the ideal case in which the observed CO_2 particle stays close to the axis of the test section, we may need to consider in detail the centerline axial flow velocity as a function of flow rate. This is important, because the flow rate will serve as the active control parameter used to adjust the vertical position of the particle in response to the system perturbations (see Section 6.4). Such a functional dependence can be obtained from **Figure 34**b, **Figure 51** and **Figure 52**

(Appendix E), if we consider the local velocity minima on the axis of the test section at various flow rates. **Figure 35** represents such a dependence at cross sections z = 5.7 cm, z = 0 cm, z = -5.7 cm (see **Figure 31**), referred to as the upper port, mid port, and lower port, respectively.

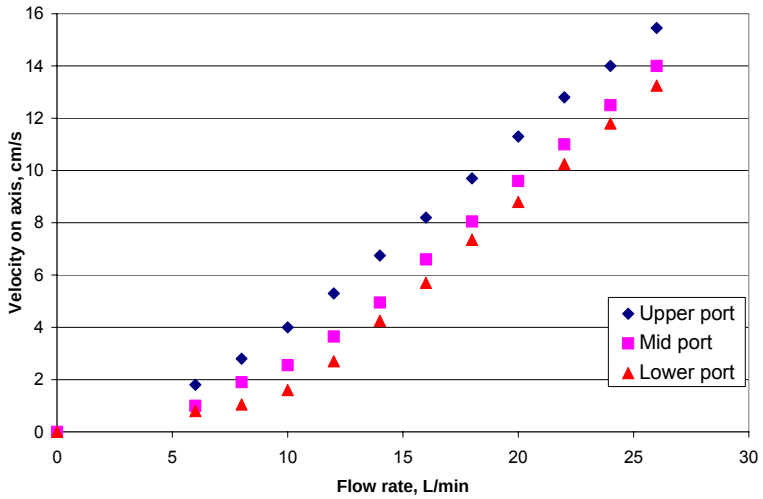

Figure 35. Centerline velocity in the test section as a function of flow rate

Below, we provide a qualitative discussion of these experimental results in order to comment on some interesting trends and to prove that the chosen experimental system satisfies the requirements set earlier for velocity profiles. First note that for every flow rate, the velocity on the axis of the test section decreases as we move downstream in the diffuser. That is, the favorable velocity gradient for particle stabilization in the vertical direction exists for all the considered flow rates[18]. This means that the decrease in velocity due to the expansion of the test section overwhelms the velocity growth on the axis due to the profile development.

It is quite peculiar that **Figure 35** demonstrates a nearly linear dependence of axial centerline velocity on flow rate for the velocities above approximately 3 cm/s. The Reynolds number corresponding to this region of linearity can be roughly estimated as:

[18] Even the most sensitive differential pressure transducer, used in conjunction with Pitot tube for velocity measurements, had problems for detection and precise measurement of velocities below 1 cm/s. Therefore, no data is provided for Q < 5 L/min.

$$\mathrm{Re} \approx \frac{5.5\ \mathrm{cm/s} \cdot 6.2\ \mathrm{cm}}{0.01\ \mathrm{cm}^2/\mathrm{s}} = 3410\,. \tag{65}$$

Based on **Figure 34**b, the average velocity corresponding to 3cm/s on the axis was estimated as 5.5 cm/s, and the diameter of the experimental test section is 6.2 cm at $z = 0$. This magnitude is quite close to the critical Re for the transition from laminar to turbulent flow in a circular pipe.[19] Although no special precautions were taken to make the pipe smoother, a slightly elevated magnitude of critical Re may be due to the presence of the conditioner upstream, which diminishes flow perturbations.

The transition from laminar to turbulent flow causes restructuring of the flow, enhanced mixing, and, hence, faster growth of the local velocity minimum on the axis with flow rate. This higher rate of velocity growth is observed in **Figure 35** for flow rates above approximately 10-11 L/min.

6.4 CONTROL DESIGN

A control system was developed to speed up the system response and maintain the vertical position of the particle by varying the velocity perturbation, $\Delta_v(t)$. This control system is based on the linearized equation of motion given by Eq.(63). Note that the controller will also work to linearize the system response, helping to justify the linearization of the system equations in Section 6.2.1.

The experimental facility has a variable speed pump (Autoclave Engineers ¾ HP MagnePump®) with a digital controller that permits fine flow rate (and hence, axial flow

[19] The velocity profiles for high flow rates in **Figure 34**b look smooth, because the Pitot tube measures a temporal average of velocity overall a finite time period and therefore cannot measure turbulent fluctuations.

velocity) adjustment. An automatic image analyzing system created in the LabVIEW environment detects and digitizes the particle location within the viewing window with high precision. Thus, both an adjustable input and a precisely measured output are available for the control system.

It is important to check the linearity and bandwidth of the mechanisms responsible for the flow rate adjustment. For the variable speed pump used in the unit, an experimental curve was obtained for flow rate as a function of pump speed. In the range of 1-32 L/min this curve fits the following linear equation very well:

$$Q = 0.324 \cdot P - 1.03, \quad \text{with } R^2 = 0.9996, \tag{66}$$

where Q is the flow rate in LPM, and P is the percentage of the full pump speed. Thus, the flow rate generated by the pump is linearly proportional to the voltage of the input signal. **Figure 35** gives a local velocity minimum at $z = 0$ as a function of the flow rate in the system. For Q > 11 L/min this function is already linear, so no linearization is needed in this range for the linear control analysis. As for lower flow rates, a non-linear transition is present. Assuming the range of flow rate variations for stabilization purposes is rather small compared to the mean flow rate, linearization around the mean value of the flow rate seems appropriate. Accepting this linearization along with Eq.(66), one can consider velocity as a linear function of the feedback voltage signal. Thus, linear control analysis is applicable in the first approximation, although we may expect some problems in the range of lower flow rates.

Conservatively assuming that fine flow rate adjustment does not exceed 10% of the overall pump speed range, the pump response can be reduced to at least 0.25 sec. This is quite a large delay, and when incorporated into the theoretical model, can significantly degrade the controller performance.

A PID (proportional-integral-derivative) controller was chosen, given their performance and robustness for servo control applications [88, 89]. The overdamped character of the response suggests a derivative controller was not necessary. However, proportional and integral terms are required in order to speed up the system and bring the steady-state error to zero.

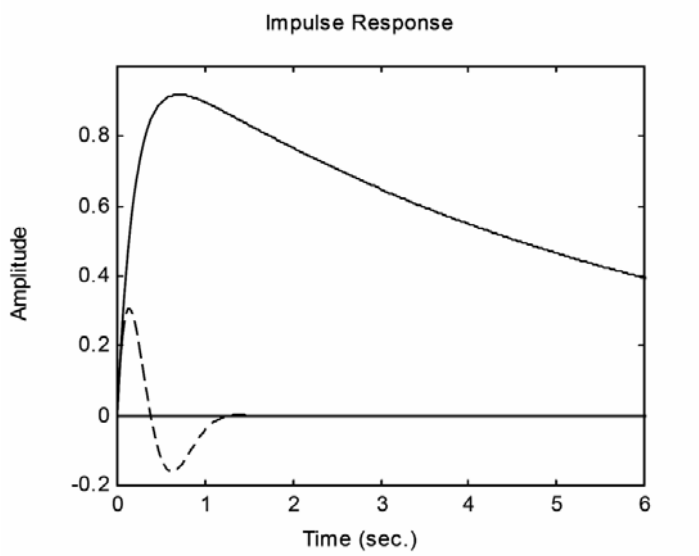

Figure 36. Open- (solid line) and close-loop (dashed line) responses (PID gains K_p=12, K_i=25, K_d=1) of the system given by Eq.(C14)

As discussed at the end of Section 6.2.2, desirable performance of the system would include a relatively fast settling time (several seconds) and a zero steady-state error. Heuristic tuning of the control gains produced the following values for the PID gains, respectively: K_p=12, K_i=25, and K_d=1. Note that some derivative control was ultimately introduced to suppress the high amplitudes of the integral controller and to remove oscillations caused by the proportional gain. **Figure 36** shows the simulated open-loop and closed-loop impulse responses for the system, respectively. For the closed-loop response, the amplitude of the output signal was significantly reduced, the settling time decreased to about 1-2 sec. and the steady-state error was zero. Thus, the performance objectives for the system were met in simulation using PID control.

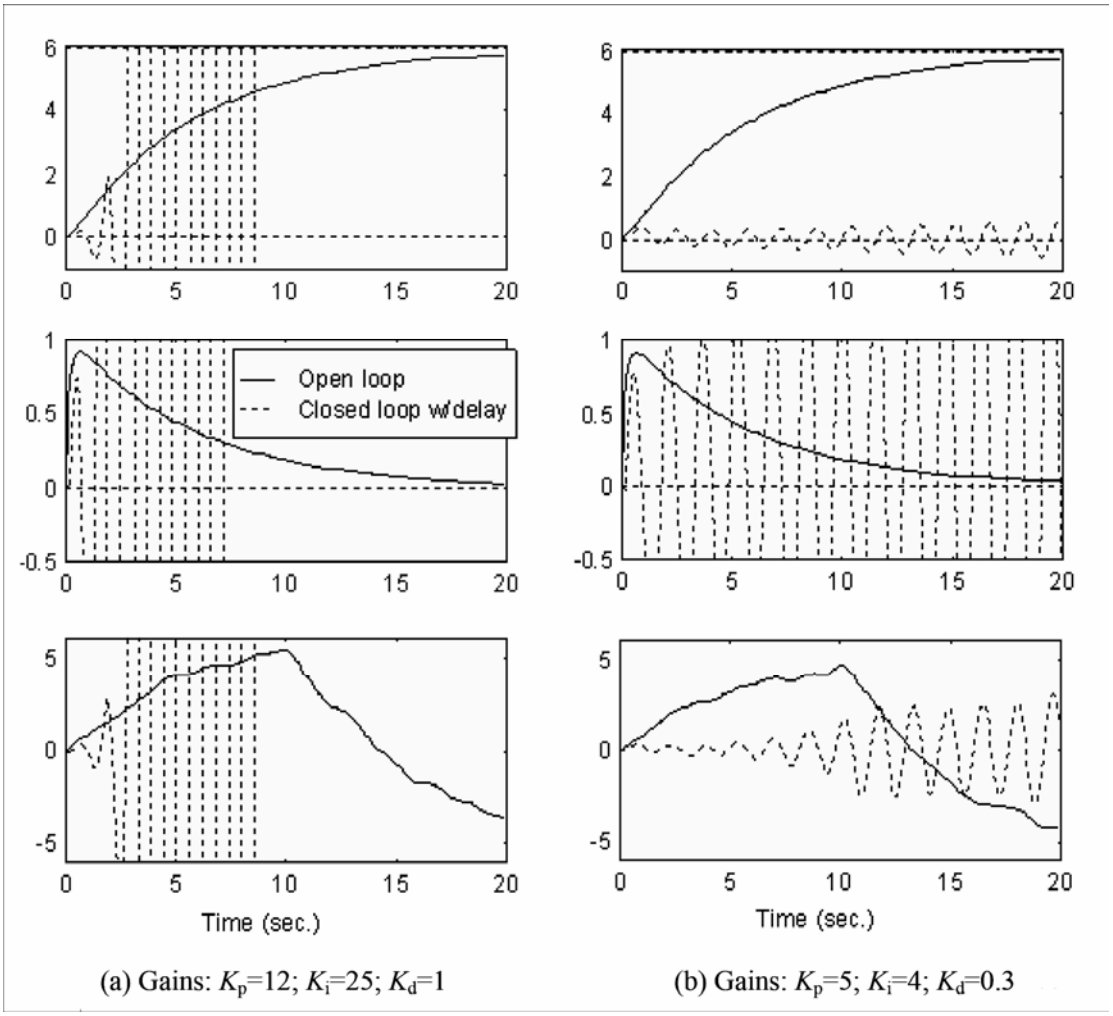

Figure 37. Response of system given by Eq.(C14) with delay and noise to the step (top), impulse (middle), and 10 sec. square wave (bottom) perturbations for two different control gain sets shown.

The successful result for the control design above will dramatically change if we add features of the real hydrodynamic system, i.e., the pump delay (about 0.25 sec.) and a high level of noise (order of magnitude of step perturbation). **Figure 37**a shows the simulated step response (top left), impulse response (middle left) and square wave response (bottom left), predicted by the transfer function (C15) with the transport delay added using a Padé Approximation [90]. Optimal gains, obtained earlier for the ideal system without delays (K_p=12, K_i=25, K_d=1), are now

unacceptable, that is the amplitude of oscillations grows and the particle loses stability. Even for significantly lower magnitudes of gains (K_p=5, K_i=4, K_d=0.3) the system is still unstable (**Figure 37**b). One may think that increased derivative control could suppress these unfavorable oscillations. However, application of a large derivative control is problematic for real systems with a very high level of noise [89]. Indeed, large values of K_d applied in the experiment with moderate K_p and K_i lead to instability even more rapidly. Thus, to ensure stability, the PID gains must be significantly reduced. The square wave system response with PID gains that have a stable closed-loop response is shown in **Figure 38** (K_p=0.5, K_i=0.3, K_d=0.15).

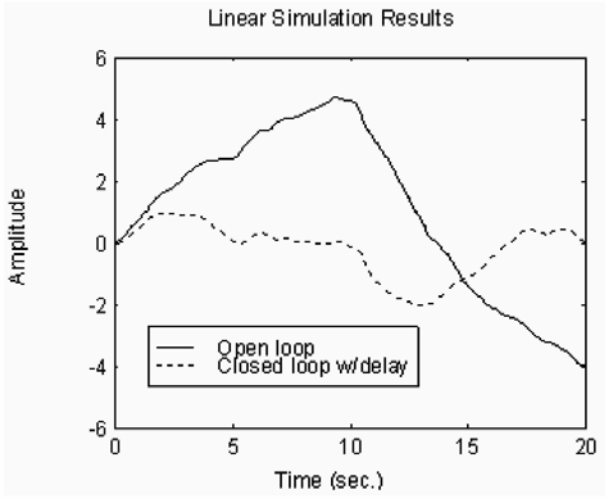

Figure 38. Square wave (period 10 s) response of system given by Eq.(C14) with delay and noise (PID controller gains: K_p=0.5, K_i=0.3, K_d=0.15)

Several comments should be made about the results of the simulation. First, with such modest control gains (**Figure 38**), a large reduction of amplitude and settling time are not expected. Indeed, although some improvements are observed (i.e., settling time reduced to 5-7 sec., steady state error is zero), they are not as dramatic as for the hypothetical system without delays and noise.

6.5 CO_2 DROPS IN HWT AND STABILIZATION PROBLEMS

6.5.1 Validation of the stabilization model

A preliminary set of experiments in HWT was conducted to validate the above developed model and control design. The following data were obtained at a water pressure of 15.3 MPa (2200 psig) and a temperature of 280 K (7°C). The initial equivalent diameter of the CO_2 particle was about 13 mm. Over the course of 30 minutes, the particle diameter decreased to approximately 6 mm, at which time the particle was lost. Thus, the Reynolds number varied approximately from 900 to 400 as the particle dissolved in water. The average flow rate required to maintain the particle in the observation window was about 20 L/min. Based on **Figure 35**, this flow rate approximately corresponds to 9.5 cm/s velocity of the countercurrent flow in the center of the test section. This value is in a reasonable agreement with the equilibrium velocity obtained in Appendix C.

The first set of experiments was performed to compare the behavior of a particle in the open loop system to the system with PID control. In both cases (with and without PID control), a particle with initial equivalent diameter of 1.25 cm was observed in the test section under the following conditions: T = 6.7-6.8°C, P = 150 bar. Vertical position of the particle was recorded in the data file every 0.1 sec. PID control was realized by the variable speed pump (see Eq.(66) for pump characteristics). To be able to compare the results with the theoretical model, the same magnitudes of PID gains were chosen as in **Figure 38** (K_p=0.5, K_i=0.3, K_d=0.15). **Figure 39**a (long term behavior) and b (short term behavior) show the results of these experiments. Note that the horizontal dashed lines in **Figure 39** represent the boundaries of the circular observation window, which is contained within 3 cm on the ordinate. Ideally, the particle should be within

these boundaries at all times. Over a long term scale, a significant steady-state error is observed for the open loop system, where the particle position after 1200 seconds is completely outside of the range of the observation window. In contrast, the PID controller maintains the integral average particle position at the center of the circular window at all times (**Figure 39**a). Some improvement was also noticed over short term scales (**Figure 39**b). When comparing excursions of the particle outside the horizontal dashed lines, it was observed that the closed loop system had fewer occurrences, that were shorter in duration and that generally did not stray as far away. Although, with the PID controller, the particle was located within the observation window about 90% of the time, it was impossible to completely eliminate the sudden "bursts" from the field of view, typical for the system without feedback control. However, as predicted earlier, one should not expect dramatic improvement for such modest PID gains. Attempting to increase gains above approximately one unit caused noticeable oscillations and then instability of the experimental system, as was qualitatively predicted by the model with delay. The magnitudes of the pure proportional gain at the onset of instability were found to differ slightly between the theoretical model ($K_p \approx 1.1$) and experimental system ($K_p \approx 0.8$), which was not surprising, keeping in mind the level of simplifications in the model.

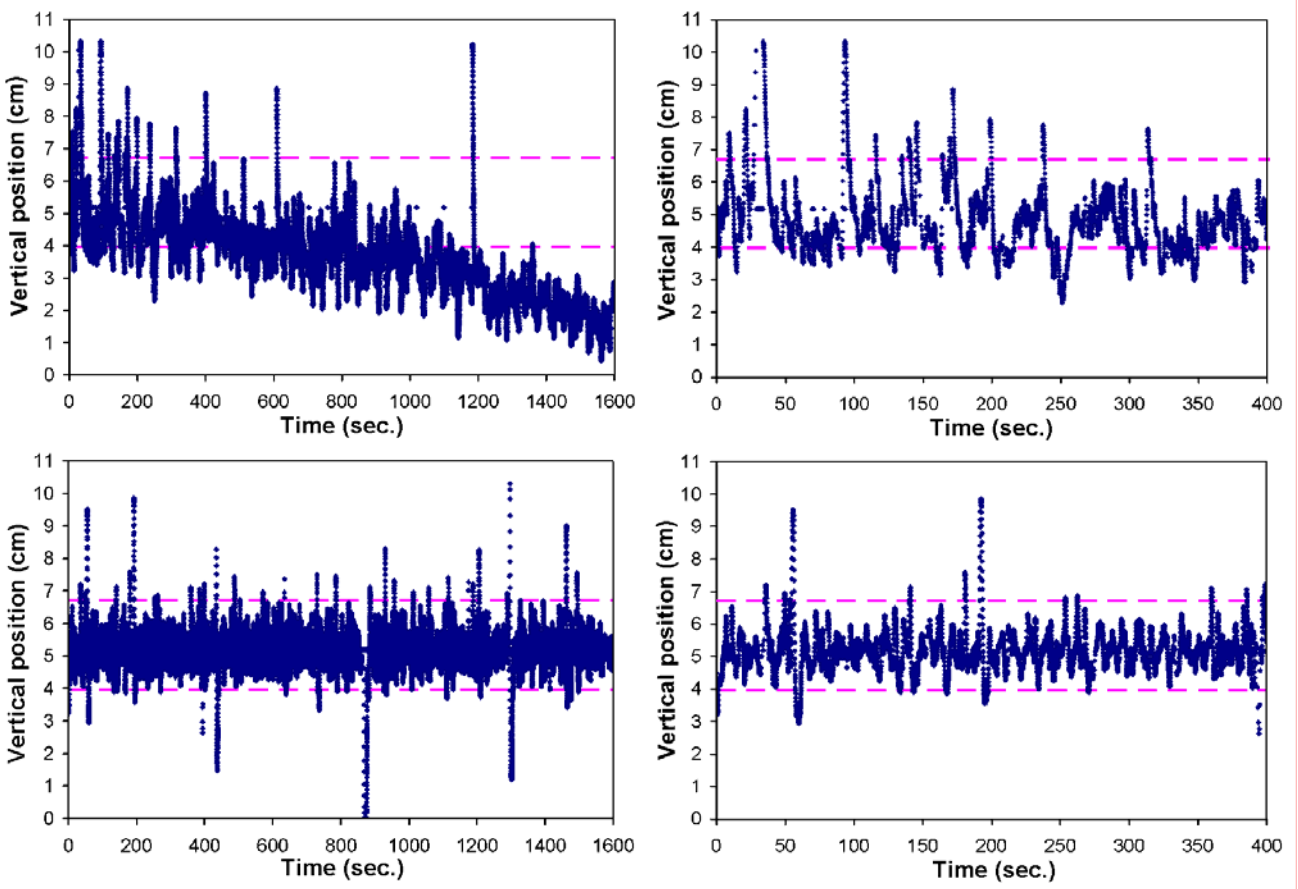

(a) (b)

Figure 39. Long term (a) and short term (b) CO_2 drop behavior in HWT (top figures represent experiment without feedback control, bottom figures – with PID control K_p=0.5, K_i=0.3, K_d=0.15). Initial diameter of CO_2 drop was 1.25cm, T = 6.7-6.8°C, P = 150bar.

Another set of experiments was performed under the same conditions and served to compare the approximate square wave response of the system with the theoretical one. Opening and closing a bypass ball valve installed in the system simulated a square wave disturbance. A sudden closing of this valve caused abrupt growth in the flow rate through the test section. **Figure 40** presents the square wave disturbance response (a) for the open loop and (b) for the closed loop (K_p=0.5, K_i=0.3, K_d=0.15) systems. The square wave disturbance signal that was sent to the bypass valve is shown at the bottom of **Figure 40** (a) and (b). The PID controlled system stayed within the viewing window boundaries (horizontal dashed lines) for the bulk of the test duration, in contrast

to the uncontrolled particle that was predominately outside of the viewing window. In addition, the uncontrolled particle (**Figure 40** (a)) did not completely reach a steady-state average position 20 seconds after switching the valve, while the closed loop system is brought back to the center of the observation window within 5-8 seconds. These settling times are quite close to the values obtained from the theoretical model (**Figure 33** and **Figure 38**). One important difference between **Figure 40** and **Figure 38** is the presence of a dominant frequency in the spectrum of noise for the experimental data of about 0.5-0.7 Hz. This frequency is beyond the bandwidth of the PID controller. Actually, it reflects a real physical phenomenon, namely the helical/rocking motion of a particle with a period of about 1.5 sec. To preserve the most natural behavior of a particle, this frequency should not be suppressed and thus the PID controller with modest gains successfully meets this need.

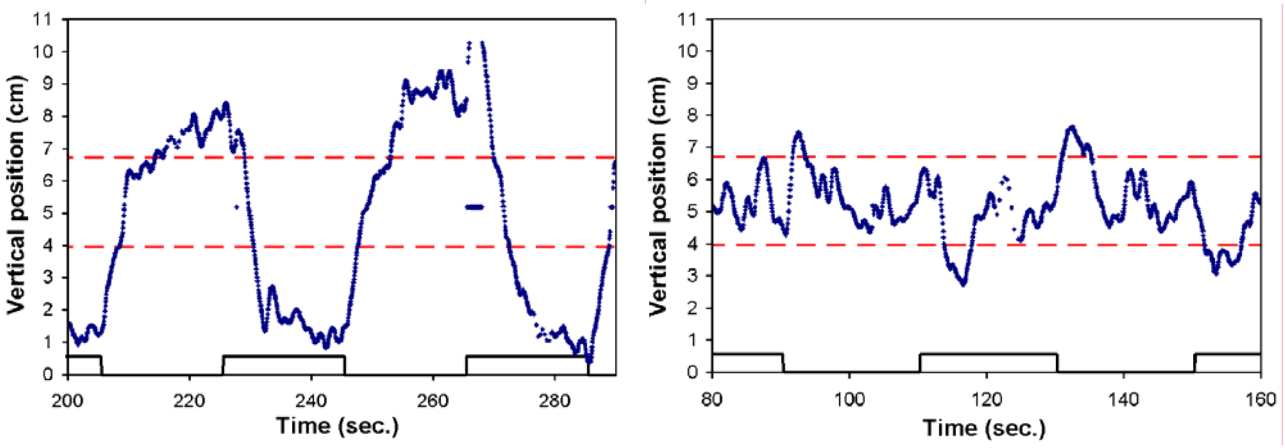

Figure 40. CO_2 response to square wave: (a) open loop and (b) with PID control (K_p=0.5, K_i=0.3, K_d=0.15)

6.5.2 Stabilization problems and limitations

It is clear that any chosen design of the test section works best for a particular range of experimental parameters (e.g., size of CO_2 drop, temperature, pressure). As we step too far away

from this most favorable range, we may need a different configuration for optimal stability. A good example of such behavior is demonstrated in the experiments with almost neutrally buoyant particles. As was noticed in Section 6.2.1, Eq.(58) is far from being true at very low flow rates. Indeed, for low velocities in the center (≈ 0.2-0.4 cm/s were observed for nearly neutrally buoyant particles at the simulated depth of 2,000-2,500 m), the profile development length is comparable with the length of the test section. Therefore, despite the slight expansion of the test section, the axial velocity in the center may grow downstream due to flow restructuring towards fully developed. Hence, the favorable velocity gradient in the axial direction is lost. **Figure 41** displays a velocity profile development downstream for low velocities in the LWT (1.2° diffuser angle), obtained by a numerical simulation using ADINA commercial package. In this numerical problem, a diffuser is considered with inlet diameter, D_1 = 5cm, outlet diameter, D_2 = 6cm, and length, L = 24cm. After the diffuser, a straight, 200cm long and 6cm in diameter, section of pipe is considered. Axial symmetry of the problem is assumed. No slip boundary condition on the walls is considered, and profile with velocity minimum on the axis is given at the inlet of the diffuser (see profile at z = 0 in **Figure 41**). Zero traction boundary condition is assumed at the outlet.[20]

[20] This relatively simple numerical simulation was performed using ADINA commercial package and is possible because the flow in the diffuser is laminar at these magnitudes of velocity.

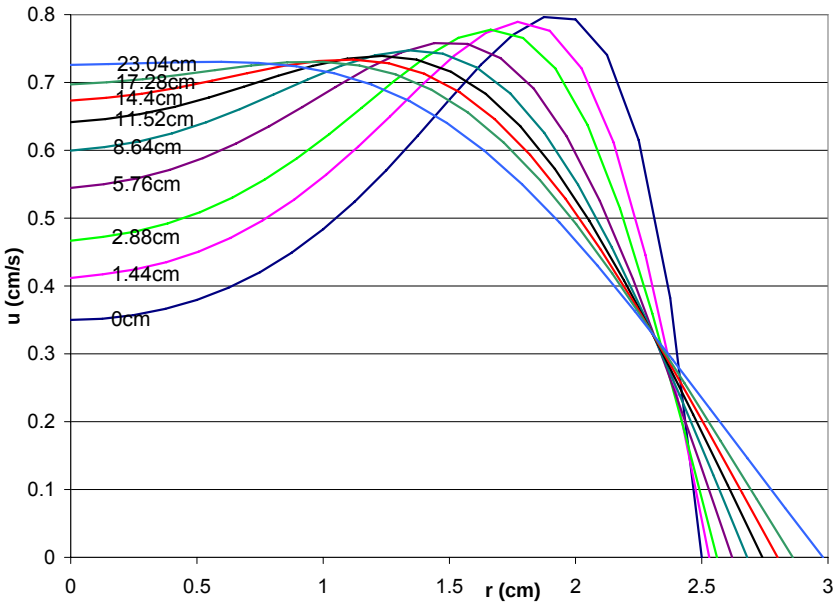

Figure 41. Velocity profile development along divergent test section of the LWT: D_1=5cm, D_2=6cm, L=24cm; Q=0.7 L/min. Axial symmetry is assumed. Velocity profile with local minimum on the axis is given at z = 0 (labels indicate distance downstream from initial profile)

The diffuser angle for the HWT was chosen to be a little larger (1.65°) in order to reduce the aforementioned trend towards lower velocities. However, although the passive vertical stabilization does not work, the velocities are so low that the feedback control system is able to maintain the desirable vertical position of the particle even for the modest gains introduced above. It is interesting that sometimes these "slow" particles were even better stabilized in the lower test section (see **Figure 16**) by a flattened velocity profile (conditioner is very remote – more than 10 pipe diameters from the particle) and in unfavorable velocity gradient (contraction instead of expansion in the direction of flow). It means that complications associated with introduction of the diffuser geometry into the system are unnecessary for a nearly neutrally buoyant particle. It can be successfully stabilized (vertically) by feedback control in even a straight section of pipe.

As the average flow rate required for particle stabilization falls below Q ≈ 11 L/min, the linearization coefficient for the axial velocity as a function of Q decreases (see **Figure 35**). Thus, a little more aggressive control is required in this range, while for Q > 11 L/min this aggressive control may push the particle out of the viewing window. Thus, additional problems with stabilization should be expected, when we work in the vicinity of this flow rate.

While only a narrow subclass of particles faces the transitional flow in the test section (Q ≈ 11 L/min), practically all the experimentally considered CO_2 particles undergo bifurcation from non-rectilinear to rectilinear regime of motion in the course of their dissolution (see Section 6.5.3). In this zone of bifurcation and possibly conditional stability (see Section 5.2.4) Eq.(D5) is not valid, and precise linearization of the drag is impossible. Since some range of uncertainty exists here (between the lower and upper drag curve), we should not expect a very good stabilization in this zone.

In Section 6.3 we considered an ideal case, when the particle always remains on the axis of the test section. In practical experiments, the particle repeatedly deviates from the axis, sometimes quite significantly. Although we tried to make sure that the gradients of the velocity profiles are rather low, they still exist. And such lateral deviations of the particle interfere with the control system (by altering the velocity which faces the particle in a particular cross section). This essentially three-dimensional interaction challenges the particle stability and affects performance of the system.

To assess the behavior of (almost) spherical CO_2 particles in HWT, some experiments with solid spheres in LWT were performed, **Table 3** (conditioner described in Section 6.3 was used).

Table 3. Stability of solid spheres in LWT

d_{ball} (cm)	ρ_{ball}(g/cm^3)	Q(l/min)	D_{pipe}(cm)	V_{av}	Re_{pipe}	
2.54	0.83	30	6	17.68	10610	"slowly" migrates to center & suddenly kicked toward wall
2.54	0.99	3.7	6	2.18	1309	Almost ideally in the center
1.8	0.99	1.4	6	0.83	495	Almost ideally in the center
0.8	0.99	0.8	6	0.47	283	about 1/3 pipe radius from the wall

All the liquid CO_2 particles considered in the experiments in the HWT can be roughly subdivided into three categories:

1. $0.99 < \rho_p / \rho < 1.01$, typically corresponds to larger depths (2,500-3,000m)

   Since only low velocities are needed in the countercurrent flow, the particles are typically close to spherical. Easy vertical control (can be done manually), but with very poor lateral stability. Particles slowly migrate in lateral directions and are often lost from the viewing window.

2. $0.95 < \rho_p / \rho < 0.99$, corresponds to depth 1,500-2,000m

   Larger particles in this regime (D_{eq} > 0.7 cm) have higher non-sphericity (D_{max}/D_{min} ≈ 1.2-1.3). They can be successfully controlled in the HWT. As particles dissolve to the size D_{eq} ≈ 0.5-0.6cm, they becomes more spherical (D_{max}/D_{min} < 1.1), and the stability declines. They repeatedly move toward the periphery, and, if they move too far from the central axis, they can be washed away by higher peripheral velocities.

3. $\rho_p / \rho < 0.95$, corresponds to shallower depths (around 1,000m)

   In this regime, particles have the highest non-sphericity (D_{max}/D_{min} is up to 1.5 for D_{eq} > 1cm). The particles slowly migrate to the central axis and suddenly kick away towards the wall and upstream. This trend is not as violent as for solid spheres (see **Table 3**), presumably, due to the non-sphericity. So, these particles are reasonably controllable in the HWT, although some adjustment in control is needed (see discussion below).

Larger drops (D_{eq} > 1cm) from categories 2 and 3 often demonstrated shape oscillation.

Based on these experiments, we make several conjectures about the three-dimensional behavior of various particles in the test section. Although the particle normally "prefers" to sit in the local velocity minimum on the axis of the test section, there is a competing lift force (acting in the direction of the velocity gradient), which tends to move the particle towards the peripheral annulus with local velocity maximum. The magnitude of this force depends on the velocity gradient, particle size and shape. Particles with larger buoyancy require higher velocities for maintaining them in the test section. Hence, when perturbations shift them from the axis of the test section to the location of maximum gradient (see **Figure 15**), they have to face a larger lift force. This causes a "sudden kick" towards the wall, alters the vertical balance by higher than necessary velocity, and wipes the particle from the observation window downstream. Such a behavior was observed in the HWT in the experiments simulating 1000m depth in the ocean at the temperatures 4°C-18°C, as well as for 1500 m at the temperatures above 10°C. For these conditions, the density ratio, ρ_p / ρ, was less than 0.95. Due to this behavior, highly buoyant particles ($\rho_p / \rho < 0.95$) were maintained in the upper third of the observation window in order for the active control system to react in a timely manner on such "sudden kicks." As for the almost neutrally buoyant particles, the difference between the velocity local axial minimum and local peripheral maximum is so small, that the lift force is practically negligible. The biggest problem for such particles is their lateral migration: the lateral restoring force is negligibly small, so migration is very slow and, if the particle is located in the periphery of the test section, it may take up to several minutes to migrate laterally towards the center (to the viewing window).

Is it interesting that better stability in the test section was demonstrated by non-spherical particles. This may be explained by the fact that the unfavorable lift force in a gradient flow is

more pronounced for spherical particles. As for the behavior of non-spherical particles after the bifurcation to non-rectilinear motion, particle rocking gives an effect similar to the change of an angle of attack for a wing. This causes an intermittency in the lift force (it changes direction to opposite every half period of rocking), which overwhelms the lift caused by a relatively weak velocity gradient.

As it was mentioned in Section 3.2, Morton numbers and density ratios of the corn and castor oils in water are quite close to the corresponding properties of carbon dioxide drops at the depth of 1,000-1,500 m. This fact justified the approach in using the oil drops in the LWT as benchmark particles. Observations of the oil drops and optimization of the test section of the LWT were performed, assuming similar behavior of the CO_2 drops in the HWT of the same configuration. Oil drops of medium sizes (up to several mL) were successfully stabilized in the LWT, using the geometry close to one described in Section 6.3. However, later experiments with CO_2 drops in the HWT have revealed some differences in behavior with respect to supposedly hydrodynamically similar oil drops. Basically, this was the first suggestion that particle viscosity (which is typically neglected in contaminated media) can play some role in certain regimes of motion. Indeed, the high viscosity of oils suppressed the particle shape oscillations in the LWT, while oscillations were often observed for the carbon dioxide particles in HWT. Later, this effect of particle viscosity was confirmed by the experiments in the Water Tank (see Section 5.2.5). **Figure 42** compares the drag for the CO_2 drops in salt water [71] with that of oil drops in water and provides additional evidence for the above discussion. Although the data for the CO_2 drops show rather large scattering, they evidently demonstrate an earlier bifurcation from the rectilinear regime (Re ≈ 800-1000 for CO_2 versus Re ≈ 1400 for oils). According to the

conclusions in Subsection 5.2.5, this fact indicates the presence of shape oscillations for CO_2 drops starting from Re ≈ 800-1000.

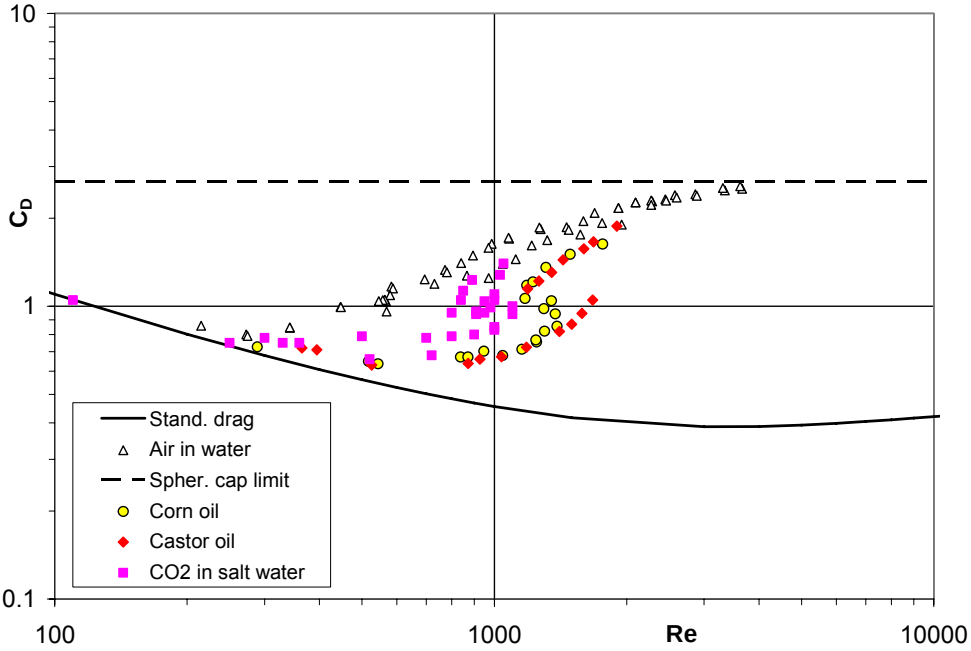

Figure 42. Onset of bifurcation in drag: CO_2 in salt water [71] versus oils in water

6.5.3 Effect of regime of motion on CO_2 particle dissolution rate

The ultimate goal of the experiments with CO_2 droplets in the HWT was to assess their fate under conditions simulating the deep ocean. Although the dissolution and mass transfer from the carbon dioxide particle in water is not within the scope of the present work, they are addressed here as far as they are affected by the hydrodynamic behavior of the particle. **Figure 43**a,b,c,d shows the dissolution of CO_2 particles over the course of time at various medium conditions. For a spherical particle, the dissolution rate is equivalent to the change of radius, so it is quite common to measure dissolution in terms of particle radius change, dR/dt. In case of non-

spherical particles, equivalent radius generalization can be used instead (see Section 1.3 for definition).

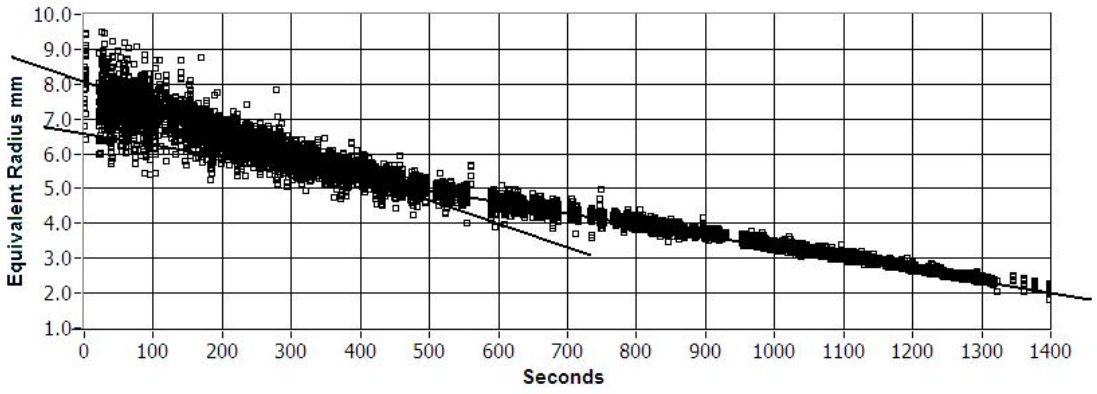

1000m, 18°C

a.

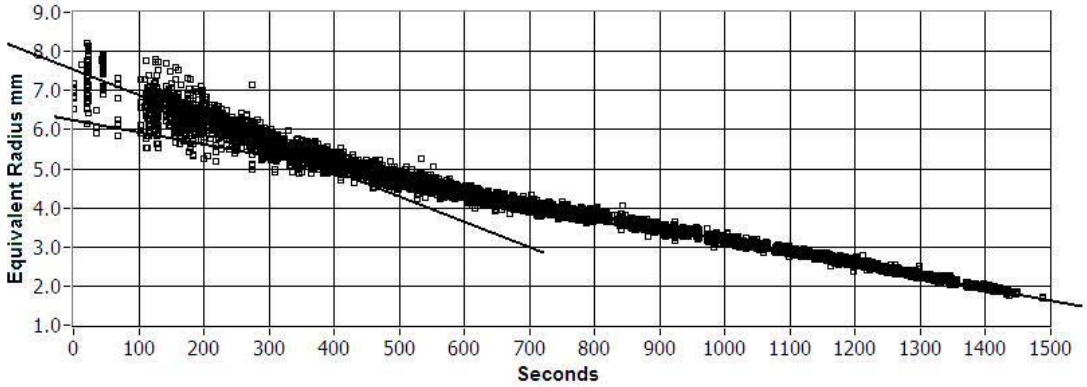

1500m, 18°C

b.

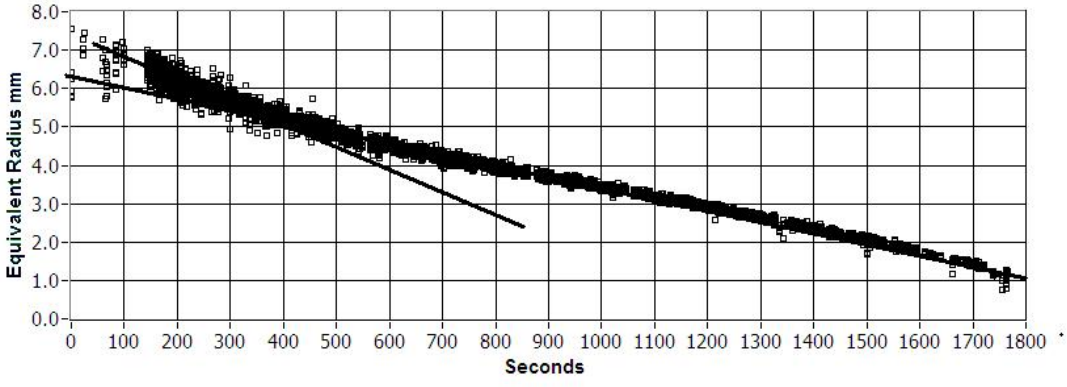

2000m, 18°C

c.

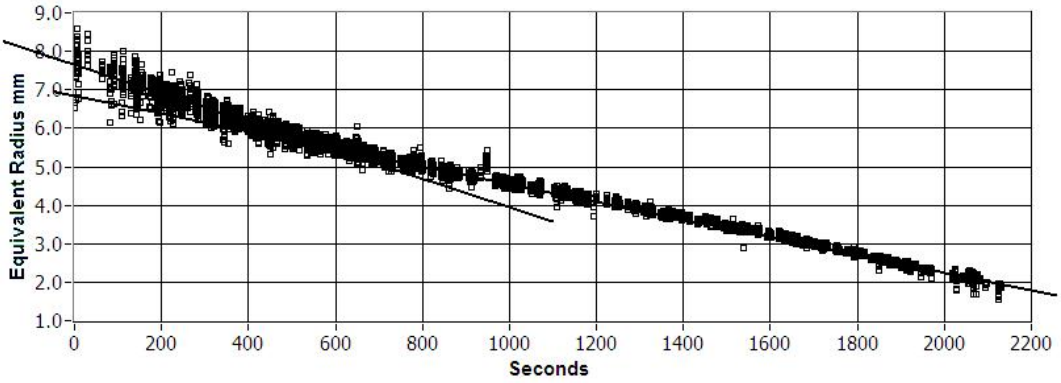

2500m, 18°C

d.

Figure 43. Experimental results on particle dissolution data in simulated deep ocean under various conditions

Dissolution rate depends on the medium conditions, so we would expect dR/dt to be constant for fixed conditions. But every set of data in **Figure 43** demonstrates two essentially different slopes. Recall that larger particles are typically more non-spherical and they tend to a spherical shape during the course of dissolution. However, it can be shown (see Appendix F) that the non-sphericity observed in our experiments increases dissolution rate by at most 3%. In addition, particle non-sphericlity changes very gradually and therefore cannot be responsible for such a sudden change in slope of $R(t)$.

The nature of the slope change suggests the possibility of a bifurcation. In order to evaluate this possibility, both the Reynolds number and the drag coefficient were assessed and the particle behavior was investigated in the region of the sudden change of dissolution rate for various experiments. Due to the nature of the experiments in the HWT (temporal variation of flow rate for particle stabilization, particle axial and/ or lateral migration), we do not expect as good precision of drag data as we had in the water tank experiments. However, these data can shed some light on the aforementioned behavior of the dissolution rate. Experimental data from the HWT in the region of the suspected bifurcation of the dissolution rate are shown in **Figure 44**

and they represent various oceanic depths (1000, 1500, 2000, and 2500 m) and temperatures (10°, 14°, and 18°C) for both rising and sinking particles. Only CO_2 drops with a density difference $\Delta\rho > 0.025\,\mathrm{g/cm^3}$ were considered, because a significantly higher precision of measurements is required in order to obtain meaningful results for almost neutrally buoyant particles.

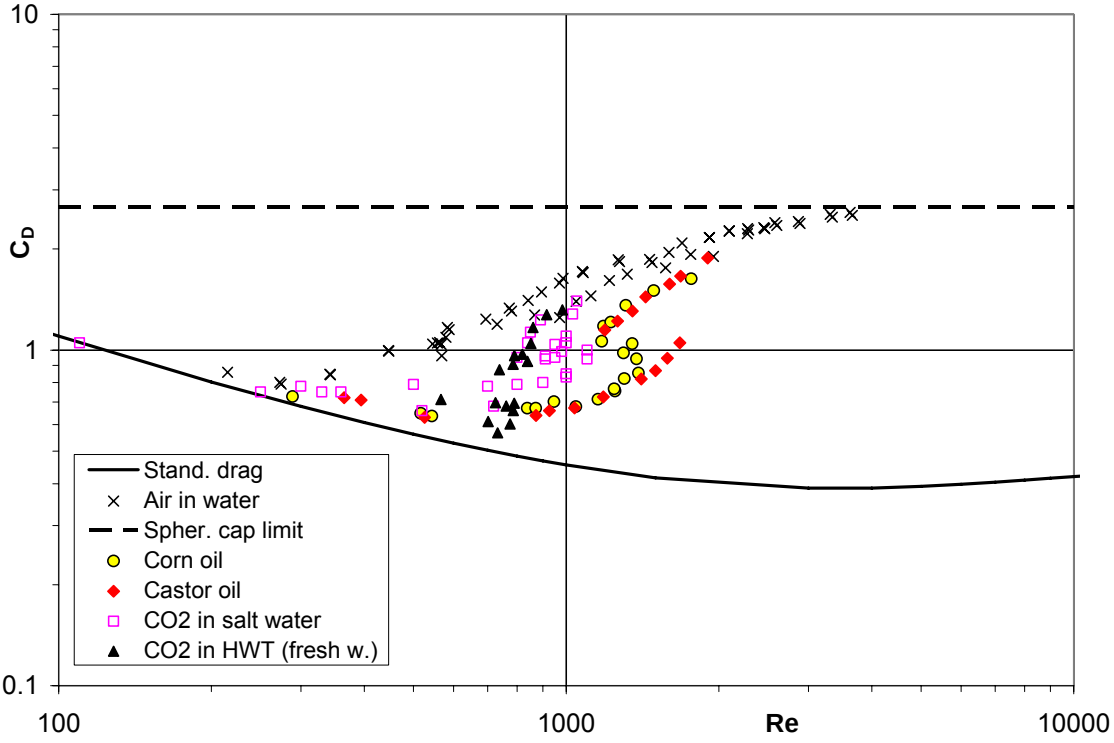

Figure 44. Experimental data for CO_2 drops in HWT, corresponding to the bifurcation in the dissolution rate (also, data from Figure 42 are reproduced for comparison).

These experimental data are in the region of a very sharp growth of drag and they correspond to the CO_2 drops behavior, reported in **Figure 42.** This confirms the hypothesis that the abrupt change in dissolution rate corresponds to a change in the regime of motion (from non-rectilinear to rectilinear) of the CO_2 particle. A change in regime of motion should certainly alter the mass transfer. Indeed, periodic oscillations and/ or rocking of the particle can appreciably intensify

mass transfer. In some experiments, dissolution rate displayed an almost twofold decrease after the transition. Thus, the dissolution rate depends not only on medium conditions and velocity of the particle, but also on the regime of motion. In fact, higher dispersion of the particle radius measurements in the range of larger slope (**Figure 43**) is also an indirect indication of the instability of particle path and/ or shape.

7.0 CONCLUSIONS AND FUTURE WORK

7.1 PARTICLE FREE MOTION IN QUIESCENT MEDIUM

Experiments with freely moving solid spheres in quiescent media have shown that these spheres obey the Standard Drag Curve (SDC) only up to certain critical Reynolds number. At this Re, a bifurcation in particle motion was found. The transition to a non-rectilinear (periodic) path causes a jump in particle drag. **Figure 45** demonstrates the drag curves for three different magnitudes of density ratio.

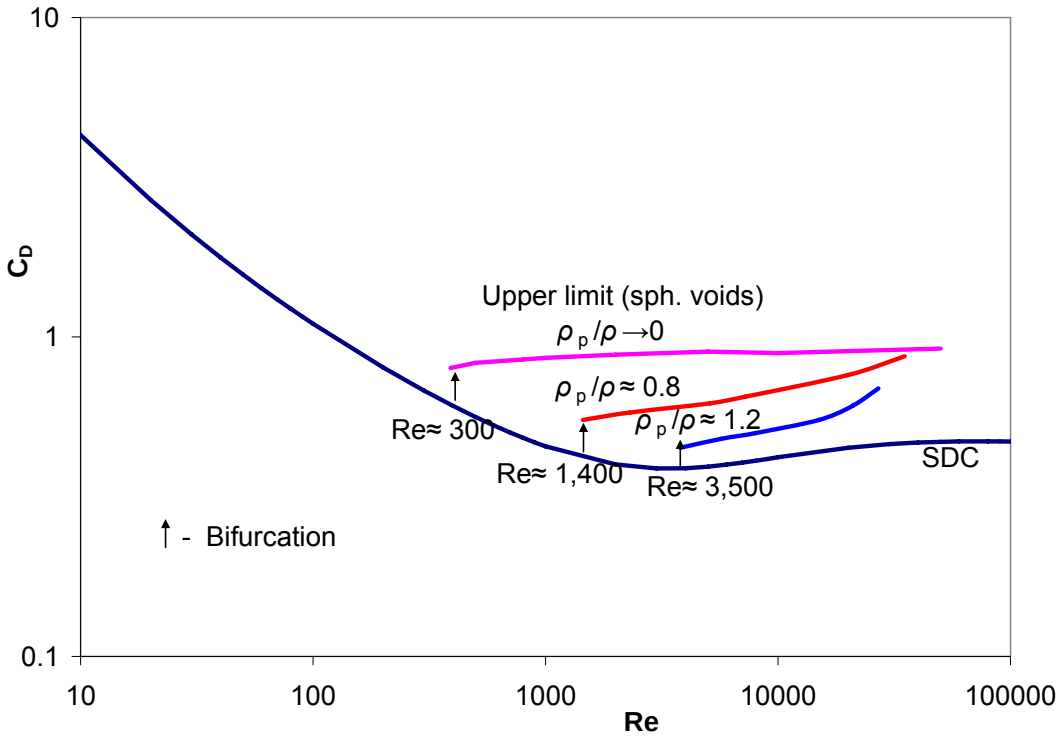

Figure 45. General hypothesis on behavior of freely moving spheres in quiescent medium. Bifurcation from SDC (standard drag curve) occurs at higher magnitudes of Re for heavier spheres.

It is believed that the bifurcation occurs due to the transition to unsteady vortex shedding around the sphere (starts at Re ≈ 300). Hence, even for spherical voids a bifurcation is not expected for Re below 300. In general, though, the bifurcation in the particle regime of motion does not coincide with the onset of vortex shedding. It depends on particle inertia and occurs at higher magnitudes of Re for larger density ratios. Thus, the drag of freely moving solid spherical particles can not be uniquely defined for a given Re, as it was in case of fixed spheres. It is worth emphasizing that spheres with the same magnitude, but different signs of buoyancy, $\frac{\rho_p - \rho}{\rho} = \pm 0.2$, have different drag curves (see **Figure 45**). Comparison of these two curves explicitly shows the importance of inertia, which causes the difference in behavior of rising and sinking particles of the same buoyancy.

Figure 45 represents averaged drag curves for three particle materials. Actual data for these spheres demonstrate very strong scattering. It was shown that this scattering is caused by non-uniform mass distribution in solid spheres. Therefore, it would be useful to perform a set of experiments with carefully chosen highly uniform spheres of various diameters and densities. This experimental data could be a unique reference case for freely moving solid and fluid particles.

Under the assumption of negligible tangential interface mobility (no special precautions were taken to purify the experimental facility), a parametric study of the free motion of fluid particles in water was performed. Based on the results of this study, the following description is suggested for fluid particles behavior in non-purified medium (see **Figure 46** and Appendix G).

A concept of the Morton number, as a measure of particle deformability, is introduced[21] (see Sections 2.3.5 and 5.2.2). The Standard Drag Curve (SDC) for solid spheres can be considered as a curve corresponding to zero deformability, while the Large Morton Limit (LML) curve is treated as maximum deformability permitted by physical laws. The insert in **Figure 46** shows a simplified three-parametric approach to the behavior of fluid particles. Although it does not provide a realistic picture of the drag in the transitional regime, it helps to visualize the concept of deformability. At low Re, corresponding to low energy of the flow, the drag of the fluid particles in contaminated media will follow the SDC. As Re increases, the growing energy of the flow deforms the particles and gradually increases the drag above that predicted by the SDC. Eventually, with further growth of Re, the drag curve approaches the LML (highest deformability limit). Since the motion from SDC towards LML corresponds to the growth of Re, the particle deformation increases as we move along the experimental curves. Significantly, particles of higher deformability (higher *Mo*) deviate from the SDC (from sphericity) and approach the LML at lower magnitudes of Re.

[21] To avoid confusion, one should clearly distinguish between deformability and actual particle deformation. A particle of given deformability (given Mo) can deform differently depending on the Reynolds number (depending on the kinetic energy of the flow). Ability to deform does not necessarily mean the presence of deformation. For example, in Stokes flow (Re→0) even a highly deformable particle (large Mo) maintains an almost spherical shape.

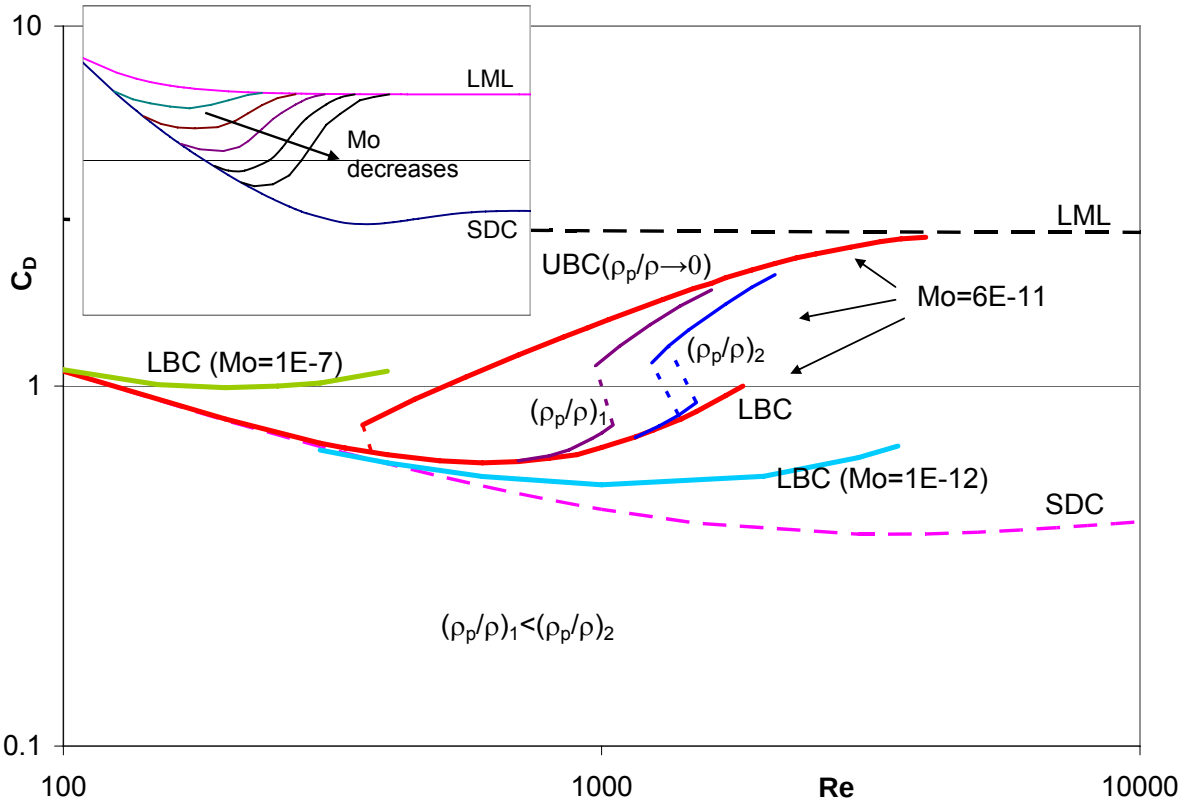

Figure 46. General hypothesis on behavior of freely moving fluid particles in quiescent medium (SDC – standard drag curve; LML – large Morton limit; UBC – upper bound curve; LBC – lower bound curve). For more details, see enlarged figure in Appendix G.

The uniqueness of the drag behavior for fixed *Mo* holds only up to the bifurcation. The unique portion of the drag curve, which is obeyed by every particle with given *Mo* (given deformability), is referred to as the Lower Bound Curve (LBC). Formally, the LBC corresponds to the situation when the energy of the oscillating flow is insufficient to challenge the stability of the rectilinear particle motion. To find the bifurcation point and the behavior after the bifurcation, additional parameters should be taken into account. It is logical to anticipate an analogy with the behavior of solid spheres at this point; namely, the bifurcation from the LBC occurs at higher Re for denser particles (see **Figure 46**). This is, indeed, the case to some extent. In particular, the fluid particles with minimum inertia (air bubbles) demonstrate instability of the

rectilinear regime of motion at the smallest possible Re (≈ 300); while significantly heavier oils ($\rho_p / \rho = 0.92 - 0.96$), although having the same *Mo*, stay on LBC up to Re ≈ 1,300-1,400. After the bifurcation, a jump occurs to another (upper) branch of the drag curve. All the upper branches for particles with fixed *Mo* seem to eventually approach the curve corresponding to air bubbles (minimum inertia), as Re grows.[22] Therefore, we call this curve the Upper Bound Curve (UBC). In turn, the UBC itself approaches the LML, where the periodic behavior is expected to vanish. The stochastic fluctuations along with rectilinear (on average) particle motion are anticipated ("spherical cap like" behavior). It does not necessarily mean that a particle returns to the rectilinear regime, but reflects a widely accepted point of view that after the third bifurcation the behavior of a dynamic system becomes chaotic ("noise-like") [46-48]. Another important limitation should be kept in mind regarding the vicinity of the LML, namely, the structural integrity of a particle. For particles with relatively low interfacial tension, a particle may break up before it reaches the LML or even before the bifurcation to non-rectilinear regime of motion.

Similar trends are expected for other magnitudes of *Mo*: the drag deviates from SDC to LBC for the chosen *Mo*; the bifurcation from LBC occurs, which eventually merges the UBC and LML curves. However, not all the medium/ particle pairs at fixed *Mo* follow the trend "larger particle density – later bifurcation." Since the fluid particles differ from the solid spheres by the ability to change shape, under certain circumstances another issue arises – stability of this shape. For some combinations of the parameters, we were able to observe the particle shape oscillations. Typically, they occurred earlier than the expected transition to the periodic path and destabilized the rectilinear motion of the particle. In the presence of shape oscillations, the bifurcation from rectilinear regime occurred earlier than without them, even for denser particles.

[22] Sometimes (in particular, during the release of large drops by inverting the cup) some overshooting of the upper curve for air bubbles was observed. This trend should be investigated in more details and, if confirmed, reasonable physical arguments for it should be found.

It is conjectured that particle viscosity, which is typically neglected for particles in contaminated media, becomes important in the transitional region. Using the one-dimensional analogy, it was shown that a dynamic system of moving particles can develop shape oscillations, if the product of interfacial tension and particle mass sufficiently exceeds particle viscous damping (see Eq.(54)). This conjecture needs further experimental support and analytical/ numerical development.

7.2 PARTICLE STABILIZATION IN LWT & HWT

The entire problem of particle stabilization within the limits of the viewing window is essentially three-dimensional. Since the velocity profile in the unit is not uniform, any lateral motion from the axis of the pipe transports the particle to regions of higher velocity. This interaction of axial and lateral motions is not taken into account in the one-dimensional model and one-dimensional control and, in conjunction with other passive and active control limitations (sluggish response, noise, pump delay), it is the source of additional instability.

Our findings on bifurcations in the drag curve and effect of particle viscosity on drag enable us to form several conclusions for the applied problem of particle stabilization in the HWT. First, the presence of the bifurcation in drag makes it impossible to use the curve fit of type (D5) (see **Figure 50**) in the region of the jump and of possible conditional stability. Respectively, linearization in this region is impossible. It does not necessarily mean that particle stabilization is impossible with PID control. But particle behavior becomes more erratic when it reaches this zone in the course of dissolution, and change of the stabilization parameters may be required. The study of the CO_2 particle dissolution in HWT also revealed a rather sharp drop in dissolution rates once the particle reaches a critical size. A thorough investigation of numerous experimental

results has shown that the observed jump in dissolution rate approximately corresponds to the Re for bifurcation of the drag curve. This conclusion seems to be supported by the common sense, because particle lateral wandering and/or shape oscillations are expected to enhance the mass transfer.

Secondly, it was shown that particle viscosity becomes an important factor, affecting particle motion for some ranges of parameters. Namely, the ratio of viscous forces inside the particle to the particle inertia and interfacial tension determines the presence or absence of the particle shape oscillations. This helps to explain the differences in behavior of the oil drops in LWT and CO_2 particles in HWT for certain range of Re, even when they both have the same Morton number. Indeed, high oil viscosity suppresses shape oscillation in oil drops, although for CO_2 particles it can be observed in some regimes.

Basically, there are two transitions in the considered experimental systems. First, it is transition from the laminar to turbulent regime in the test section, corresponding to the flow rate of approximately 11 L/min for the chosen system geometry. It causes more intensive flow restructuring and an earlier loss of velocity minimum on the axis downstream from the conditioner. Another transition is related to the change in the regime of particle motion. This transition depends on particle size and buoyancy and is associated with the onset of instability in the rectilinear motion of the particle. If, in the course of dissolution, the particle reaches one of these transitions, it may cause additional problems with stabilization.

As described above, the HWT was successfully used to investigate the fate of CO_2 droplets (including droplets with a hydrate shell) in many realistic simulations of the deep ocean environment. For some experimental regimes and particle sizes, stability of CO_2 liquid particles was not as good as desired (see Section 6.5.2) In several occasions this resulted in not

representative enough data sets due to insufficient particle residence time in the observation window, or just caused particle loss in the course of the experiment. As a result of studies in this thesis, it was shown that particle stability in the HWT can't be significantly improved even by the active means of stabilization, due to the characteristics of the control system and specifics of flow and particle regimes, including bifurcations.

APPENDIX A

DISCUSSION OF DRAG COEFFICIENT FOR SPHERICAL CAP

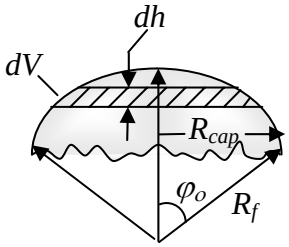

Figure 47. Calculation of the spherical cap volume

In general, the process of obtaining the solution for the so called spherical cap shape does not involve the particularities of the shape at the rear of a fluid particle. Since we are in an inertial regime of motion, the following two postulates are used for the large air bubbles [30]:

a) in the vicinity of the front stagnation point the bubble is spherical (or almost spherical in the work of Joseph [76]);
b) velocity in the vicinity of stagnation point can be approximated by the potential for the sphere, giving the following tangential velocity on the surface:

$$u_{\varphi} = \frac{3}{2} U \sin\varphi \qquad \text{(A1)}$$

Omitting the details, the idea of the Davis & Taylor [30] approach is the following.

The pressure inside the bubble is assumed constant. If the front of the bubble is perfectly spherical, then pressure on its outer side must be constant, too. Two factors contribute to the pressure change on the outer surface of the bubble – dynamic force and gravity. To keep pressure constant, they should balance each other:

$$\frac{u_\varphi^2}{2} = gx = gR_f(1-\cos\varphi), \tag{A2}$$

where x is a vertical coordinate in the direction of gravity with the origin at the stagnation point.

Substituting Eq.(A1) into Eq.(A2), we obtain:

$$U = \frac{2}{3}\sqrt{2gR_f\frac{1-\cos\varphi}{\sin^2\varphi}}, \tag{A3}$$

or for small angle φ (vicinity of the stagnation point):

$$U = \frac{2}{3}\sqrt{gR_f}. \tag{A4}$$

Batchelor [31] suggested some generalization of this solution, assuming the density of the fluid particle is not negligible. Then, pressure inside the particle is not a constant, but depends at least on the altitude. Neglecting the dynamic force inside the particle, one obtains:

$$\rho\frac{u_\varphi^2}{2} - \rho gx = -\rho_p gx \quad \Rightarrow \quad \frac{u_\varphi^2}{2} = \frac{\rho-\rho_p}{\rho}gR(1-\cos\varphi) \tag{A5}$$

Finally, using Eq.(A1) we obtain for small angle φ :

$$U = \frac{2}{3}\sqrt{gR_f\frac{\rho-\rho_p}{\rho}} \tag{A6}$$

Thus, strictly speaking, the so called spherical cap solution does not involve the spherical cap geometry. This geometry (cap angle, $\varphi_0 \in [47^\circ - 58^\circ]$), shown in **Figure 47** and discussed in

Section 1.3, is assumed a priori from the experimental observations rather than being determined as part of a solution. No velocity field around the particle can be obtained using this method.

In engineering aerodynamics, the drag coefficient is usually calculated based on the projected area. However, for purposes of this paper, it is more convenient to introduce an effective diameter (diameter of spherical particle volumetrically equivalent to the spherical cap). Therefore, the drag coefficient for the spherical cap is calculated based on the maximum cross sectional area of an equivalent spherical particle. Thus:

$$C_D^{eq} = C_D \cdot \left(R_{cap} / R_{eq}\right)^2 \tag{A7}$$

To estimate the ratio R_{cap} / R_{eq}, a particular value of angle φ_o must be chosen. As was mentioned in Section 1.3, the angle φ_o of a spherical cap lies within rather narrow range: $\varphi_0 \in [47^o - 58^o]$. The calculations below will be performed for the average value of this angle: $\varphi_0 \approx 52^o$.

First, we calculate the volume of spherical cap. Assuming axial symmetry, the volume of the spherical cap V can be evaluated using an infinitesimal volume, dV:

$$dV = \pi(R_f \sin\varphi)^2\, dh = \pi R_f^2 \sin^2\varphi(-R_f \sin\varphi)d\varphi = -\pi R_f^3 \sin^3\varphi\, d\varphi$$

and therefore:

$$V = -\int_{\varphi_o}^{0} \pi R_f^3 \sin^3\varphi\, d\varphi = -\pi R_f^3 \int_{\varphi_o}^{0} \sin^3\varphi\, d\varphi = \frac{\pi R_f^3}{12}\left(9\cos\varphi - \cos 3\varphi\right)\Big|_{\varphi_o}^{0} = \tag{A8}$$
$$= \frac{\pi R_f^3}{12}\left(8 + \cos 3\varphi_o - 9\cos\varphi_o\right) = \frac{\pi R_f^3}{12}\left(8 + \cos 156^o - 9\cos 52^o\right) \approx 0.129\pi R_f^3$$

Using the definition of the equivalent radius for the spherical cap, R_{eq} and Eq.(A2):

$$R_{eq} = \left(\frac{3V}{4\pi}\right)^{1/3} \approx \left(\frac{3}{4\pi} 0.129\pi R_f^3\right)^{1/3} \approx 0.459 R_f \tag{A9}$$

Thus, we have approximately the following relation between equivalent radius of a spherical cap and its projected radius R_{cap}:

$$R_{cap} = R_f \cdot \sin 52^{\circ} \approx 0.79 R_f \approx 1.72 R_{eq}$$

Hence: $C_D^{eq} = C_D \cdot \left(R_{cap} / R_{eq}\right)^2 \approx 2.96 C_D$ (A10)

Thus, the value of C_D based on the effective radius is about 2.96 times larger, than familiar C_D for projected area of spherical cap.

It follows from a force balance for the spherical cap:

$$\frac{1}{2} C_D \rho U^2 A_{cap} = \frac{1}{2} C_D^{eff} \rho U^2 A_{eq} = \Delta\rho g V , \quad \text{(A11)}$$

where: $V \approx 0.129 \pi R_f^3$;

$$A_{cap} = \pi R_{cap}^2 = \pi R_f^2 \sin^2 52^{\circ} = 0.624 \pi R_f^2 ;$$

$$A_{eq} = \pi R_{eq}^2 = \pi R_f^2 (0.459)^2 = 0.21 \pi R_f^2 \quad \text{(A12)}$$

Substituting these values into the force balance equations, we obtain after simplifications:

$$0.312 C_D \rho U^2 = 0.105 C_D^{eq} \rho U^2 = 0.129 \Delta\rho g R_f \qquad \Rightarrow$$

$$C_D = 0.413 \frac{\Delta\rho}{\rho} \frac{g R_f}{U^2} ; \; C_D^{eq} = 1.23 \frac{\Delta\rho}{\rho} \frac{g R_f}{U^2} \quad \text{(A13)}$$

From Batchelor [31], the expression for the particle velocity in a spherical cap regime:

$$U = \frac{2}{3} \sqrt{g R_f \frac{\Delta\rho}{\rho}} . \quad \text{(A14)}$$

Hence: $\boxed{C_D \approx \frac{9}{4} \times 0.413 \approx 0.93}$; $\boxed{C_D^{eq} \approx \frac{9}{4} \times 1.23 \approx 2.77}$. (A15)

As we noticed earlier, the drag coefficient based on equivalent spherical particle will be about three times larger than the familiar drag based on the projected area of the spherical cap. The

magnitude of the effective drag coefficient is rather close to experimentally obtained value of 8/3, especially if we take into account the very approximate character of the above evaluation. Although Eq.(A4) and Eq.(A6) do not depend on the particular shape at the rear of a fluid particle, expressions (A15) were obtained for the particular cap angle: $\varphi_0 \approx 52^o$.

APPENDIX B

"UNIVERSAL CORRELATION" FOR THE DRAG OF FLUID PARTICLES

The idea of finding a magic formula, which would describe the drag of any fluid particle, sounds very attractive. In fact, several researchers tried to create a pair of non-dimensional numbers in the hope that in their coordinate system all experimental data (or at least a good bit of a range) will fit the same curve.

These attempts can give only a very limited success, unless the whole picture of liquid particles drag is present for the full range of Re and *Mo*. Even having a complete chart with set of curves $C_D = C_D(\mathrm{Re}, Mo)$, it's quite difficult to find a good correlation for fluid particles.

As an example, consider one of the most successful correlations for fluid particles, developed in works of Hu-Kintner, Johnson-Braida, Grace et al [66-68]. The following non-dimensional combinations were suggested for correlation curve:

$$H = \frac{4}{3} Eo\, Mo^{-0.149} \lambda^{-0.14}$$
$$J = \mathrm{Re}\, Mo^{0.149} + 0.857 \qquad \text{(B1)}$$

where

$$Eo = \frac{\Delta\rho\, g\, D_{eq}^2}{\gamma} = \frac{\Delta\rho\, g\, D_{eq}^3}{\gamma\, D_{eq}} = \left[\frac{\text{buoyancy}}{\text{surface tension}}\right] \quad \text{– Eotvos number;}$$

$\lambda = \dfrac{\mu_p}{\mu}$ – viscosity ratio.

The correlation was recommended by Grace et al. [68] for contaminated fluid particles:

$$J = \begin{cases} 0.94H^{0.757}, & for \quad 2 < H < 59.3 \\ 3.42H^{0.441}, & for \quad H > 59.3 \end{cases} \tag{B2}$$

for $Mo < 10^{-3}$; $Eo < 40$; $\mathrm{Re} > 0.1$.

To assess this correlation, we represent it in more familiar and physically relevant form C_D(Re,Mo). To achieve the form, express H and J in terms of C_D, Re, and Mo and substitute the result into Eq.(B2). The final expression for the drag, which is equivalent to Eq.(B2):

$$C_D = \begin{cases} \lambda^{0.21}\left[0.99Mo^{0.013}\,\mathrm{Re}^{-0.01} + 0.85Mo^{0.136}\,\mathrm{Re}^{-1.01}\right]^2, & for \quad 2 < H < 59.3 \\ \lambda^{0.21}\left[0.28Mo^{0.07}\,\mathrm{Re}^{0.412} + 0.24Mo^{-0.079}\,\mathrm{Re}^{-0.588}\right]^{3.4}, & for \quad H > 59.3 \end{cases} \tag{B3}$$

for $Mo < 10^{-3}$; $Eo < 40$; $\mathrm{Re} > 0.1$.

Before giving a graphical representation of Eq.(B3), we comment on drag as a function of viscosity ratio. As it follows from Eq.(B3), drag is proportional to viscosity ratio in a fixed power 0.21. This means that drag grows from 0 to infinity with viscosity ratio. For example, if the drop viscosity increases about 30 times (oil drops versus organic solvent drops), the formula states that drag should increase twice for all Reynolds numbers. This is inconsistent with known results. Drag is rather independent (or very weakly dependent) of the viscosity ratio in contaminated fluids. And if this dependence exists, it is much more complex than a simple power law. Equation (B3) may look reasonable if we consider a narrow range of viscosity ratios (say, 0.2-5). But it does not have much physical ground and does not correspond to the experimental trend in the wide range of viscosity ratios.

Therefore, below we omit viscosity ratio dependence from Eq.(B3), and build a graphical representation of Eq.(B3) assuming $\lambda = 1$.

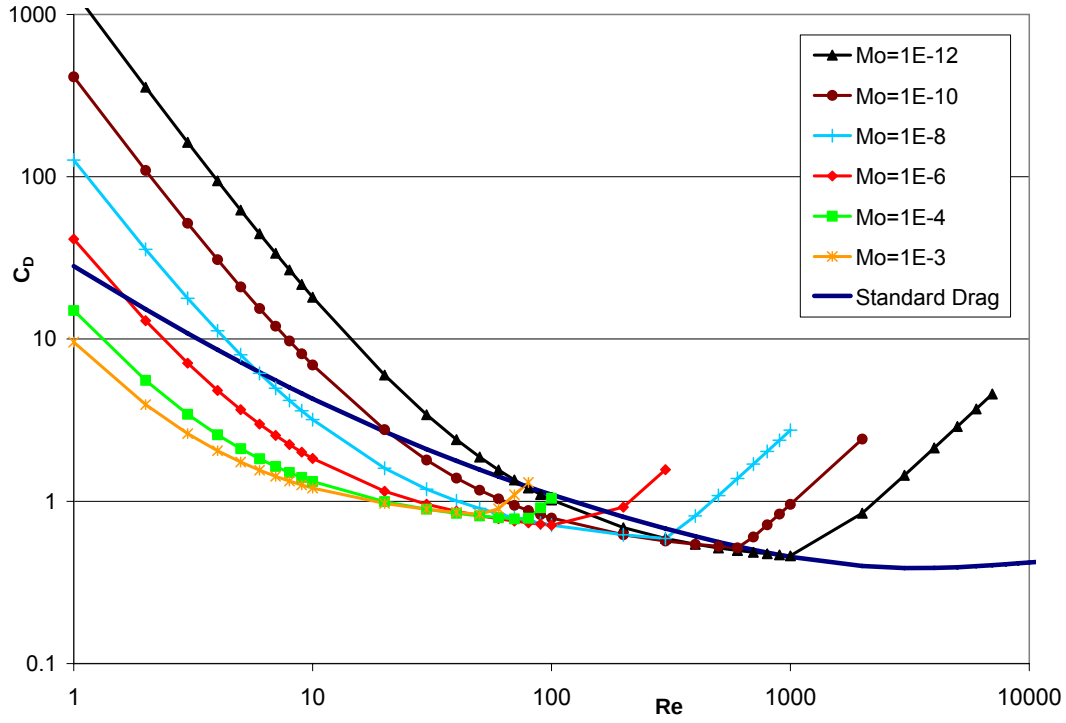

Figure 48. "Universal" drag curves for fluid particles (viscosity ratio $\lambda = \mu_p / \mu = 1$)

Drag curves, described by Eq.(B3) reflect the reality to some degree only in the vicinity of the local drag minimum, where the particle starts to deviate from the standard drag curve. Equation (B3) does not describe properly the most interesting part of drag curve, namely, how the drag grows in the transitional regime and how it approaches the spherical cap regime. Even the drag local minimum obtained from Eq.(B3) seems to work only for small Morton numbers. For moderate *Mo*, it drifts rather far from the standard drag curve. The slope of the curve (B3) for low Re significantly exceeds the slope of the standard drag curve, which also does not seem to be correct.

In the transitional region (higher Re) of **Figure 48**, all curves have the same slope in log/log coordinates. However, as it was shown in Sections 2.3.4, 5.2, and 5.3, the particuliarities of drag behavior in this region depend on the viscosity ratio and/or density ratio and may significantly differ for different liquids and gases even for the fixed Morton number. Moreover, the drag curves in the transitional region undergo a bifurcation at some value of the Reynolds number, which can not be reflected by the empirical model (B3).

APPENDIX C

VELOCITY MEASUREMENTS IN THE LWT & HWT USING THE PITOT TUBE

During the preliminary work with the LWT directed at optimization of the test section design, velocity profiles for water flow were obtained using a standard Pitot tube (Series 166/167, Dwyer stainless steel Pitot tube) in conjunction with the differential pressure transducer (Validyne DP103-06). However, neither the standard Pitot tube, nor commercially available S-type Pitot tube could be used in the HWT due to space limitations. Therefore, a special S-type Pitot tube was designed and fabricated at NETL for this particular application. The usage of the custom made Pitot tube requires some additional efforts for calibration. Namely, the calibration procedure should be performed in two steps:

1. The differential pressure transducer must be calibrated with respect to the standard Pitot tube.
2. The scaling coefficient for the custom made S-type Pitot tube must be found, using the calibrated transducer.

The calibration procedure was performed in the LWT, with the Pitot tube located on the axis of the test section. A simple model flow through the test section without the conditioning element was used. Assuming that the flow (either laminar or turbulent) was close to fully developed, we

were able to obtain an additional integral verification of the calibration procedure, based on the known flow rate.

To calibrate the differential pressure transducer with the standard Pitot tube, a high precision Dwyer No.1420 Hook gage (±0.0005" H_2O) was used. Although having a very slow response (order of an hour), it gave results, which were consistent with the aforementioned integral verification for the given flow rate (4% to 6% unidirectional error). The calibration curve for the differential pressure transducer with the standard Pitot tube is shown in **Figure 49**:

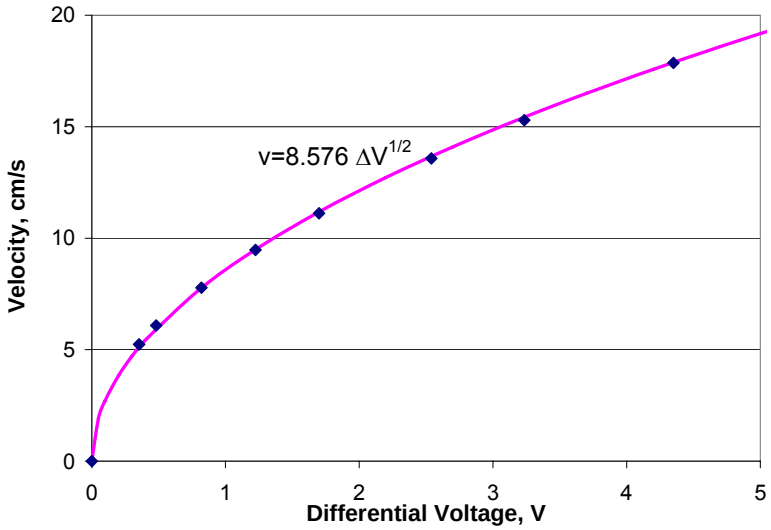

Figure 49. Calibration curve for the differential pressure transducer with the standard Pitot tube

Using the Bernoulli approximation (typical for Pitot tubes) and highly linear response of the pressure transducer, we obtain that the squared velocity is proportional to the pressure difference in the transducer and to the measured differential voltage:

$$v^2 \sim \Delta p \sim \Delta V \qquad \text{(C1)}$$

Hence, the following fit is obtained for the calibration curve:

$$v = 8.576\ \Delta V^{1/2} \qquad \text{(C2)}$$

Similar set of experiments for the S-type Pitot tube was used to find its scaling coefficient. The scaling coefficient has the range 0.75-0.79 and shows slight variation with the change of flow rate. As the flow rate grows from 5 L/min to 25 L/min, the scaling coefficient drops from 0.79 to 0.75. Hence, the calibration curve for the custom made S-Pitot tube would approximately be:

$$v \approx 6.60\, \Delta V^{1/2} \qquad \text{(C3)}$$

Besides size, the custom made S-type tube has several advantages compared with the standard Pitot tube. These include: possibility of bi-directional velocity measurements; faster response; about 25% better sensitivity. The latter is important for low velocities, because even for the most sensitive pressure transducer (used in these experiments), the precision of measurements is never better than 0.01 V.

After calibration, the S-type tube with automatically controlled stepping motor was mounted on the HWT. Velocity measurements were taken at the points along the diameter of the test section with an increment of 2mm. The measurement procedure was automated using LabVIEW version 6 software from National Instruments, of Austin, TX.

Note that the measuring system – Pitot tube + pressure transducer – has a very low temporal sensitivity. After traversing to a new measuring point, it could take up to several minutes for the measuring system to reach a steady state. Therefore, this system can be used only for a steady regime of flow or to provide a temporal average. It can not be used to measure flow fluctuations.

APPENDIX D

NUMERICAL EXAMPLE OF THE VERTICAL STABILITY MODEL

Consider Eq.(63) introduced in Section 6.2.1 with the following values of parameters:

$$\rho_p = 0.97\,\mathrm{g/cm^3};\ \rho = 1\,\mathrm{g/cm^3};$$

$$R = 0.6\,\mathrm{cm};\ \mu = 0.0145\,\mathrm{g/(cm\cdot s)} = 1.45\ \mathrm{mPa\cdot s}; \tag{D1}$$

$$r_o = 3\,\mathrm{cm};\ g = 981\,\mathrm{cm/s^2},$$

that are within the working range of the experimental HWT facility and are actually used for the comparative experiment that will be presented later. Code in MathCad 2001 Professional was written to calculate one-dimensional linearized equation of motion. Some highlights of this procedure are shown below.

First, the inertia term of Eq.(63) is calculated (mass of the particle):

$$m = \frac{4\pi}{3}\rho_p R^3 \approx 0.88\,\mathrm{g}. \tag{D2}$$

Next, the equilibrium velocity, $\bar{\mathrm{v}}$, is determined from the balance of the drag and buoyant forces. The buoyant force is given by:

$$F_b = \frac{4}{3}\pi R^3(\rho - \rho_p)g \approx 26.6\ \mathrm{g\cdot cm/s^2} = 0.266\ \mathrm{mN}. \tag{D3}$$

The drag force is proportional to the drag coefficient C_D:

$$F_d = \frac{\pi}{2} C_D \rho \, \mathrm{v}_r^2 \, R^2 \tag{D4}$$

As shown in the preceding chapters, the behavior of the drag curve, C_D(Re), for fluid particles is quite complex. Even before the onset of bifurcation it gradually deviates from the SDC (see **Figure 26**), demonstrating slightly faster growth due to non-sphericity. In order to perform linearization (56), we need some analytical expression for the drag curve. Equation (7b) can give quite a decent fit for medium Reynolds numbers or for the case of a hydrate shell around the particle (hydrodynamically behaves similar to a solid sphere). As an alternative, the following drag curve fit can be used (see **Figure 50**):

$$C_D = \frac{24}{\mathrm{Re}}\left(1 + 0.173\,\mathrm{Re}^{0.657}\right) + \frac{3}{1 + 3{,}000{,}000\,\mathrm{Re}^{-1.82}} \tag{D5}$$

It corresponds to some average drag curve for fluid particles with $Mo \approx 5 \cdot 10^{-11}$ (see discussion in Section 5.2.2 and **Figure 22**). In fact, for the example considered here, both Eq.(D5) and Eq.(7b) give similar results in terms of settling time. Similarity of the results may be caused by the fact that the Reynolds numbers considered in the numerical examples (and in the experiments, respectively) are < 1,000. Curves given by Eq.(D5) and Eq.(7b) don't differ significantly in this region of Re (see **Figure 50**).

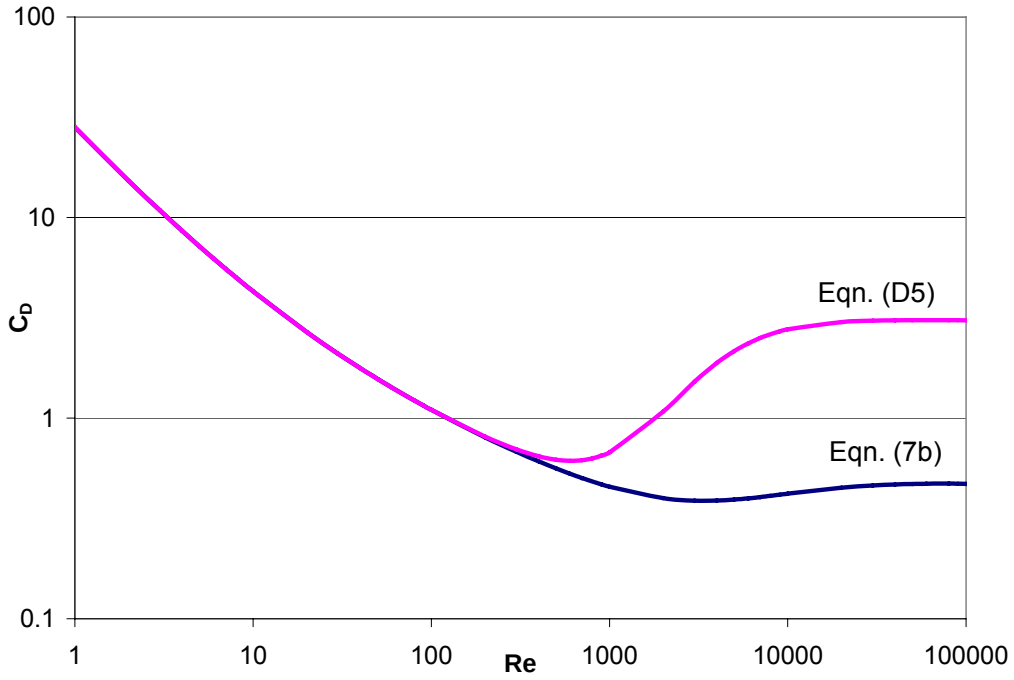

Figure 50. Curve fits corresponding to Eq.(7b) and Eq.(D5)

At equilibrium, the drag force will be equal to the buoyant force:

$$F_d(\bar{v}_r) = F_b\,. \tag{D6}$$

Substituting Eq.(D4) and Eq.(D5) into Eq.(D6), an equilibrium velocity can be found:

$$\mathrm{v}_r = 8.7 \text{ cm/s}\,. \tag{D7}$$

This corresponds to the following Reynolds number:

$$Re = \frac{\rho\,\bar{\mathrm{v}}_r\,R}{\mu} \approx 745\,. \tag{D8}$$

The last step is to linearize the expression for the drag force around the equilibrium velocity:

$$F_d(v_r) \approx -30.8 + 6.59\,v_r = \eta + \gamma\,\mathrm{v}_r\,, \quad \text{for } \left|\mathrm{v}_r - \bar{\mathrm{v}}_r\right| << \mathrm{v}_r\,. \tag{D9}$$

The governing Eq.(63) will take the form:

$$m\ddot{z} = 6.59\left[\Delta_{\mathrm{v}}(t) + \bar{\mathrm{v}}\frac{2\tan\alpha}{r_o}z - \dot{z}\right]. \tag{D10}$$

Substituting m from Eq.(D2) and $\bar{v}$ from Eq.(48) gives:

$$0.88\,\ddot{z} = 6.59\left[\Delta_v(t) - 8.7\frac{2\tan\alpha}{3}z - \dot{z}\right] = 6.59\,\Delta_v(t) - 6.59\dot{z} - 57.3(\tan\alpha)\,z\,. \qquad \text{(D11)}$$

As a result, the coefficients from Eq.(63) will become: $m = 0.88$; $\gamma = 6.59$; $b = 57.3\tan\alpha$. Using Eq.(64) for critical damping, the following is obtained:

$$(6.59)^2 = 4\cdot(57.3\tan\alpha)\cdot 0.88 \qquad \text{or} \qquad \alpha \approx 12^o\,. \qquad \text{(D12)}$$

Note that if the divergence angle α of the test section becomes sufficiently large, Eq.(58) may not be reasonably satisfied even for a parabolic fluid velocity profile. Due to the fast expansion, the profile may significantly deviate from its initial shape. Further, a jet like regime may occur with reverse flow near the pipe walls. In addition, the use of such a large angle is impractical because the length of the test section becomes smaller than the pipe diameter (or becomes comparable with the particle size).

Therefore, for the experimental facility, a diverging angle of $\alpha \approx 1.4^o$ was chosen. It is much smaller than the critical damping angle, that is, the system is significantly overdamped. This high damping will cause the return of the system to equilibrium after a disturbance to be very sluggish, something that can be ameliorated with the addition of feedback control.

Substituting $\alpha \approx 1.4^o$ into Eq.(D12) yields the following linearized equation of motion:

$$\ddot{z} + 7.49\dot{z} + 1.59z = 7.49\,\Delta_v(t)\,, \qquad \text{(D14)}$$

that has the following transfer function:

$$G(s) = \frac{7.49}{s^2 + 7.49s + 1.59} = \frac{7.49}{s^2 + 2\zeta\,\omega_n s + \omega_n^2} = \frac{7.49}{(s+7.27)(s+0.22)}\,. \qquad \text{(D15)}$$

The real poles of this overdamped second-order system are: $s_{1,2} = \{-7.27; -0.22\}$, (D16)

and the damping coefficient is: $\zeta \approx \frac{7.49}{2\cdot 1.26} \approx 2.97$. (D17)

APPENDIX E

VELOCITY PROFILES IN THE TEST SECTION OF THE HWT

Figure 34 shows velocity profiles measured at the set point (z = 0, see **Figure 31**) of the test section in HWT and the conditioner used to create these specific velocity profiles. However, this figure does not completely describe the velocity distribution in the test section. We need information about the velocity profiles development in the test section downstream from the conditioner at least within the limits of the observation windows. To obtain these data, two additional ports for Pitot tube were used at the top and the bottom of the oblong window at z = 5.7 and z = -5.7 (see **Figure 16** and **Figure 31**). **Figure 51** and **Figure 52** below provide experimentally obtained velocity profiles at these cross sections.

These profiles along with profiles in **Figure 34**b are used to obtain velocity development on the axis of the test section and to confirm the existence of the favorable velocity gradient in vertical direction (**Figure 35**).

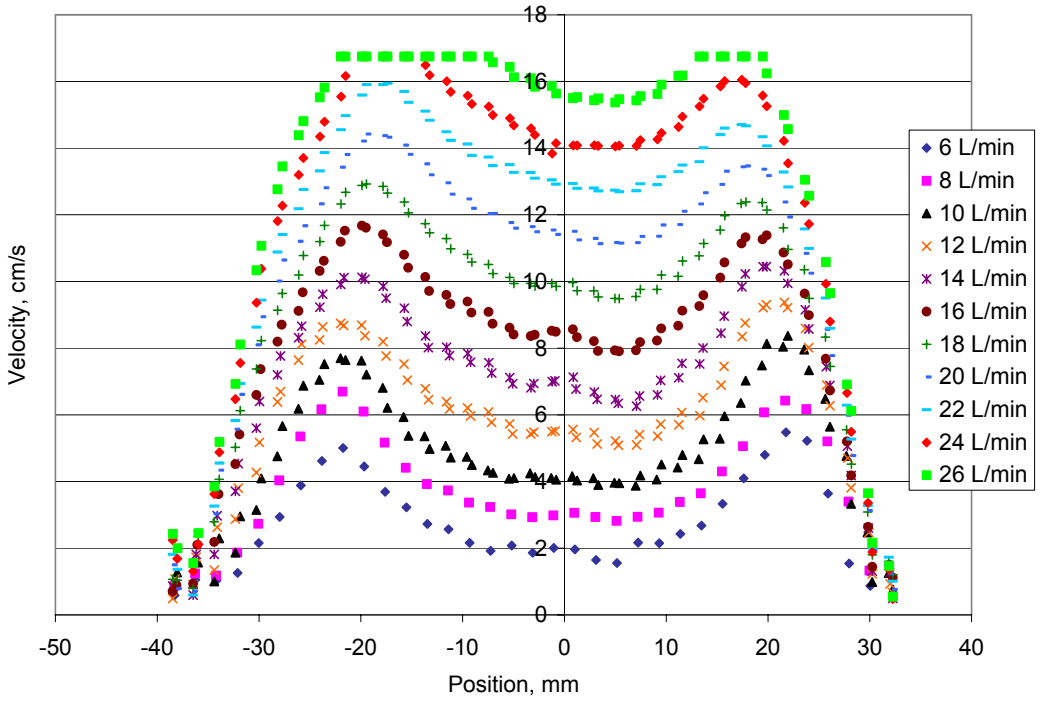

Figure 51. Velocity profiles measured at z=5.7cm for different flow rates

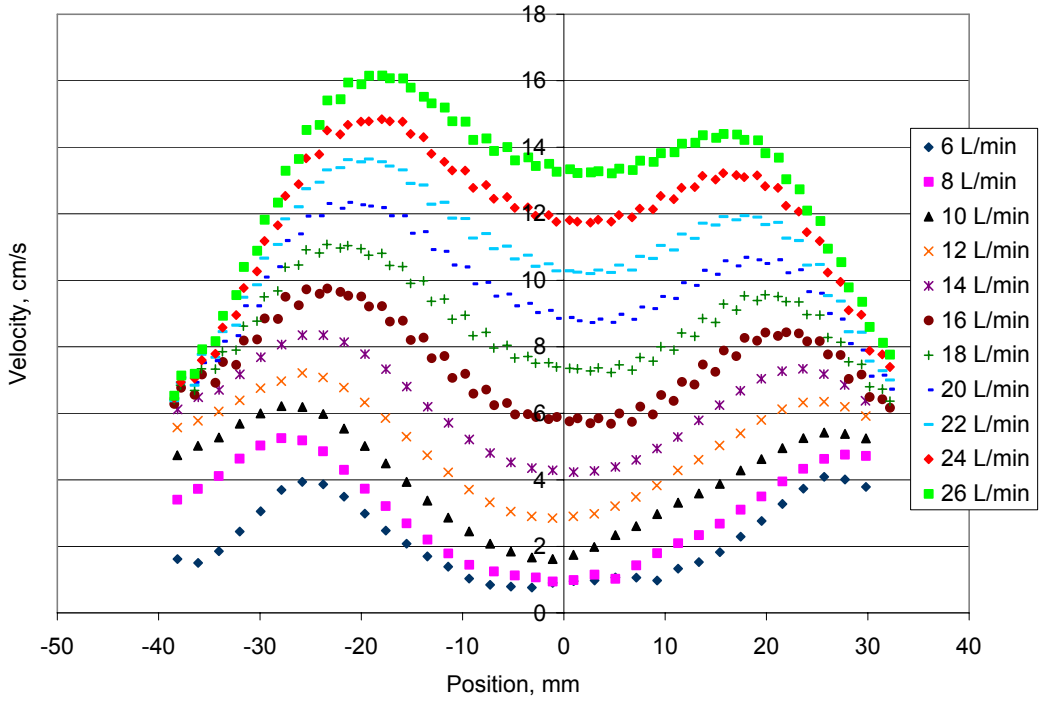

Figure 52. Velocity profiles measured at z=-5.7cm for different flow rates

APPENDIX F

DISSOLUTION RATE OF A CO_2 PARTICLE

Material loss for spherical CO_2 particle is due to the flow through the particle surface. Hence, particle volume change is proportional to its surface area:

$$\frac{dV}{dt} = -\Gamma \cdot A, \qquad \text{(F1)}$$

where $V = \frac{4}{3}\pi R^3$ - volume of spherical particle [cm^3];

$A = 4\pi R^2$ - surface area of the spherical particle [cm^2];

Γ - dissolution rate $\left[\frac{cm^3}{cm^2 \cdot s}\right]$

Dissolution rate can be considered as a volume escaping from particle through unit area per second, and depends on mechanical & thermodynamical conditions in the vicinity of the particle.

Substitute expressions for the volume and surface area of the spherical particle into Eq.(F1):

$$V = \frac{4}{3}\pi R^3; \quad A = 4\pi R^2 \quad \Rightarrow \quad \frac{4}{3}\pi \frac{dR^3}{dt} = -\Gamma \cdot 4\pi R^2 \quad \Rightarrow \quad \boxed{\frac{dR}{dt} = -\Gamma} \qquad \text{(F2)}$$

The last expression, basically, means that dissolution rate is a temporal change of particle radius.

Mention again, that these calculations were based on assumption of particle sphericity. Typically, CO_2 particles, observed in HWT, have eccentricity of about 1.2. Thus, they will have

slightly larger surface area than spherical particle of equivalent volume. It means, that the assumption of particle sphericity slightly underestimates dissolution rate.

Calculate an error, introduced by non-sphericity of the particle. In the worst case scenario in our experiments, particle eccentricity was:

$$\frac{a}{c} = 1.5\,. \tag{F3}$$

Then ellipticity: $$e \equiv \left(1 - c^2 / a^2\right)^{0.5} \approx 0.745 \tag{F4}$$

Using a simplified assumption that non-spherical particle has a shape of oblate spheroid, we obtain the surface areas for oblate spheroid and sphere, respectively:

$$S_O = 2\pi a^2 + \pi \frac{c^2}{e} \ln\left(\frac{1+e}{1-e}\right); \qquad S_S = 4\pi r^2 \tag{F5}$$

If volumes of these particles are equal, then:

$$a^2 c = r^3 \tag{F6}$$

Using the last equality and definition of ellipticity, we obtain ratio of surface areas:

$$\frac{S_O}{S_S} = \frac{1}{4\left(1-e^2\right)^{1/3}} \left[2 + \frac{1-e^2}{e} \ln\left(\frac{1+e}{1-e}\right)\right] \tag{F7}$$

or, substituting 0.745 for ellipticity:

$$\frac{S_O}{S_S} \approx 1.031\,, \tag{F8}$$

that is, the error in dissolution rate due to particle non-sphericity is at most 3%.

APPENDIX G

GENERAL HYPOTHESIS ON FREELY MOVING FLUID PARTICLES IN QUIESCENT MEDIUM

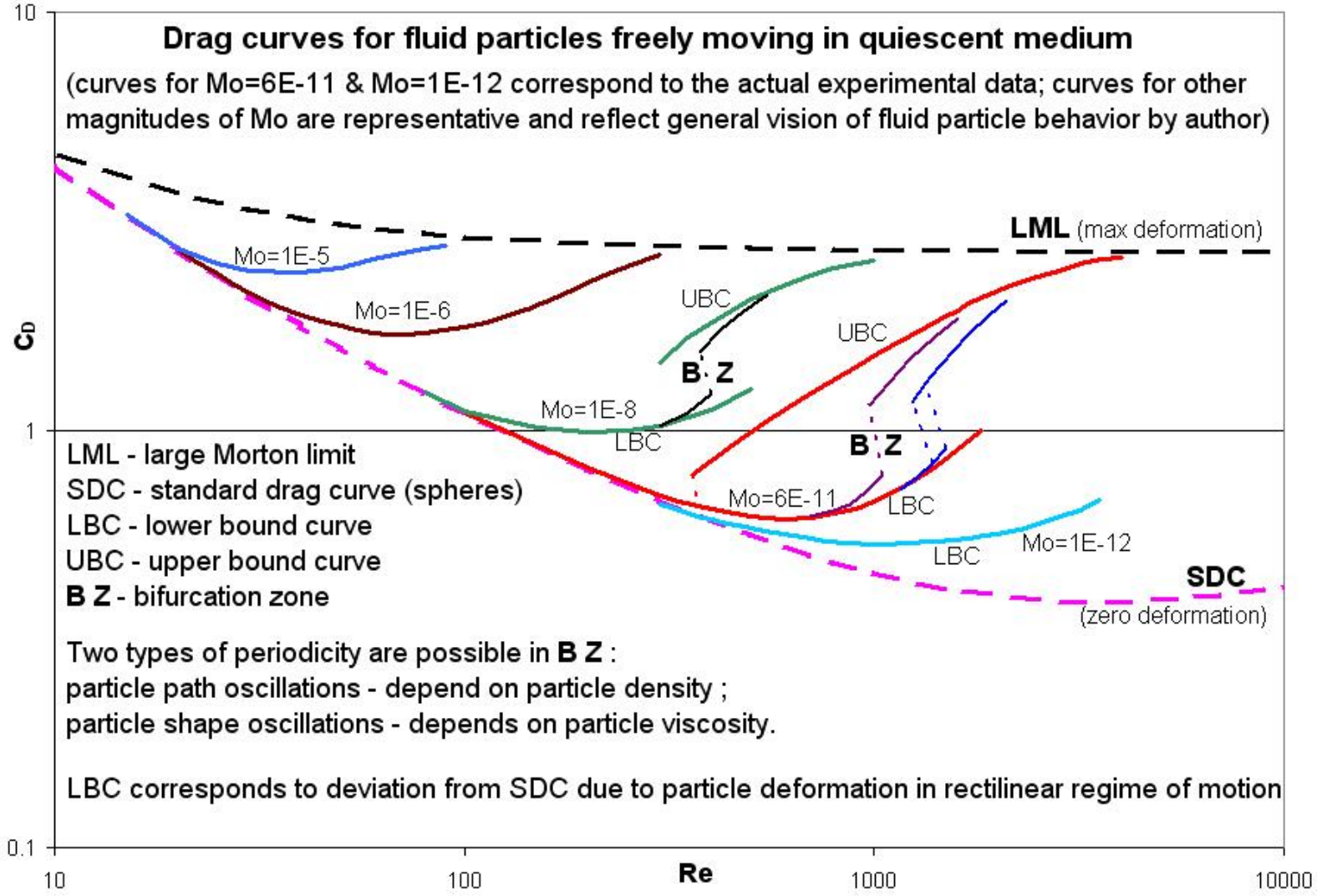
Drag curves for fluid particles freely moving in quiescent medium
(curves for Mo=6E-11 & Mo=1E-12 correspond to the actual experimental data; curves for other magnitudes of Mo are representative and reflect general vision of fluid particle behavior by author)
LML (max deformation)
Mo=1E-5
Mo=1E-6
UBC
UBC
B Z
Mo=1E-8
LBC
B Z
Mo=6E-11
LBC
LBC
Mo=1E-12
SDC
(zero deformation)
LML - large Morton limit
SDC - standard drag curve (spheres)
LBC - lower bound curve
UBC - upper bound curve
B Z - bifurcation zone
Two types of periodicity are possible in B Z :
particle path oscillations - depend on particle density ;
particle shape oscillations - depends on particle viscosity.
LBC corresponds to deviation from SDC due to particle deformation in rectilinear regime of motion
10
1
0.1
C_D
10
100
1000
10000
Re

BIBLIOGRAPHY

1. Clift, R., Grace J.R., Weber M.E., *Bubbles, drops, and particles*. 1978, New York: Acad. Press.

2. *Carbon sequestration research and development*. 1999, U.S. Department of Energy Report, DOE/SC/FE-1, available from NTIS.

3. Herzog, H., *Greenhouse gas control technologies*, ed. B. Eliasson, P.W.F. Riemer, A. Wokaun. 1999, Amsterdam: Pergamon. 237-242.

4. Angus, S., Armstrong B., de Reuck K.M., *Carbon Dioxide International Thermodynamic Tables*. Commission on Thermodynamics and Thermochemistry, Imperial College, London: Pergamon Press.

5. Warzinski, R.P., G.D. Holder, *Greenhouse gas control technologies*, ed. B. Eliasson, P.W.F. Riemer, A. Wokaun. 1999, Amsterdam: Pergamon. 1061-1063.

6. Bridgman, P.W., *Dimensional analysis*. 1931, New Haven, CT: Yale University Press.

7. White, F.M., *Fluid Mechanics*. Fourth ed. 1999: WCB/McGraw-Hill.

8. Wieselsberger, C., *Weitere Feststellungen uber die Gesetze des Flussigkeits- und Luftwiderstandes.* Phys. Zeitschr., 1922. **23**: p. 219-224.

9. Liebster, H., *Uber den Widerstand von Kugeln.* Ann. Phys., 1927. **82**: p. 541-562.

10. Lapple, C.E., Shepherd C.B., *Calculation of particles trajectories.* Ind. Eng. Chem., 1940. **32**(5): p. 605-617.

11. Turton, R., Levenspiel O., *A short note on the drag correlation for spheres.* Powder Technol., 1986. **47**: p. 83-86.

12. Flachbart, O., *Neue Untersuchungen uber den Luftwiderstand von Kugeln.* Phys. Z., 1927. **28**: p. 461-469.

13. Newton, I., *Mathematical ptinciples of natural philosophy*. 1969, New York: Greenwood Press.

14. Lapple, C.E., *Fluid and Particle Mechanics*. 1951, Newark: University of Delaware.

15. Stokes, G.G., Trans. Camb. Philos. Soc., 1851. **9**(8).

16. Allen, H.S., *The motion of a sphere in a viscous fluid.* Philos. Mag., 1900. **50**: p. 323-338, 519-534.

17. Bailey, A.B., *Sphere drag coefficient for subsonic speeds in continuum and free-molecular flows.* J. Fluid Mech., 1974. **65**: p. 401-410.

18. Achenbach, E., *The effects of surface roughness and tunnel blockage on the flow past spheres.* J. Fluid Mech., 1974. **65**: p. 113-125.

19. Hadamard, J.S., *Mouvement permanent lent d'une sphère liquide et visqueuse dans un liquide visqueux.* Comptes Rendus des Scéances de l'Académie des Sciences, 1911. **152**: p. 1735-1738.

20. Rybczynski, W., *On the translatory motion of a fluid sphere in a viscous medium.* Bulletin International de l'Académie Polonaise des Sciences et des Lettres, Classe des Sciences Mathématiques et Naturelles, A, 1911: p. 40-46.

21. Bond, W.N., Newton D.A., *Bubbles, Drops, and Stokes' Law.* Philos. Mag., Ser.7, 1928. **5**: p. 794-800.

22. Frumkin, A., Levich V.G., Zh. Fiz. Khim. [Russ. J. Phys. Chem.], 1947. **21**: p. 1183-1204.

23. Masliyah, J.M., Epstein N., J. Fluid Mech., 1970. **44**: p. 493-512.

24. Haberman, W.L., Morton R.K., *An experimental investigation of the drag and shape of air bubbles rising in various fluids*. 1953, Navy Dept., The David W. Taylor Model Basin.

25. Levich, V.G., *Physicochemical Hydrodynamics*. 1962: Prentice Hall.

26. Savic, P. 1953, National Research Council of Canada.

27. LeVan, M.D., Newman J., *The effect of surfactant on the terminal and interfacial velocities of a bubble or drop.* AIChE J., 1976. **22**(4): p. 695-701.

28. Sadhal, S.S., Johnson R.E., *Stokes flow past bubbles and drops partially coated with thin films. Part 1. Stagnant cap of surfactant film - exact solution.* J. Fluid Mech., 1983. **126**: p. 237-250.

29. Harper, J.F., Moore D.W., *The motion of a spherical liquid drop at high Reynolds number.* J. Fluid Mech., 1967. **32**(2): p. 367-391.

30. Davies, R.M., Taylor G.I., *The mechanics of large bubbles rising through extended liquids and through liquids in tubes.* Proc. R. Soc. London, Ser. A, 1950. **200**: p. 375-390.

31. Batchelor, G.K., *An introduction to fluid dynamics*. 1967: Cambridge University Press.

32. Davenport, W.G., Richardson F.D., Bradshaw A.V., *Spherical cap bubbles in low density liquids.* Chem. Eng. Sci., 1967. **22**: p. 1221-1235.

33. Wu, B.J.C., Deluca R.T., Wegener P.P., Chem. Eng. Sci., 1974. **29**: p. 1307-1309.

34. Lindt, J.T., *Time dependent mass transfer from single bubbles*, in *Scheikundig Ingenieur Geboren te Amsterdam*. 1971. p. 130.

35. Ellingsen, K., Risso F., *On the rise of an ellipsoidal bubble in water: oscillatory paths and liquid-induced velocity.* J. Fluid Mech., 2001. **440**: p. 235-268.

36. Bhaga, D., Weber M.E., *Bubbles in viscous fluids: shapes, wakes, and velocities.* J. Fluid Mech., 1981. **105**: p. 65-81.

37. Wairegi, T., *The mechanics of large drops and bubbles moving through extended liquid media*, in *Chemical Engineering*. 1974, McGill University: Montreal. p. 299.

38. Maxworthy, T., Gnann C., Kürten M., Durst F., *Experiments on the rise of air bubbles in clean viscous liquids.* J. Fluid Mech., 1996. **321**: p. 421-441.

39. Ormières, D., M. Provansal, *Transition to turbulence in the wake of a sphere.* Phys. Rev. Lett., 1999. **83**(1): p. 80-83.

40. Natarajan, R., Acrivos A., *The instability of steady flow past spheres and disks.* J. Fluid Mech., 1993. **254**: p. 323-344.

41. Johnson, T.A., Patel V.C., *Flow past a sphere up to a Reynolds number of 300.* J. Fluid Mech., 1999. **378**: p. 19-70.

42. Ghidersa, B., Dušek J.,, *Breaking of axisymmetry and onset of unsteadiness in the wake of a sphere.* J. Fluid Mech., 2000. **423**: p. 33-69.

43. Gushchin, V.A., Kostomarov A.V., Matyushin P.V., Pavlyukova E.R., *Direct numerical simulation of the transitional separated fluid flows around a sphere and a circular cylinder.* J. Wind Eng. Ind. Aerod., 2002. **90**: p. 341-358.

44. Landau, L.D., *On the problem of turbulence (in Russian).* DAN SSSR, 1944. **44**: p. 339-342.

45. Swinney, H.L., J.P. Gollub, *The transition to turbulence.* Phys. Today, 1978. **31**(8): p. 41.

46. Ruelle, D., F.Takens, *On the nature of turbulence.* Commun. Math. Phys., 1971. **20**: p. 167.

47. Crutchfield, J.P., J.D.Farmer, B.A.Huberman, *Fluctuations and simple chaotic dynamics.* Phys. Rep., 1982. **92**: p. 45.

48. Schuster, H.G., *Deterministic Chaos*. 1984, Weinheim: Physik-Verlag.

49. Goldburg, A., Florsheim B.H., *Transition and Strouhal number for the incompressible wake of various bodies.* Phys. Fluids, 1966. **9**: p. 45-50.

50. Sheth, R.B., *Secondary motion of freely moving spheres*. 1970, Brigham Young University: Provo, Utah.

51. Viets, H., Lee D.A., *Motion of freely falling spheres at moderate Reynolds numbers.* AIAA J., 1971. **9**: p. 2038-2042.

52. Preukschat, A.W., *Measurements of drag coefficients for falling and rising spheres in free motion*. 1962, Calif. Inst. Technol.: Pasadena.

53. MacCready, P.B., Jex H.R., *Study of sphere motion and balloon wind sensors*, in *NASA Tech. Memo.* 1964.

54. Karamanev, D.G., Nikolov L.N., *Free rising spheres do not obey Newton's law for free settling.* AIChE J., 1992. **38**(11): p. 1843-1846.

55. Karamanev, D.G., *The study of free rise of buoyant spheres in gas reveals the universal behavior of free rising rigid spheres in fluid in general.* Int. J. Multiphase Flow, 2001. **27**: p. 1479-1486.

56. Galdi, G.P., *On the motion of a rigid body in a viscous fluid: a mathematical analysis and applications*, in *Handbook of mathematical fluid dynamics*. 2002: North-Holland, Amsterdam. p. 653-791.

57. Jenny, M., G. Bouchet, J. Dusek, *Nonvertical ascension or fall of a sphere in a Newtonian fluid.* Phys. Fluids, 2003. **15**(1): p. L9-L12.

58. Oberbeck, H.A., Crelles J., 1876. **81**: p. 62-87.

59. Payne, L.E., Pell W.H., J. Fluid Mech., 1960. **7**: p. 529-549.

60. Pell, W.N., Payne L.E., *On Stokes flow about a torus.* Mathematika, 1960. **7**: p. 78-92.

61. Pell, W.N., Payne L.E., Q. Appl. Math., 1960-1961. **18**: p. 257-262.

62. Dorrepaal, J.M., O'Neill M.E., Ranger K.B., J. Fluid Mech., 1976. **75**: p. 273-286.

63. Rosenberg, B., *The drag and shape of air bubbles moving in liquids*. 1950, The David W. Taylor Model Basin.

64. Moody, L.F., Trans. ASME, 1944. **66**.

65. Feng, Z.G., Michaelides E.E., *Drag coefficients of viscous spheres at intermediate and high Reynolds numbers.* J. Fluid Eng. - Trans. ASME, 2001. **123**(4): p. 841-849.

66. Hu, S., Kintner R.C., *The fall of single liquid drops through water.* AIChE J., 1955. **1**: p. 42-48.

67. Johnson, A.I., Braida L., *The velocity of fall of circulating and oscillating liquid drops through quiescent liquid phases.* Can. J. Chem. Eng., 1957. **35**: p. 165-172.

68. Grace, J.R., Wairegi T., Nguyen T.H., Trans. Inst. Chem. Eng., 1976. **54**: p. 167-173.

69. Krishna, P.M., Venkateswarlu D., Narasimhamurty G.S.R., *Fall of liquid drops in water.* J. Chem. Eng. Data, 1959. **4**(4): p. 336-343.

70. Edge, R.M., Grant C.D., *The motion of drops in water contaminated with a surface-active agent.* Chem. Eng. Sci., 1972. **27**: p. 1709-1721.

71. Ozaki, M., Minaniura J., Kitajima Y., Mizokami S., Takeuchi K., Hatakenaka K., *CO_2 ocean sequestration by moving ships.* J. Mar. Sci. Technol., 2001. **6**: p. 51-58.

72. Thorsen, G., Stordalen R.M., Terjesen S.D., *On the terminal velocity of circulating and oscillating liquid drops.* Chem. Eng. Sci., 1968. **23**: p. 413-426.

73. Garner, F.H., D.A. Lihou, DECHEMA - Monogr., 1965. **55**: p. 155-178.

74. Beard, K.V., J. Atmos. Sci., 1976. **33**: p. 851-864.

75. de Vries, A.W.G., *Path and wake of a rising bubble*. 2001, Universiteit Twente. p. 105.

76. Joseph, D.D., *Rise velocity of a spherical cap bubble.* J. Fluid Mech., 2003. **488**: p. 213-223.

77. Moore, D.W., *The rise of a gas bubble in a viscous fluid.* J. Fluid Mech., 1959. **6**: p. 113-130.

78. Beavers, G.S., Joseph D.D., *The rotating rod viscometer.* J. Fluid Mech., 1975. **69**(3): p. 477-512.

79. Joseph, D.D., M.S. Arney, G. Gillberg, H. Hu, D.A. Hultman, C. Verdier, H. Vinagre, *A spinning drop tensioextensiometer.* J. Rheol., 1992. **63**(4).

80. Holder, G.D., L.P. Mokka, R.P. Warzinski, *Formation of gas hydrates from single-phase aqueous solutions.* Chem. Eng. Sci., 2001. **56**: p. 6897-6903.

81. Warzinski, R.P., Lynn R.J., Robertson A.M., Haljasmaa I.V., *High-pressure water tunnel facility for ocean CO_2 storage experimentation.* ACS DIvision of Fuel Chemistry, 2002. **47**(1): p. 25-26.

82. Haljasmaa, I.V., J.S. Vipperman, R.J. Lynn, R.P. Warzinski, *Control of a fluid particle under simulated deep-ocean conditions in a high-pressure water tunnel.* Rev. Sci. Instrum., 2005. **76**(2): p. 1-11.

83. Lide, D.R., ed. *Handbook of chemistry and physics*. 72 ed. 1991-1992.

84. Lindt, J.T., *On the periodic nature of the drag on a rising bubble.* Chem. Eng. Sci., 1972. **27**: p. 1775-1781.

85. Renardy, Y.Y., V. Cristini, *Effect of inertia on drop breakup under shear.* Phys. Fluids, 2001. **13**(1): p. 7-13.

86. Maini, B.B., P.R. Bishnoi, *Experimental investigation of hydrate formation behaviour of a natural gas bubble in a simulated deep sea environment.* Chem. Eng. Sci., 1981. **36**: p. 183.

87. Moo-Young, M., Fulford G., Cheyne I., Ind. Eng. Chem. Fundam., 1971. **10**: p. 157.

88. Franklin, G.F., J.D. Powel, E.-N. Abbas, *Feedback control of dynamic systems*. 2002, Englewood Cliffs, NJ: Prentice-Hall.

89. Brogan, W.L., *Modern control theory*. 1990, Englewood Cliffs, NJ: Prentice-Hall.

90. Dutton, K., S. Thompson, B. Barraclough, *The art of control engineering*. 1997, Reading, MA: Addison-Wesley.